

---

# Unidirectional Coupling of Light from Nanowire Lasers into Silicon Waveguides

---

## Master Thesis

**Urban Senica**

Chair of Nanoelectronics

Department of Electrical and Computer Engineering

and

Chair for Semiconductor Nanostructures and Quantum Systems (E24)

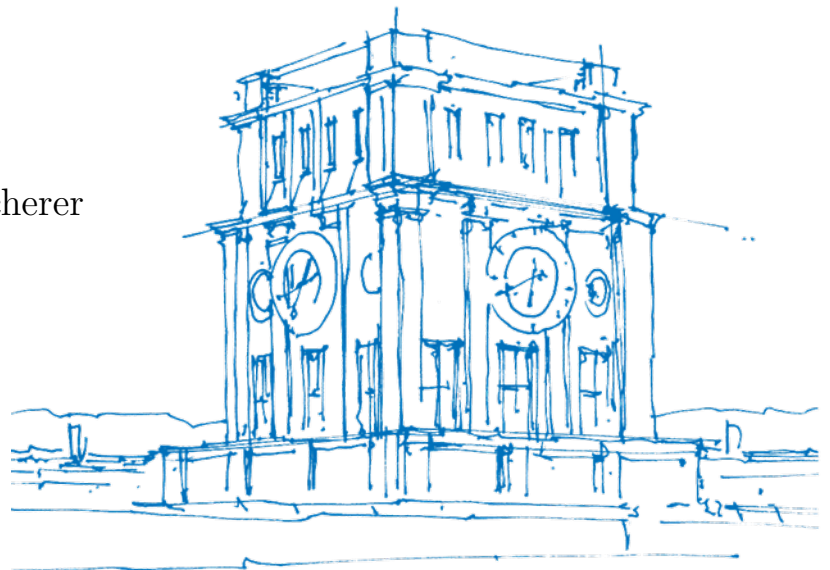
Walter Schottky Institut

**Supervised by**

Prof. Dr.-Ing. habil. Markus Becherer

Chair of Nanoelectronics

München, September 2017



*TUM Uhrenturm*



I hereby declare that this thesis is entirely the result of my own work except where otherwise indicated. I have only used the resources given in the list of references.

München, 26. 9. 2017

Urban Senica



# Acknowledgements

I would like to express my gratitude to all the people that were helpful during the making of this thesis at the Walter Schottky Institut, Technische Universität München.

I thank Prof. Janez Krč for all the helpful discussions and advice from Ljubljana and for fully supporting my decision to do the thesis abroad. Even from a distance, your help and encouragement were very beneficial.

I thank Prof. Markus Becherer for enabling me to do the thesis under the Chair of Nanoelectronics, Department of Electrical and Computer Engineering, TUM. I am grateful to Prof. Jonathan J. Finley for enabling me to do most of the work for my thesis within the E24 Chair at the Walter Schottky Institut and for providing useful ideas and references.

I thank Jochen Bissinger for introducing me to Nanowire Lasers and Simulations and for being a great supervisor in general. Not only were you successfully guiding and advising me throughout the whole thesis process, your positive attitude even in times of doubt and many ideas how to push things forward were crucial in making progress.

I also thank Dr. Gregor Koblmüller for fruitful discussions at the group meetings and for providing great feedback and interesting ideas.

I thank all the other members of the Nanowire Group for the nice atmosphere during my stay at WSI: Doctoral Candidates Jonathan, Daniel, Tom, Sergej, Andreas and Master Students Anton, Wenching, Lin, Lukas, Paul and Tobias.

Last but not least, this thesis would not have been possible without the unconditional support of my family. Hvala za vse!



# Contents

<b>1</b>	<b>Introduction: From Electronics to Photonics</b>	<b>3</b>
<b>2</b>	<b>Semiconductor Nanowire Laser Fundamentals</b>	<b>9</b>
2.1	Photonic Transitions in Direct Band Gap Semiconductors . . . . .	9
2.2	Lasing Condition . . . . .	10
2.3	Lasing Threshold . . . . .	12
2.4	Nanowire Lasers . . . . .	13
2.4.1	Fundamentals . . . . .	13
2.4.2	GaAs-AlGaAs Core-Shell Nanowire Lasers . . . . .	15
<b>3</b>	<b>Waveguide Modes</b>	<b>17</b>
3.1	Basic Concepts . . . . .	17
3.2	Step-index Fiber . . . . .	19
3.3	Nanowire as a Waveguide . . . . .	24
<b>4</b>	<b>Chiral Optics</b>	<b>29</b>
4.1	Chirality Basics . . . . .	29
4.2	Light Angular Momenta . . . . .	30
4.3	Transverse Spin . . . . .	31
4.4	Spin-direction Locking . . . . .	33
4.5	Unidirectional Coupling in Waveguides . . . . .	34
<b>5</b>	<b>Numerical Methods</b>	<b>39</b>
5.1	Finite Element Method . . . . .	39

5.1.1	Procedure . . . . .	40
5.1.2	Mode Analysis with COMSOL . . . . .	43
5.2	Finite Differences Methods . . . . .	45
5.2.1	Finite Difference Eigenmode . . . . .	45
5.2.2	Finite-Difference Time-Domain . . . . .	48
5.2.2.1	Basic Algorithm . . . . .	48
5.2.2.2	FDTD with Lumerical . . . . .	50
<b>6</b>	<b>Simulation Results</b>	<b>53</b>
6.1	GaAs-AlGaAs Core-Shell NW Laser . . . . .	53
6.1.1	Structure . . . . .	53
6.1.2	Mode Analysis . . . . .	55
6.1.3	End Facet Reflectivity . . . . .	57
6.2	Nanowire on a Si Ridge Waveguide . . . . .	63
6.2.1	Structure . . . . .	63
6.2.2	Nanowire Position Offset . . . . .	69
6.2.3	Nanowire Radius . . . . .	76
6.2.4	Waveguide Dimensions . . . . .	78
6.2.5	Mode Amplitudes Ratio . . . . .	83
6.2.6	SiO <sub>2</sub> Layer . . . . .	88
6.3	Summary . . . . .	91
<b>7</b>	<b>Conclusion</b>	<b>95</b>
	<b>Bibliography</b>	<b>99</b>
<b>A</b>	<b>Lumerical MODE Analysis Code</b>	<b>107</b>
A.1	Waveguide . . . . .	107
A.2	Nanowire . . . . .	109
A.3	Spin Dot Product . . . . .	111
<b>B</b>	<b>Lumerical FDTD Postprocessing Code</b>	<b>119</b>

# List of Images

1.1	Optical interconnects . . . . .	5
2.1	Fundamental light-matter interactions . . . . .	10
2.2	Fabry-Pérot resonator . . . . .	11
2.3	$L - I$ curves . . . . .	13
2.4	Basic NW structure . . . . .	14
2.5	GaAs-AlGaAs core-shell nanowire laser . . . . .	15
2.6	Band gaps of semiconductor materials . . . . .	16
3.1	Formation of modes through the interference of light waves . . . . .	18
3.2	Step-index fiber schematic . . . . .	20
3.3	Mode nomenclature, illustrated on a simple example . . . . .	25
3.4	Intensity profiles of the $ Ez $ . . . . .	26
3.5	Electric field intensity $ \mathbf{E} $ profiles . . . . .	27
4.1	Directional emission . . . . .	30
4.2	Light angular momenta . . . . .	31
4.3	Total internal reflection at a dielectric interface . . . . .	33
4.4	Evanescent waves and transverse spin . . . . .	34
4.5	Unidirectional coupling examples from publications . . . . .	36
4.6	Waveguide field component ratios . . . . .	37
4.7	Unidirectional coupling via a dipole source . . . . .	38
5.1	Shapes of finite elements . . . . .	40

5.2	Interpolation with a linear combination approximation . . . . .	41
5.3	COMSOL auto-generated mesh . . . . .	44
5.4	COMSOL eigenmode solution example . . . . .	45
5.5	Yee mesh . . . . .	46
5.6	Yu-Mittra methods and Conformal Mesh Technology . . . . .	50
6.1	The basic GaAs-AlGaAs core-shell NW simulation structure . . . . .	54
6.2	The $n_{\text{eff}}$ dependency on NW radius for several modes . . . . .	56
6.3	Reflectivity vs. NW radius for several supported modes . . . . .	59
6.4	NW with gold mirror . . . . .	59
6.5	Reflectivity vs. gold mirror thickness . . . . .	60
6.6	Field intensity profiles for different gold layer thicknesses . . . . .	61
6.7	NW with an oxide/gold layer stack . . . . .	61
6.8	Reflectivity vs. SiO <sub>2</sub> layer thickness . . . . .	62
6.9	Schematic of the simulated NW on WG structure . . . . .	65
6.10	Electric field intensities $ \mathbf{E} ^2$ , HE11 <sub>a</sub> +HE11 <sub>b</sub> . . . . .	66
6.11	Electric field $z$ component intensities $ E_z $ , HE11 <sub>a</sub> +HE11 <sub>b</sub> . . . . .	66
6.12	Spin angular momentum across the NW cross section . . . . .	67
6.13	Electric field components, fundamental WG mode . . . . .	68
6.14	Map of $\text{Im}(E_x)/\text{Re}(E_y)$ of the fundamental WG mode . . . . .	68
6.15	NW offset sweep . . . . .	71
6.16	Field intensity snapshots at two NW offsets . . . . .	72
6.17	The $S_z$ component of the NW and WG fundamental modes . . . . .	74
6.18	A map of the waveguide's $S_z$ spin component in the $xy$ plane . . . . .	75
6.19	FDTD vs. semi-analytical approximation . . . . .	76
6.20	NW radius and offset sweep . . . . .	78
6.21	WG height and NW offset sweep . . . . .	80
6.22	WG width and NW offset sweep . . . . .	82
6.23	Elliptically polarized waves . . . . .	84
6.24	Amplitudes ratio and NW offset sweep . . . . .	86
6.25	SiO <sub>2</sub> and NW offset sweep . . . . .	89

6.26 Light propagation along the oxide/air interface . . . . . 90



# List of Tables

1	Quantities and Symbols . . . . .	xvii
6.1	Simulation constants . . . . .	54
6.2	Additional simulation constants . . . . .	64



# List of Symbols

Quantity / Label		Unit	
Name	Symbol	Name	Symbol
Energy	$E$	joule	J
Planck constant	$h$	-	J·s
Reduced Planck constant	$\hbar$	-	J·s
Speed of light	$c$	-	m/s
Speed	$v$	-	m/s
Frequency	$f$	Hertz	Hz
Angular frequency	$\omega$	-	rad/s
Time	$t$	second	s
Wavelength	$\lambda$	meter	m
Imaginary unit	$i$	-	-
Refractive index	$n + ik$	-	-
Effective refractive index	$n_{\text{eff}}$	-	-
Group refractive index	$n_g$	-	-
Spontaneous emission factor	$\beta$	-	-
Gain coefficient	$g$	-	$\text{m}^{-1}$
Loss coefficient	$\alpha$	-	$\text{m}^{-1}$
Optical intensity	$I$	-	$\text{W}/\text{m}^2$
Reflectivity	$R$	-	%
Confinement factor	$\Gamma$	-	-
Vacuum permittivity	$\varepsilon_0$	-	F/m

Quantity / Label		Unit	
Name	Symbol	Name	Symbol
Relative permittivity	$\varepsilon_r$	-	-
Vacuum permeability	$\mu_0$	-	H/m
Relative permeability	$\mu_r$	-	
Electric displacement	$\mathbf{D}$	-	As/m <sup>2</sup>
Electric field	$\mathbf{E}$	-	V/m
Magnetic field	$\mathbf{B}$	tesla	T
Magnetic field strength	$\mathbf{H}$	-	A/m
Current density	$\mathbf{J}$	-	A/m <sup>2</sup>
Charge density	$\rho$	-	As/m <sup>3</sup>
Phase velocity	$v_p$	-	m/s
Group velocity	$v_g$	-	m/s
Phase constant	$\beta$	-	rad/m
Wavenumber	$k$	-	m <sup>-1</sup>
Vacuum wavenumber	$k_0$	-	m <sup>-1</sup>
Wavevector	$\mathbf{k}$	-	m <sup>-1</sup>
Bessel function	$J$	-	-
Modified Bessel function	$K$	-	-
Polarization helicity	$\sigma$	-	-
Spin angular momentum	$\mathbf{S}$	-	kg·m <sup>2</sup> ·s <sup>-1</sup>
Intrinsic orbital angular momentum	$\mathbf{L}^{\text{int}}$	-	kg·m <sup>2</sup> ·s <sup>-1</sup>
Extrinsic orbital angular momentum	$\mathbf{L}^{\text{ext}}$	-	kg·m <sup>2</sup> ·s <sup>-1</sup>
Momentum vector	$\mathbf{P}$	-	N·s
Position vector	$\mathbf{R}$	meter	m
Normal vector	$\mathbf{n}$	-	-
Thickness	$d$	meter	m
Length	$l$	meter	m
Power	$P$	Watt	W
Absorption coefficient	$\alpha$	-	m <sup>-1</sup>

---

Quantity / Label		Unit	
Name	Symbol	Name	Symbol
Dipole moment	$\mathbf{d}$	-	As·m
Phase	$\varphi$	radian	rad
Imaginary part	$Im()$	-	-
Real part	$Re()$	-	-

---

**Table 1:** Quantities and Symbols



# List of Abbreviations

- CMOS - complementary metal-oxide-semiconductor
- CMT - Conformal Mesh Technology
- DBR - distributed Bragg reflector
- EM - electromagnetic
- EOAM - extrinsic orbital angular momentum
- FDE - Finite Difference Eigenmode
- FDTD - Finite-Difference Time-Domain
- FEM - Finite Element Method
- IOAM - intrinsic orbital momentum
- MBE - molecular beam epitaxy
- MCM - multi-coefficient material
- MOCVD - metal-organic chemical vapour phase deposition
- MQWs - multiple quantum wells
- NW - nanowire
- NW<sub>off</sub> - nanowire offset

- $NW_{\text{rad}}$  - nanowire radius
- $Ox_{\text{height}}$  - top oxide height
- PEC - perfect electric conductor
- PDE - partial differential equation
- QD - quantum dot
- SAM - spin angular momentum
- Si - silicon
- SOI - Silicon-On-Insulator
- TE - transverse electric
- TEM - transverse electromagnetic
- TM - transverse magnetic
- HE/EH - helical mode
- VCSEL - vertical cavity surface emitting laser
- WG - waveguide
- $WG_{\text{height}}$  - waveguide height
- $WG_{\text{width}}$  - waveguide width

# Abstract

The monolithic integration of efficient, reliable and cheap nanoscale sources on silicon in the desired wavelength range remains the holy grail for chip-level optical interconnects. In this context, (III-V) semiconductor nanowires (NWs) are a promising candidate. Furthermore, the possibility of directional emission into future photonic circuits and networks could prove crucial. This thesis focuses on numerical simulations of different nanowire and waveguide structures to achieve unidirectional coupling of light into a proximal waveguide (WG) via the spin-orbit interaction.

The initial results for a GaAs-AlGaAs core-shell NW show that the NW acts as a low-loss WG, supporting several modes whose field profile and effective refractive index  $n_{\text{eff}}$  depend on the NW radius. The addition of a metal mirror can increase the end facet reflectivity (an important parameter in achieving low-threshold lasing) from 40% to 90% in the case of the fundamental HE11 mode.

To achieve a unidirectional coupling, the NW needs to support a circularly (elliptically) polarized wave. This is achieved by mixing two degenerate HE11<sub>a</sub> and HE11<sub>b</sub> modes, phase shifted by  $\pi/2$ . By placing the NW off-center on top of a Si WG we break the symmetry and the amount of light coupled in opposite directions of the WG differs thanks to spin-orbit coupling. The unidirectional coupling ratio can reach values of nearly  $10^4$  but is extremely sensitive to the NW offset position on the WG - a 10 nm shift can change the coupling ratio by an order of magnitude. The coupling efficiency into the WG depends on the spin overlap between the NW and WG mode and can exceed 10%. The reflectivity back into the NW depends mainly on the NW radius and reaches values of 30%.

The coupling depends also on the NW and WG dimensions, as these affect the  $n_{\text{eff}}$  and field profiles of each of the modes, respectively. A coupling ratio of almost 8000, a coupling efficiency of over 10% and a reflectivity of around 20% are reached with a NW with a 120 nm radius positioned 115 nm off-center on top of a waveguide with a width of 280 nm and a height of 50 nm. To prevent reflection and coupling into higher order modes, the NW and WG dimensions should be kept small enough to exhibit single-mode waveguiding. With a change in the amplitude ratio of the  $a$  and  $b$  mode, one can shift the NW offset with the coupling ratio peak without affecting the coupling efficiency and reflectivity significantly. The introduction of an intermediate  $\text{SiO}_2$  oxide layer (required in the fabrication process for a site-selective growth of NWs) deteriorates the coupling ratio and coupling efficiency. This is due to the propagation of a part of the light along the oxide/air interface where it decays quickly. The reflectivity can be enhanced by tuning the oxide thickness to achieve constructive interference of the back reflected waves without affecting the WG mode.

In summary, the simulation results presented in this thesis show for the first time that unidirectional coupling can in principle be achieved with a NW supporting a circularly polarized propagating wave placed asymmetrically on top of a Si waveguide.

**Key words:** nanowire laser, waveguide, reflectivity, unidirectional coupling, spin-orbit coupling

# Chapter 1

## Introduction: From Electronics to Photonics

Ever since the invention of the transistor in 1947 up to state-of-the-art CMOS technologies, we have been witnessing an incredible evolution of electronics, which became an indispensable part of our daily lives. As early as in 1965, Gordon Moore made his famous observation that the number of transistors on an integrated circuit doubles approximately every two years [1]. The so-called *Moore's law* accurately predicted the exponential progress in semiconductor technology for several decades, mostly thanks to simple but effective shrinking of devices. Unfortunately, the downscaling cannot go on forever - as we race towards sub-10 nm technology nodes, we face undesired quantum-mechanical effects and fundamental physical limitations, with device layers only a few atoms thick. A major issue is the so-called interconnect bottleneck, as the miniaturization of copper wires serving as interconnects causes increased parasitic capacitance, resulting in longer propagation delays which put an upper limit to switching times [2]. A higher integration density and tighter component packing also means a significant increase in heat dissipation and makes efficient cooling a severe challenge. In fact, in today's world of increasing large-scale data communication and information exchange, around 50% of the total power in data centers is dissipated in

copper interconnects [3].

A possible solution to overcome these fundamental limitations is to make a shift from electronic to photonic components and optical interconnects. On the large scale, global information exchange has already been based on optical communications for years, as optical fibers offer several advantages over conventional copper cables - providing much higher communication bandwidths at a lower power loss, which enables longer transmission distances. Vertical cavity surface emitting lasers (VCSELs) have found use in short-reach, high-speed optical interconnects in data centers and server clusters [4]. On the smaller scale, however, implementing optical interconnects efficiently has proven difficult. Even though photonic components are much faster compared to their electronic counterparts, significantly lower integration densities due to the diffraction limit of light prevented a true paradigm shift until this day.

Photonics has been one of the hottest research topics and in the past decade several milestones, pushing the boundary of science and technology, have been reached. Low-loss waveguides [5, 6], directional couplers [7, 8], high-performance optical modulators [9, 10], photodetectors [11, 12], multiplexers [13] and demultiplexers [14] have already been successfully developed and are available on the Silicon-On-Insulator (SOI) platform. These innovations, as well as established CMOS-like low-cost silicon integrated circuit processes put silicon photonics forward as a key enabling technology for next-generation optical communications. Although many of the desired photonic components are already available on the SOI platform, demonstrating the monolithic integration of efficient, reliable and cheap nanoscale light sources on silicon in the desired wavelength range remains the holy grail for chip-level optical interconnects.

Silicon (Si) itself is a terrible light emitter due to its indirect bandgap, which means that interband transitions have to involve a phonon process to satisfy the conservation of energy and momentum. As a consequence, the quantum efficiency is extremely low. There have been several approaches proposed to circumvent this problem, such as using porous Si [16], Si nanocrystals [17], Si Raman lasers [18],

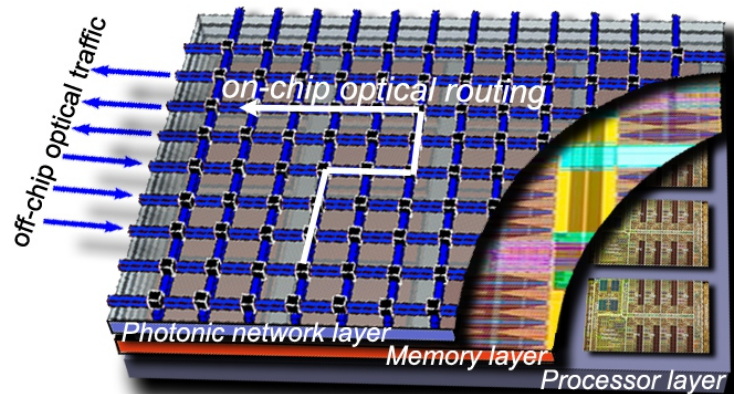


**Figure 1.1:** The realization of integrated light sources on silicon would open the door to optical interconnects for intra- and inter-chip communication, improving the speed and power consumption by orders of magnitude compared to conventional copper wires. Source: [15]

Erbium light sources [19], Ge-on-Si lasers [20, 21], GeSn lasers [22], and III-V-based lasers [23].

Ideally, a light source on silicon should fulfill a few requirements [24]:

- (i) emission in the telecom range ( $1.3\text{-}1.55\ \mu\text{m}$ ),
- (ii) electrical pumping and a high integration density,
- (iii) high power-efficiency,
- (iv) CMOS-compatibility,
- (v) efficient coupling to photonic circuit.

As III-V materials have excellent optical properties, such as a direct band gap, high gain values and the possibility to tune the band gap by varying the composition, a promising strategy would be to integrate III-V active media on silicon. In this context, III-V semiconductor nanowires (NWs) are of great interest as integrated light sources on silicon [25]. Their one-dimensional structure, which forms a natural Fabry-Pérot resonator, and high index contrast enable low-loss waveguiding. Another advantage is that they can be grown site-selectively on silicon using conventional epitaxial processes.

Lasing up to room temperature of optically pumped GaAs-AlGaAs core-shell NWs on a dielectric substrate has been demonstrated in 2013 [26]. Further development resulted in a monolithic integration of NW lasers on silicon with low threshold and high spontaneous emission coupling factors [27]. Current research activities within our group include tuning of the emission wavelength by employing different gain media, such as radially positioned InGaAs multiple quantum wells (MQWs) [28] and the integration of NW lasers on Si waveguides [29].

## The Scope of this Thesis

The scope of this thesis is to evaluate several GaAs-AlGaAs nanowire and silicon waveguide structures through numerical simulations and to explore the possibilities of unidirectional coupling and optimize different parameters to obtain the desired behavior.

The thesis is structured in the following way:

- Chapter 2 reviews the fundamentals of semiconductor lasers and outlines the specifics for nanowire lasers.
- In Chapter 3, the basic properties of waveguide modes are illustrated on an example of a simple optical fiber to then explain the properties of nanowires as waveguides.
- Chapter 4 provides an introduction to the emerging topic of chiral optics and presents phenomena like spin-direction locking, which can be utilized for unidirectional coupling in waveguides.
- Chapter 5 is an overview of the numerical methods utilized by the simulation programs used in the results.
- In Chapter 6, the simulation setup and results are presented in terms of the simulated structures, varied parameters and properties of interest.
- Chapter 7 provides concluding remarks.



# Chapter 2

## Semiconductor Nanowire Laser Fundamentals

As mentioned in Chapter 1, there is a variety of possible strategies towards the realization of integrated light sources on silicon. Semiconductor nanowire lasers are of particular interest due to several advantages.

This chapter commences with a short review of the fundamentals of semiconductor lasers and builds on these basic concepts to enlighten the reader about the specifics of nanowire lasers.

### 2.1 Photonic Transitions in Direct Band Gap Semiconductors

The first laser was successfully demonstrated in 1960 by Theodore H. Maiman, based on theoretical work by Charles H. Townes and Arthur L. Schawlow [30] and has since then proven extremely useful in a variety of fields, ranging from optical communication to medical applications [31]. The acronym LASER stands for *light amplification by stimulated emission of radiation*.

In order to gain some basic understanding, we first review the fundamental light-matter interactions in a semiconductor: *absorption, spontaneous emission*

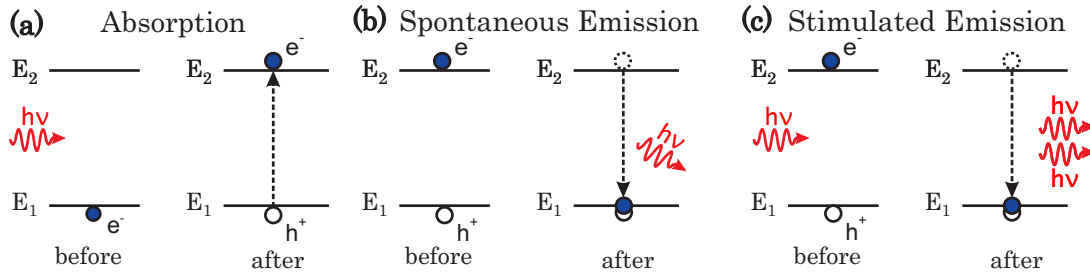


**Figure 2.1:** Illustration of the three fundamental light-matter interactions in a semiconductor. **(a)** An incident photon with sufficient energy gets absorbed and generates an electron-hole pair. An electron in the higher energy state  $E_2$  can recombine either by **(b)** spontaneous emission (after a random time  $\tau_{\text{spon}}$ ) or by **(c)** stimulated emission, triggered by an incident photon. The emitted photon's phase, polarization and direction are random in case of spontaneous emission and match the incident photon in case of stimulated emission.

and *stimulated emission* of light. Considering a direct band gap semiconductor, in a simple model we can approximate the band structure as a system of two discrete states,  $E_2 > E_1$ , see Fig. 2.1. An incident photon with an energy  $E = h\nu$  equal or greater than the energy difference  $E_2 - E_1$  can get absorbed and generates an electron-hole pair. In other words, the electron gets excited and makes a transition to the higher energy state.

In this configuration, there are two possible radiative recombination processes. *Spontaneous emission* occurs when the electron recombines with the hole after a characteristic spontaneous emission lifetime  $\tau_{\text{spon}}$  and emits a photon with a random phase, polarization and direction. In the case of *stimulated emission*, the recombination is triggered through the interaction with another incident photon. The emitted and the incident photon have the same phase, polarization and direction - they are *coherent*.

## 2.2 Lasing Condition

A laser consists of an active medium with population inversion, which can be achieved e.g. by optically pumping the semiconductor active region above its band gap. Furthermore, an optical resonator is required to amplify light - increase

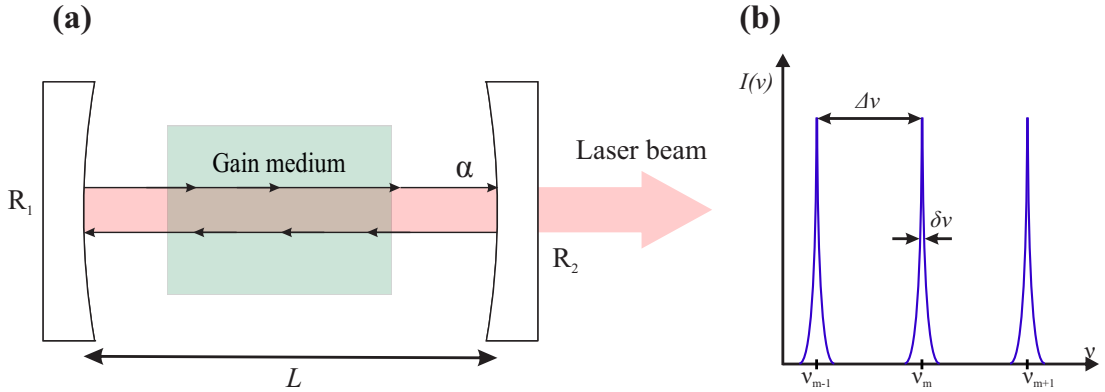


**Figure 2.2:** (a) Illustration of a Fabry-Pérot resonator. Two mirrors separated by distance  $L$  form the optical cavity. Light is amplified in the gain medium region, while the losses occur due to non-ideal mirror reflectivities and absorption in the cavity. Sketch adapted from [35]. (b) The Fabry-Pérot resonator supports longitudinal modes which are spaced equidistantly.

the photon density inside the device to ensure that stimulated emission is the dominating recombination process in order to generate a coherent light output.

One of the simplest optical resonators - the Fabry-Pérot resonator - can be formed by placing mirrors parallel to the active medium [32], see Fig. 2.2(a). Some of the photons, spontaneously generated in the cavity, are then reflected at mirrors and fed back into the gain material, potentially leading to stimulated emission. Once the spontaneous and stimulated emission rates exceed absorption and mirror losses, light amplification is achieved. Due to constructive and destructive interference effects, the resonator supports only certain longitudinal modes which are equidistantly spaced. The supported modes can be described by the following formula [33]

$$q \frac{\lambda_m}{2} = L_{\text{cav}} \quad (2.1)$$

where  $q$  is an integer,  $\lambda_m = \frac{\lambda_{\text{vac}}}{n_{\text{group}}}$  is the wavelength of the mode  $m$  and  $L_{\text{cav}}$  is the length of the cavity. The spectrum of the supported modes is illustrated in Fig. 2.2(b). Light amplification within the gain medium can be expressed with the gain coefficient  $g$  [34]:

$$\frac{dI}{dz} = g(\omega)I(z), \quad (2.2)$$

where  $I$  is the optical intensity,  $\omega$  the angular frequency and  $z$  the direction of propagation of the beam.

## 2.3 Lasing Threshold

In conventional lasers, the lasing threshold is usually defined as the state where gain equals losses. For microscopic lasers it is more correctly defined as the point where the pump power to bring the mean cavity photon number to unity is reached [36]. The required lasing threshold is often determined based on photon density ( $L - I$ ) curves, displaying the relation between output photon density and injection current/pump power. When the spontaneous emission factor  $\beta$  which describes the fraction of spontaneous emission is small, the  $L - I$  curves have a distinguishable sharp twist, typically marked as the laser threshold (see Fig. 2.3). However, in nanolasers,  $\beta$  can reach higher values, the curved features get smoother and we need to resort to one of several other definitions for the threshold: the first- or second-order derivatives of the  $L - I$  curves, the derivative of the  $\log(L) - \log(I)$  curves, the peak height vs width ratio  $s/w$ , and others [37]. It is worth noting that coherence of laser light is more important than its intensity.

If we go back to a simple uniform gain medium between two mirrors, separated by distance  $L$  and with reflectivities  $R_1$  and  $R_2$ , we can derive the threshold conditions. As the mode makes a round-trip through the cavity, it is amplified with a gain coefficient  $g$ , attenuated by the loss coefficient  $\alpha$  and experiences mirror losses due to their finite mirror reflectivities  $R_1$  and  $R_2$ . The gain must therefore compensate the waveguiding and mirror losses [38]:

$$R_1 R_2 e^{-2\alpha L} e^{2g\Gamma L} \geq 1, \quad (2.3)$$

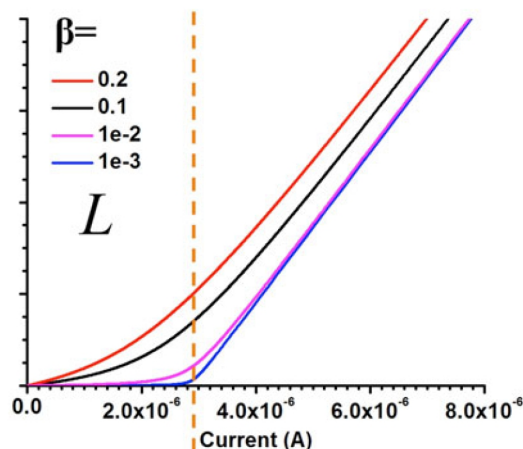


**Figure 2.3:**  $L - I$  curves for different values of spontaneous emission factor  $\beta$ . For small  $\beta$ , there is a distinguishable kink in the curve, often marked as the laser threshold (dashed line). For higher  $\beta$ , the curves get smoother and one of the other definitions for laser threshold needs to be used. Plot taken from [37].

where  $\Gamma$  is the mode confinement factor,  $L$  the resonator length,  $L_g$  the gain medium length and  $\alpha$  the absorption coefficient (in our case,  $L = L_g$ ). The minimum value of  $g$  that satisfies this condition is the threshold gain  $g_{\text{th}}$ :

$$g_{\text{th}} = \frac{1}{\Gamma} \left[ \alpha - \frac{1}{2L} \ln(R_1 R_2) \right] \quad (2.4)$$

Lowering the threshold gain to reduce the required power is a crucial goal in laser design.

## 2.4 Nanowire Lasers

### 2.4.1 Fundamentals

Semiconductor nanowire lasers fulfill many of the requirements to achieve low-threshold lasing. The nanowire represents a gain medium and an optical resonator at the same time [25] - as the end facets behave as mirrors, a longitudinal Fabry-Pérot cavity is formed naturally, see Fig. 2.4. Their unique one-dimensional geometry enables low-loss guiding of supported optical modes.

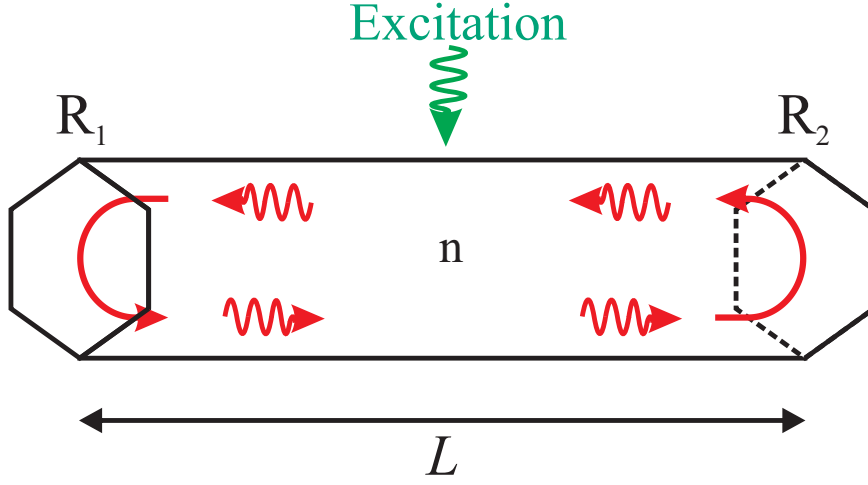


**Figure 2.4:** Illustration of a basic NW structure with end facets serving as mirrors and forming a Fabry-Pérot resonator. Schematic adapted from [25].

High mirror reflectivities are crucial to enable low-threshold operation. To achieve high reflectivities, there should be a significant difference between the photon momentum ( $\hbar k = \hbar \frac{2\pi}{\lambda n_{\text{group}}}$ ) of light propagating inside the nanowire to the one in the surrounding medium. The refractive group index  $n_{\text{group}} = \frac{c}{v_{\text{group}}} = n - \lambda \frac{dn}{d\lambda}$  [39], should therefore have large values compared to the environment (e.g., air,  $n_{\text{group}} = 1$ ).

Another important parameter for efficient waveguiding is enabling high mode confinement factors through a large refractive index contrast between the nanowire and the surrounding medium. The confinement factor is a measure of the mode confinement inside the active gain medium. In conventional laser structures, a simple power confinement factor is usually calculated, i.e., the ratio of the integrals of the Poynting vector over the active region and over the complete mode profile. However, for nanolaser structures exhibiting strong confinement, a definition which accounts for quantum mechanical effects is more correct [40]:

$$\Gamma = \frac{\varepsilon_0 c n_a \iint_{\text{active}} |\mathbf{E}|^2 dx dy}{\iint \text{Re}[\mathbf{E} \times \mathbf{H}^*] \cdot \hat{z} dx dy} \quad (2.5)$$

$c$  is the speed of light,  $\varepsilon_0$  the vacuum permittivity,  $n_a(\omega)$  the refractive index of the

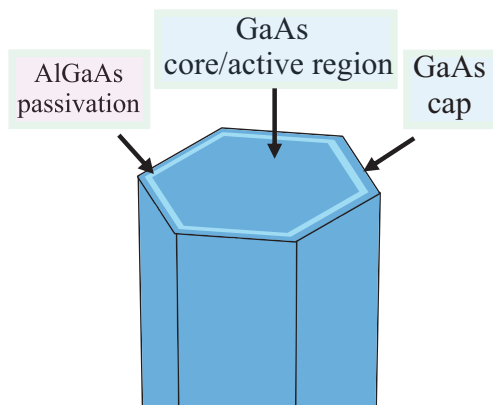


**Figure 2.5:** Schematic of a GaAs-AlGaAs core-shell nanowire laser. The cross-section consists of a GaAs core (active region), followed by a 5 nm thick AlGaAs passivation layer and protected by a 5 nm thick GaAs cap.

active region material at frequency  $\omega$ , while  $\mathbf{E}$  and  $\mathbf{H}$  are the complex electric and magnetic fields of the mode. When defined in this fashion, the confinement factor can reach values above unity. This may seem counterintuitive, as the confinement factor is the ratio between the modal and material gain. The reasoning behind is that light has a higher effective group index and propagates slower within the high index contrast waveguide. This causes the modal gain to increase, even beyond the value of the material gain, further decreasing the necessary threshold gain.

## 2.4.2 GaAs-AlGaAs Core-Shell Nanowire Lasers

The basic object investigated in the thesis is the GaAs-AlGaAs core-shell nanowire Laser [26], [27]. Its structure, illustrated in Fig. 2.5, tackles several challenges towards successfully integrating III-V light sources on silicon. Conventional GaAs NWs suffer from a large density of surface states, which cause unwanted non-radiative recombination and a poor luminescence efficiency. By passivating the surface with a material with a larger bandgap, such as  $\text{Al}_x\text{Ga}_{1-x}\text{As}$ , the carriers are unable to interact with the surface. A 5 nm thick layer is sufficient to enhance the NW's luminescence by a factor of  $\sim 10^3$  [41]. The 5 nm thick GaAs cap prevents oxidation of the AlGaAs layer. Another major challenge is the large lattice mismatch between III-V compound semiconductors and silicon (around

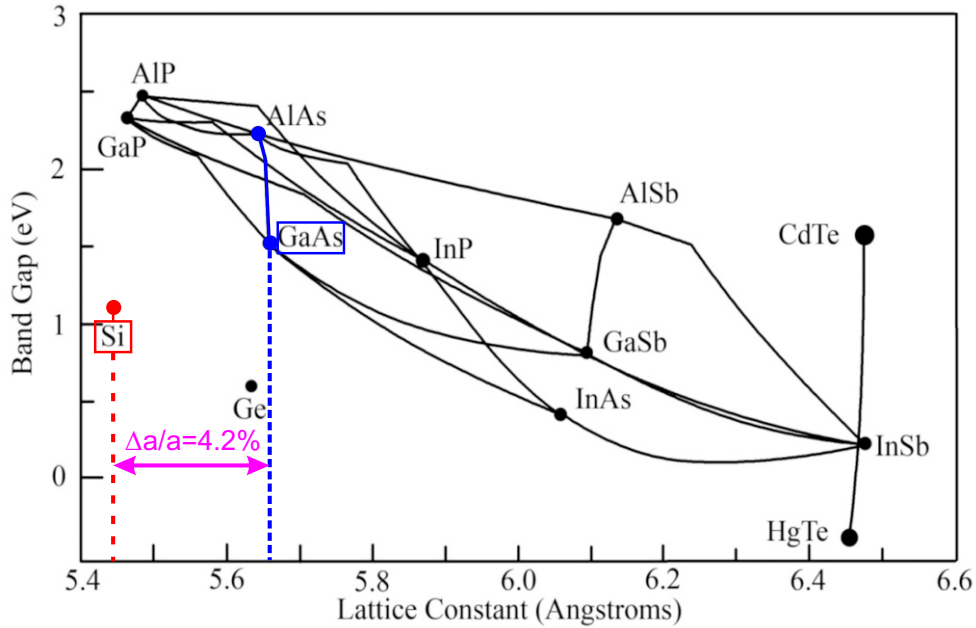


**Figure 2.6:** Lattice constant vs. band gap plot of common semiconductor materials. The large lattice mismatch of 4.2% between GaAs and Si is highlighted. Adapted from [43].

4.2% in the case of GaAs), as shown in Fig. 2.6. However, thanks to the NW's non-planar one-dimensional growth, strain relaxation is strongly modified and potential defects do not propagate further into the NW [42].

There are several growth schemes for GaAs-based NW lasers, based on molecular beam epitaxy (MBE) or metal-organic chemical vapour phase deposition (MOCVD). In our group, the NW structures are grown on a  $\text{SiO}_2$  templated Si (111) substrate in a two-step process using MBE [25].

# Chapter 3

## Waveguide Modes

Nanowires act as low-loss waveguides. Depending on their structure and diameter, they can support several different optical modes. We start by reviewing the basic concepts of optical waveguides, go over an example of a simple step-index optical fiber, and then finally focus on NWs as waveguides.

### 3.1 Basic Concepts

Optical waveguides generally consist of a core and a surrounding cladding. The refractive index of the core  $n_1$  is higher than that of the cladding  $n_0$ , so that the propagating light is confined within the core by total internal reflection, with the critical condition  $\theta \geq \sin^{-1} \frac{n_0}{n_1} = \theta_C$ . In a waveguide, only certain modes can exist. They have to fulfill a phase-matching condition for the propagating angle  $\phi$  [39]:

$$\tan \left( k n_1 a \sin \phi - \frac{m\pi}{2} \right) = \sqrt{\frac{2\Delta}{\sin^2 \phi} - 1}, \quad (3.1)$$

where  $k = 2\pi/\lambda$  is the wavenumber,  $m$  the mode number,  $a$  the core radius,  $n_1$  the core refractive index and  $\Delta = \frac{n_1^2 - n_0^2}{2n_1^2} \cong \frac{n_1 - n_0}{n_1}$  the refractive index difference. The solution with the mode number  $m = 0$  is the *fundamental mode*, while the ones with  $m > 1$  are *higher order modes* (see Fig. 3.1). For a propagating wave,

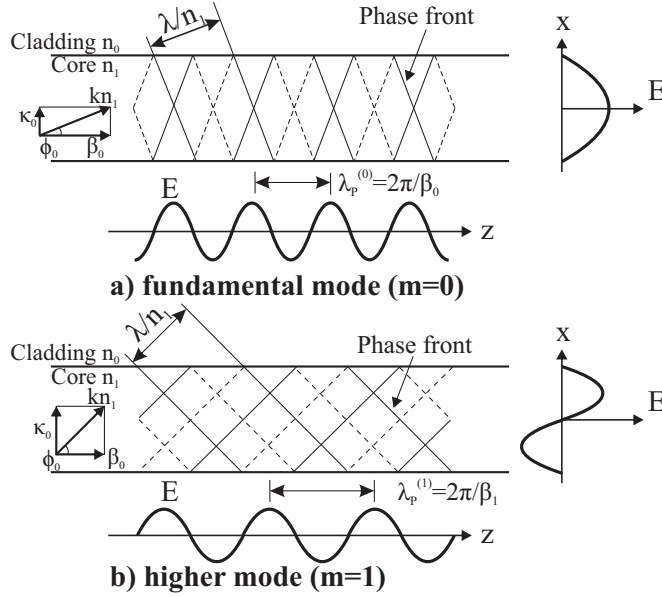


**Figure 3.1:** Formation of modes through the interference of light waves. The solid and dashed lines represent a positive and negative phase front, respectively. The E-field has a maximum (minimum) amplitude where two positive (negative) phase fronts interfere. The amplitude approaches zero near the core-cladding interface, as the positive and negative phase fronts cancel each other out. The field distribution along the transverse  $x$  direction is a standing wave which varies periodically along the  $z$  direction:  $\lambda_p^{(n)} = (\lambda/n_1)/\cos\phi = 2\pi/\beta_n$ .  $\beta_n = kn_1 \cos\phi$  and  $\kappa_n = kn_1 \sin\phi$  are the propagation constants along  $z$  and  $x$ . Schematic adapted from [39].

we define a phase velocity  $v_p = \frac{\omega}{\beta}$  and a group velocity  $v_g = \frac{dz}{dt} = \left. \frac{d\omega}{d\beta} \right|_{\omega=\omega_0}$ , where  $\beta$  is the phase constant. Each mode has an *effective index*, which is the ratio between the phase constant and the vacuum wavenumber,  $n_{\text{eff}} = \frac{\beta}{k_0}$ . The higher order modes have a *cutoff frequency* below which they cannot propagate in the waveguide anymore. This occurs when the effective index of the mode becomes smaller than the refractive index of the surrounding material. The group refractive index is defined as a ratio of the vacuum velocity of light to the group velocity in the medium:  $n_g = \frac{c_0}{v_g} = \frac{d(kn)}{dk} = n + k \frac{dn}{dk} = n - \lambda \frac{dn}{d\lambda}$ .

We can classify basic mode types (propagating along  $z$ ):

- (I) TEM (Transverse Electromagnetic), where  $E_z = 0$  and  $H_z = 0$ ,
- (II) TE (Transverse Electric), where  $E_z = 0$ ,

- (III) TM (Transverse Magnetic), where  $H_z = 0$ ,
- (IV) HE or EH (hybrid or helical modes), which contain all components of electric and magnetic fields and are a linear superposition of TE and TM waves. The order of the letters depends on which of the transversal field components is dominant - electric  $E_z$  in HE and magnetic  $H_z$  in EH.

## 3.2 Step-index Fiber

We follow an example of a step-index fiber [39], consisting of a core with radius  $a$  and a cladding layer, as illustrated in Fig. 3.2.

The EM fields are expressed in cylindrical coordinates as

$$\hat{\mathbf{E}} = \mathbf{E}(r, \theta)e^{i(\omega t - \beta z)} \quad (3.2a)$$

$$\hat{\mathbf{H}} = \mathbf{H}(r, \theta)e^{i(\omega t - \beta z)} \quad (3.2b)$$

Here,  $\mathbf{E}$  is the electric field,  $\mathbf{H}$  the magnetic field,  $\omega$  the angular frequency,  $t$  time and  $\beta$  the phase constant.

We obtain two sets of wave equations:

$$\frac{\partial^2 E_z}{\partial r^2} + \frac{1}{r} \frac{\partial E_z}{\partial r} + \frac{1}{r^2} \frac{\partial^2 E_z}{\partial \theta^2} + (k^2 n(r, \theta)^2 - \beta^2) E_z = 0 \quad (3.3a)$$

$$\frac{\partial^2 H_z}{\partial r^2} + \frac{1}{r} \frac{\partial H_z}{\partial r} + \frac{1}{r^2} \frac{\partial^2 H_z}{\partial \theta^2} + (k^2 n(r, \theta)^2 - \beta^2) H_z = 0 \quad (3.3b)$$

The transverse electromagnetic fields are [39]:

$$E_r = -\frac{i}{k^2 n(r)^2 - \beta^2} \left( \beta \frac{\partial E_z}{\partial r} + \frac{\omega \mu_0}{r} \frac{\partial H_z}{\partial \theta} \right) \quad (3.4a)$$

$$E_\theta = -\frac{i}{k^2 n(r)^2 - \beta^2} \left( \frac{\beta}{r} \frac{\partial E_z}{\partial \theta} - \omega \mu_0 \frac{\partial H_z}{\partial r} \right) \quad (3.4b)$$

$$H_r = -\frac{i}{k^2 n(r)^2 - \beta^2} \left( \beta \frac{\partial H_z}{\partial r} - \frac{\omega \varepsilon_0 n(r)^2}{r} \frac{\partial E_z}{\partial \theta} \right) \quad (3.4c)$$

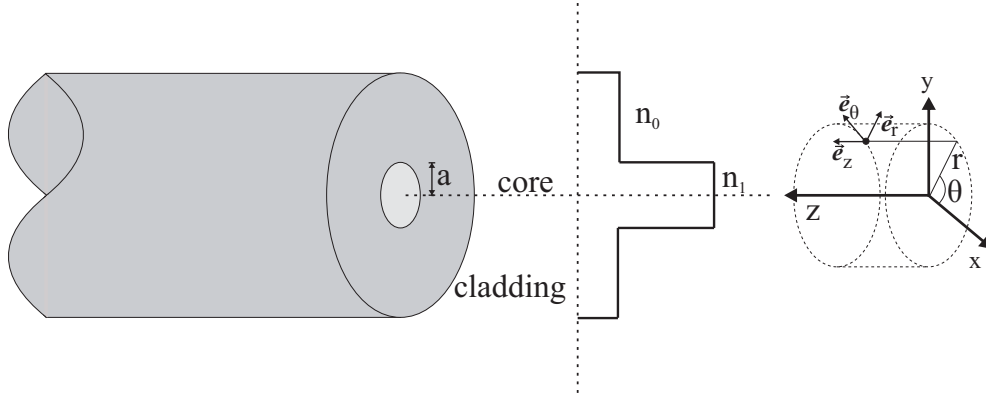


**Figure 3.2:** A step-index fiber consists of a core, surrounded by a cladding. The refractive index of the core  $n_1$  is higher than that of the cladding  $n_0$  to ensure the confinement of modes within the core through total internal reflection.

$$H_\theta = -\frac{i}{k^2 n(r)^2 - \beta^2} \left( \frac{\beta}{r} \frac{\partial H_z}{\partial \theta} + \omega \varepsilon_0 n(r)^2 \frac{\partial E_z}{\partial r} \right) \quad (3.4d)$$

$k$  is the wave number and  $\mu_0$  and  $\varepsilon_0$  stand for vacuum permeability and vacuum permittivity, respectively. In Eqs. 3.4 we already took into account that in axially symmetric fibers,  $n$  is not dependent on the angle  $\theta$ , therefore  $n(r, \theta) \rightarrow n(r)$ . The azimuthal dependency of the EM fields is expressed by  $\cos(l\theta + \psi)$  or  $\sin(l\theta + \psi)$ , where  $l$  is an integer and  $\psi$  the phase. The optical fiber supports TE, TM and hybrid modes.

## TE Modes

When interested in TE Modes,  $E_z = 0$  and we can omit the factors with  $E_z$ , simplifying Eqs. 3.4, while taking into account only the 3.3b wave equation.

The magnetic field in the core and cladding is

$$H_z = \begin{cases} g(r) \\ h(r) \end{cases} \cos(l\theta + \psi) \quad \begin{array}{l} (0 \leq r \leq a) \\ (r > a) \end{array} \quad (3.5)$$

It follows from the boundary conditions that  $H_z$  and  $H_\theta$  are continuous at the

core-cladding interface ( $r = a$ ):

$$g(a) = h(a) \quad (3.6a)$$

$$\frac{i\beta}{k^2 n(a)^2 - \beta^2} \frac{l}{a} g(a) \sin(l\theta + \psi) = \frac{i\beta}{k^2 n_0^2 - \beta^2} \frac{l}{a} h(a) \sin(l\theta + \psi) \quad (3.6b)$$

Since in a step-index fiber,  $n(a) = n_1 \neq n_0$ , the integer  $l$  has to equal 0. The resulting wave equation and EM fields for the TE modes are then

$$\frac{d^2 H_z}{dr^2} + \frac{1}{r} \frac{dH_z}{dr} + (k^2 n(r)^2 - \beta^2) H_z = 0 \quad (3.7)$$

$$E_\theta = \frac{i\omega\mu_0}{k^2 n(r)^2 - \beta^2} \frac{dH_z}{dr} \quad (3.8a)$$

$$H_r = - \frac{i\beta}{k^2 n(r)^2 - \beta^2} \frac{dH_z}{dr} \quad (3.8b)$$

$$E_r = H_\theta = 0. \quad (3.8c)$$

The solutions of the wave equation 3.7 for the field in the core and the cladding are the  $0^{th}$  order Bessel function  $J_0(\kappa r)$  and the modified Bessel functions of the second kind  $K_0(\sigma r)$ , respectively.  $\kappa = \sqrt{k^2 n_1^2 - \beta^2}$  and  $\sigma = \sqrt{\beta^2 - k^2 n_0^2}$  are the wave number in the core and cladding.

After applying the boundary conditions, rearranging and simplifying<sup>1</sup>, we obtain the EM fields for the TE mode:

$$E_r = E_z = H_\theta = 0, \quad (3.9)$$

---

<sup>1</sup> The complete derivation can be found in [39]

(a) Fields in the core ( $0 \leq r \leq a$ ):

$$E_\theta = -i\omega\mu_0 \frac{a}{u} A J_1\left(\frac{u}{a}r\right) \quad (3.10a)$$

$$H_r = i\beta \frac{a}{u} A J_1\left(\frac{u}{a}r\right) \quad (3.10b)$$

$$H_z = A J_0\left(\frac{u}{a}r\right) \quad (3.10c)$$

(b) Fields in the cladding ( $r > a$ ):

$$E_\theta = i\omega\mu_0 \frac{a}{\omega} \frac{J_0(u)}{K_0(w)} A K_1\left(\frac{w}{a}r\right) \quad (3.11a)$$

$$H_r = -i\beta \frac{a}{w} \frac{J_0(u)}{K_0(w)} A K_1\left(\frac{w}{a}r\right) \quad (3.11b)$$

$$H_z = \frac{J_0(u)}{K_0(w)} A K_0\left(\frac{w}{a}r\right) \quad (3.11c)$$

where  $u = \kappa a$  and  $w = \sigma a$ .

## TM Modes

We follow a similar procedure in the case of TM modes, when we set  $H_z = 0$ , simplify Eqs. 3.4 and consider only the 3.3a wave equation. The solutions are again Bessel functions.

The EM fields for TM mode are

$$E_\theta = H_r = H_z = 0, \quad (3.12)$$

(a) Fields in the core ( $0 \leq r \leq a$ ):

$$E_r = i\beta \frac{a}{u} A J_1\left(\frac{u}{a}r\right) \quad (3.13a)$$

$$E_z = A J_0\left(\frac{u}{a}r\right) \quad (3.13b)$$

$$H_\theta = j\omega\varepsilon_0 n_1^2 A J_1\left(\frac{u}{a}r\right) \quad (3.13c)$$

(b) Fields in the cladding ( $r > a$ ):

$$E_r = -i\beta \frac{a}{w} \frac{J_0(u)}{K_0(w)} AK_1\left(\frac{w}{a}r\right) \quad (3.14a)$$

$$E_z = \frac{J_0(u)}{K_0(w)} AK_0\left(\frac{w}{a}r\right) \quad (3.14b)$$

$$H_\theta = -i\omega\varepsilon_0 n_0^2 \frac{a}{w} \frac{J_0(u)}{K_0(w)} AK_1\left(\frac{w}{a}r\right) \quad (3.14c)$$

## Hybrid Modes

In hybrid HE or EH modes, both the axial components  $E_z$  and  $H_z$  are non-zero. The solutions for the wave equations 3.3a and 3.3b are now a product of  $l^{\text{th}}$  order Bessel functions and  $\cos(l\theta + \psi)$  or  $\sin(l\theta + \psi)$ .

The EM field components are in this case

(a) Fields in the core ( $0 \leq r \leq a$ ):

$$E_r = -\frac{ia^2}{u^2} \left[ A\beta \frac{u}{a} J'_n\left(\frac{u}{a}r\right) + C\omega\mu_0 \frac{n}{r} J_n\left(\frac{u}{a}r\right) \right] \cos(l\theta + \psi) \quad (3.15a)$$

$$E_\theta = -\frac{ia^2}{u^2} \left[ -A\beta \frac{n}{r} J_n\left(\frac{u}{a}r\right) - C\omega\mu_0 \frac{u}{a} J'_n\left(\frac{u}{a}r\right) \right] \sin(l\theta + \psi) \quad (3.15b)$$

$$E_z = AJ_n\left(\frac{u}{a}r\right) \cos(l\theta + \psi) \quad (3.15c)$$

$$H_r = -\frac{ia^2}{u^2} \left[ A\omega\varepsilon_0 n_1^2 \frac{n}{r} J_n\left(\frac{u}{a}r\right) + C\beta \frac{u}{a} J'_n\left(\frac{u}{a}r\right) \right] \sin(l\theta + \psi) \quad (3.15d)$$

$$H_\theta = -\frac{ia^2}{u^2} \left[ A\omega\varepsilon_0 n_1^2 \frac{u}{a} J'_n\left(\frac{u}{a}r\right) + C\beta \frac{n}{r} J_n\left(\frac{u}{a}r\right) \right] \cos(l\theta + \psi) \quad (3.15e)$$

$$H_z = CJ_n\left(\frac{u}{a}r\right) \sin(l\theta + \psi) \quad (3.15f)$$

(b) Fields in the cladding ( $r > a$ ):

$$E_r = \frac{ia^2}{w^2} \left[ A\beta \frac{w}{a} K'_n\left(\frac{w}{a}r\right) + C\omega\mu_0 \frac{n}{r} K_n\left(\frac{w}{a}r\right) \right] \frac{J_n(u)}{K_n(w)} \cos(l\theta + \psi) \quad (3.16a)$$

$$E_\theta = \frac{ia^2}{w^2} \left[ -A\beta \frac{n}{r} K_n\left(\frac{w}{a}r\right) - C\omega\mu_0 \frac{w}{a} K'_n\left(\frac{w}{a}r\right) \right] \frac{J_n(u)}{K_n(w)} \sin(l\theta + \psi) \quad (3.16b)$$

$$E_z = A \frac{J_n(u)}{K_n(w)} K_n\left(\frac{w}{a}r\right) \cos(l\theta + \psi) \quad (3.16c)$$

$$H_r = \frac{ia^2}{w^2} \left[ A\omega\varepsilon_0 n_0^2 \frac{n}{r} K_n\left(\frac{w}{a}r\right) + C\beta \frac{w}{a} K'_n\left(\frac{w}{a}r\right) \right] \frac{J_n(u)}{K_n(w)} \sin(l\theta + \psi) \quad (3.16d)$$

$$H_\theta = \frac{ia^2}{w^2} \left[ A\omega\varepsilon_0 n_0^2 \frac{w}{a} K'_n\left(\frac{w}{a}r\right) + C\beta \frac{n}{r} K_n\left(\frac{w}{a}r\right) \right] \frac{J_n(u)}{K_n(w)} \cos(l\theta + \psi) \quad (3.16e)$$

$$H_z = C \frac{J_n(u)}{K_n(w)} K_n\left(\frac{w}{a}r\right) \sin(l\theta + \psi) \quad (3.16f)$$

### 3.3 Nanowire as a Waveguide

Due to the high refractive index contrast between the active and surrounding medium, a nanowire acts as a low-loss waveguide [25]. Depending on its structure and diameter, it can support several TE, TM and HE/EH optical modes. Each of the modes has a characteristic field profile and the modes can be determined easily by observing the transversal field components. While helical HE/EH modes have both the electric and magnetic field components along the nanowire axis, TE and TM modes only have magnetic or electric field components along the waveguide, respectively. We follow the nomenclature from optical waveguides [44]: the letters denote the type of the mode, the numbers describe the azimuthal and radial symmetry of the mode, and the index a or b is added in cases with two degenerated modes due to the hexagonal symmetry of the nanowire. This is illustrated on an example of the HE31<sub>b</sub> mode, Fig. 3.3.

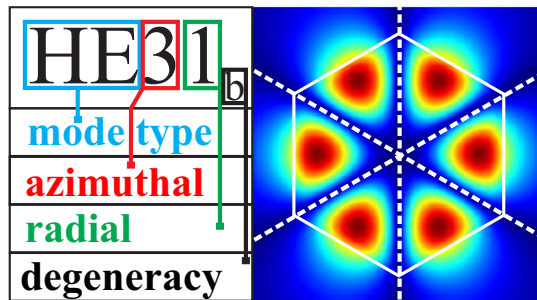


**Figure 3.3:** Nomenclature illustrated on a simple example. We can determine the mode by observing the  $|E_z|$ , transversal electric field component. In this case, it is a hybrid **HE** mode, with a dominant  $|E_z|$  component. In the azimuthal direction, there are six periodic peaks, which means the geometry can be split symmetrically with **3** axes (dashed lines). In the radial direction (from the center of the nanowire outwards), there is only one peak, therefore the radial number is **1**. The index **b** denotes the degeneracy of the mode - there is also an  $\text{HE}31_a$  mode, where the field peaks are positioned in the vertices of the hexagon.

In Fig. 3.4 and Fig. 3.5 we plot intensity profiles of the transversal electric field component  $|E_z|$  and the electric field intensity  $|\mathbf{E}|$  of guided modes for a nanowire with radius 200 nm. The Figures are positioned side-by-side on consecutive pages for an easier comparison.

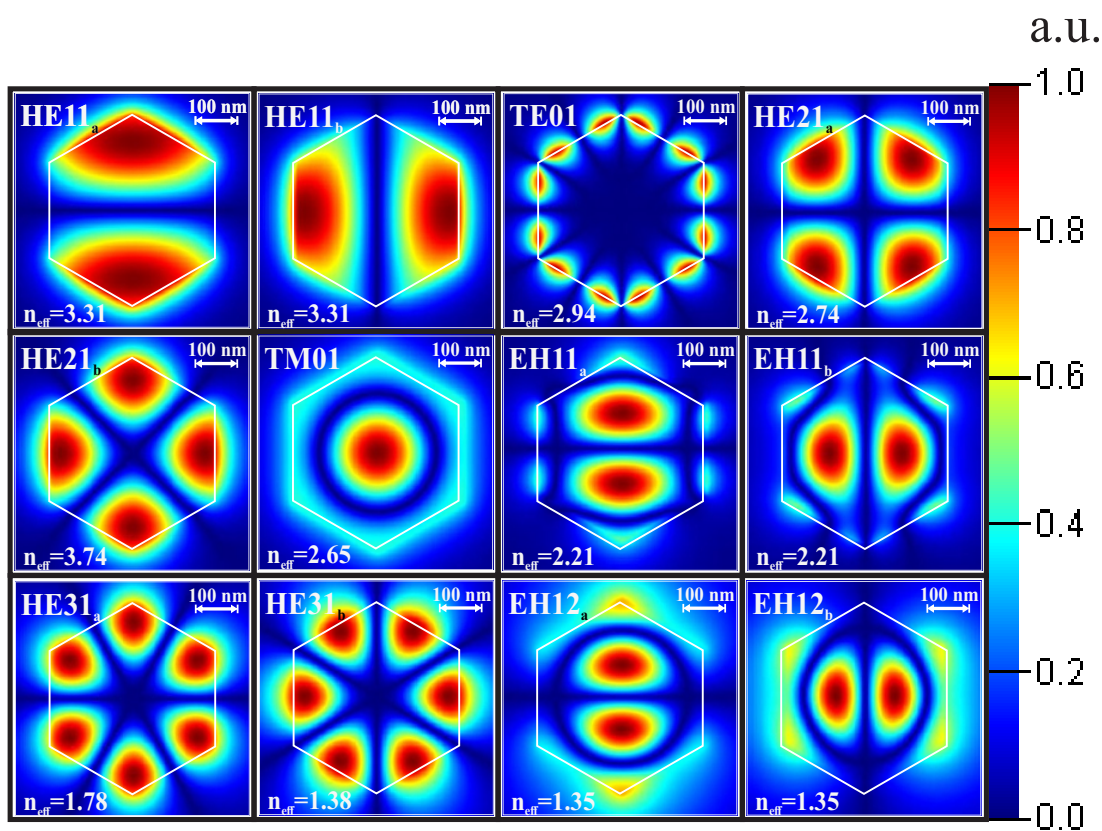


**Figure 3.4:** Intensity profiles of the transverse electric field component  $|E_z|$  of guided modes and the corresponding effective refractive indices  $n_{\text{eff}}$  for a nanowire with radius 200 nm. The field values are normalized to 1.

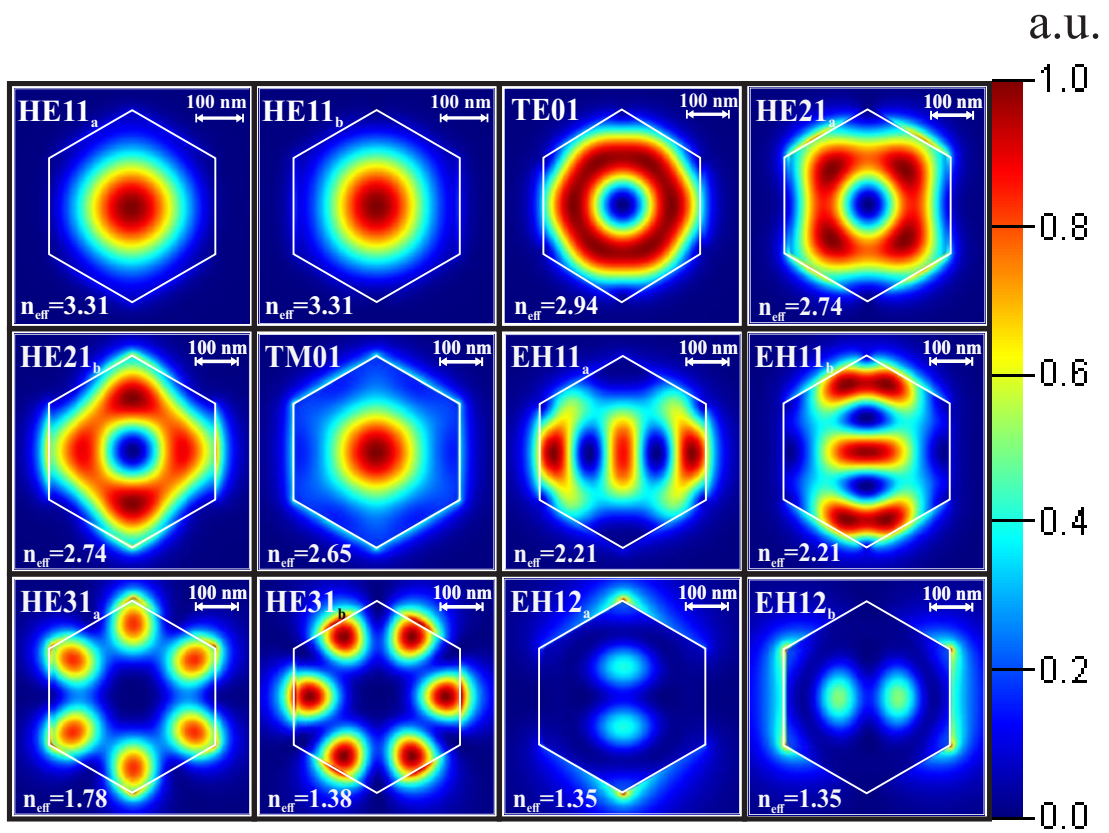


**Figure 3.5:** Electric field intensity  $|E|$  profiles of guided modes and the corresponding effective refractive indices  $n_{\text{eff}}$  for a nanowire with radius 200 nm. The field values are normalized to 1.



# Chapter 4

## Chiral Optics

One of the primary goals in quantum optics is to develop a complete set of techniques for the control of light-matter interactions, even on the single quantum level, while preventing undesired effects leading to decoherence. Strong light confinement in state-of-the-art photonic nanostructures can lead to direction- and polarization-dependent effects, violating reciprocity, so that backward and forward propagation are not identical [45].

In this chapter, we first present a short review of the fundamental chiral processes, have a look at a few effects arising from strong spatial confinement of light and finally discuss spin-direction locking and its use for unidirectional waveguide coupling, which is also interesting in the context of NWs integrated on Si waveguides. One can envision that unidirectional coupling could prove useful in selecting the light coupling path dynamically in future photonic circuits.

### 4.1 Chirality Basics

The word chiral originates from the Greek  $\chi\epsilon\iota\rho$  ("kheir"), which stands for hand. The latter is a familiar *chiral object*, i.e., it is distinguishable from its mirror image. Chirality is important in several branches of science, e.g. with chiral molecules in chemistry. Chiral optics is an emerging discipline dealing with asymmetrical phenomena in the nanoscale optics regime.

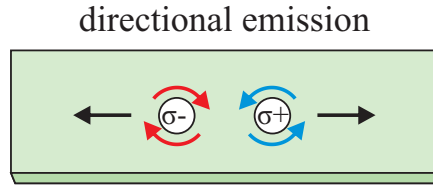


**Figure 4.1:** Depending on the polarization  $\sigma_+$  or  $\sigma_-$ , light is emitted either in the left or right direction. In other words, we get a directional excitation of waveguide modes. Adapted from [45].

An exemplary case of a one-dimensional quantum emitter shows that chiral interfaces affect light-matter interactions on a fundamental level, enabling directional photon emission, absorption and scattering [45]. Consequently, non-reciprocal light propagation is possible. An interesting application is the polarization-dependent directional excitation of waveguide modes, see Fig. 4.1. Interestingly, such effects can be expanded to quantum many-body systems, where the interaction between several quantum emitters is channeled by the waveguide, achieving directional emission, which could lead to the realization of *cascaded quantum systems* [46].

## 4.2 Light Angular Momenta

It has been known that light carries optical angular momentum, which can be separated into spin and orbital components [47].

Let us summarize the explanation from [48] for the case of a paraxial beam propagating along the  $z$  axis. A circularly polarized beam has a spin angular momentum  $\mathbf{S}$  (SAM), dependent on the polarization helicity  $\sigma \in (-1, 1)$  which marks the degree of circular polarization, and is aligned with the propagation direction. Values of  $\sigma = -1$  and  $\sigma = 1$  stand for left- and right-handed circular polarization. SAM has the value of  $\sigma\hbar$  per photon, where  $\hbar$  is the reduced Planck's constant,  $\hbar = h/2\pi$ .

Orbital angular momentum, on the other hand, is associated with the spatial distribution of the optical field. Light beams with helical wavefronts (optical

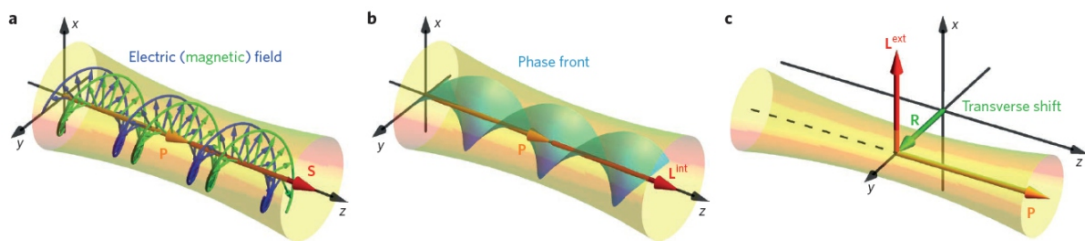


**Figure 4.2:** (a) Spin angular momentum (SAM) points in the direction of propagation for the case of a right-hand circularly polarized beam with helicity  $\sigma = 1$  and has a value of  $\sigma\hbar$  per photon. (b) Surface of a constant phase with a helical wavefront shape, illustrating the intrinsic orbital angular momentum (IOAM) for a vortex beam with a value of  $l = 2$ . (c) Extrinsic orbital angular momentum (EOAM) is analogous to mechanical angular momentum of classical particles and depends on the offset between the beam axis and coordinate system origin. Taken from [48].

vortex beams) have a non-zero intrinsic angular orbital momentum  $\mathbf{L}^{int}$  (IOAM), which is aligned with the propagation direction and determined by the so-called vortex charge  $l = 0, \pm 1, \dots$ , which describes the azimuthal phase dependence. IOAM has values of  $l\hbar$  per photon. Extrinsic orbital angular momentum  $\mathbf{L}^{ext}$  (EOAM) is similar to a classical (mechanical) angular momentum and depends only on the position of the light beam in the coordinate system. It is determined by the cross-product of the position and momentum vector.

The optical angular momenta are illustrated in Fig. 4.2 and summarized in the following equations:

$$\mathbf{S} = \sigma \frac{\mathbf{P}}{P}, \quad \mathbf{L}^{int} = l \frac{\mathbf{P}}{P}, \quad \mathbf{L}^{ext} = \mathbf{R} \times \mathbf{P}, \quad (4.1)$$

where  $\mathbf{P}$  is the momentum vector and the values per photon are expressed in  $\hbar = 1$  units.

### 4.3 Transverse Spin

Nanophotonic devices can control light at sub-wavelength scales. Light is often strongly transversely confined, i.e., perpendicularly to the direction of propaga-

tion, which leads to a longitudinal field component oscillating along the direction of propagation.

We can follow a simple example from [45], where a focused light beam with wavevector  $k = 2\pi/\lambda$  and frequency  $\omega$  is propagating along  $\pm z$ . The electric field is

$$\mathbf{E}_{\pm}(\mathbf{r}, t) = \frac{\mathcal{E}_{\pm}(\mathbf{r})}{2} e^{-i(\omega t \mp kz)} + c.c., \quad (4.2)$$

where  $\mathcal{E}_{\pm}(\mathbf{r})$  is the complex amplitude,  $\mathbf{r}$  the position vector and c.c. the complex conjugate. Following is a derivation of the relation between the longitudinal and transversal electric field components to obtain the polarization of the propagating fields. We first apply Gauss' law  $\nabla \cdot \mathbf{E} = \frac{\rho}{\varepsilon_0} = 0 \Big|_{\rho=0}$ , where  $\rho$  stands for charge density (in our case,  $\rho = 0$ ) and  $\varepsilon_0$  is the vacuum permittivity. We get the following equation:

$$\frac{1}{2} \frac{\partial \mathcal{E}_{\pm,x}}{\partial x} e^{-i(\omega t \mp kz)} + \frac{1}{2} \frac{\partial \mathcal{E}_{\pm,y}}{\partial y} e^{-i(\omega t \mp kz)} + \frac{1}{2} \frac{\partial \mathcal{E}_{\pm,z}}{\partial z} e^{-i(\omega t \mp kz)} \pm \frac{\mathcal{E}_{\pm,z}}{2} i k e^{-i(\omega t \mp kz)} = 0 \quad (4.3)$$

By assuming a slowly varying amplitude along  $z$ , we can neglect the part with  $\frac{\partial \mathcal{E}_{\pm,z}}{\partial z}$  and express  $\mathcal{E}_{\pm,z}$ :

$$\mathcal{E}_{\pm,z} = \mp \frac{i}{k} \left( \frac{\partial \mathcal{E}_{\pm,x}}{\partial x} + \frac{\partial \mathcal{E}_{\pm,y}}{\partial y} \right) \quad (4.4)$$

The longitudinal ( $\mathcal{E}_{\pm,z}$ ) and transverse ( $\mathcal{E}_{\pm,x}, \mathcal{E}_{\pm,y}$ ) components become comparable when the transverse components vary significantly over a length scale of  $1/k = \lambda/(2\pi)$  (in the wavelength scale). The complex factor  $\mp i$  means a  $\mp \pi/2$  phase shift of  $\mathcal{E}_{\pm,z}$  compared to the transverse components. As a consequence, in a strongly confined region, even a linearly polarized beam becomes elliptically polarized and  $\mathbf{E}$  rotates in the plane parallel to the direction of propagation  $\pm z$ .

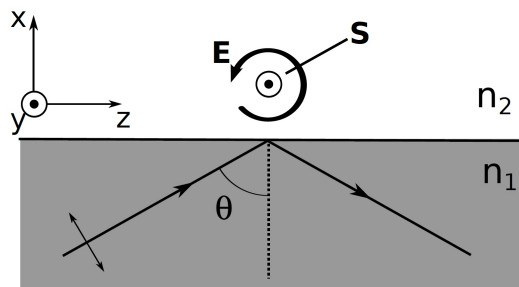


**Figure 4.3:** Total internal reflection at a dielectric interface,  $n_1 > n_2$ . In the upper medium, an evanescent field is formed. The electric field is locally elliptically polarized and we get a transverse spin component which depends on the direction of the incident light ray. Taken from [45].

The spin angular momentum density of the electric field is defined as [49]:

$$\begin{aligned} \mathcal{S}_{\mathcal{E}} &= -\frac{i\varepsilon_0}{2\omega} \mathcal{E}^* \times \mathcal{E} = -\frac{i\varepsilon_0}{2\omega} \begin{vmatrix} \hat{x} & \hat{y} & \hat{z} \\ \mathcal{E}_{\pm,x}^* & \mathcal{E}_{\pm,y}^* & \mathcal{E}_{\pm,z}^* \\ \mathcal{E}_{\pm,x} & \mathcal{E}_{\pm,y} & \mathcal{E}_{\pm,z} \end{vmatrix} \\ &= -\frac{i\varepsilon_0}{2\omega} [\mathcal{E}_{\pm,y}^* \mathcal{E}_{\pm,z} - \mathcal{E}_{\pm,y} \mathcal{E}_{\pm,z}^*, -\mathcal{E}_{\pm,x}^* \mathcal{E}_{\pm,z} + \mathcal{E}_{\pm,x} \mathcal{E}_{\pm,z}^*, \mathcal{E}_{\pm,x}^* \mathcal{E}_{\pm,y} - \mathcal{E}_{\pm,x} \mathcal{E}_{\pm,y}^*]^T \end{aligned} \quad (4.5)$$

Here,  $\mathcal{E}^*$  is the complex conjugate of  $\mathcal{E}$ . As we have an  $\mathcal{E}_{\pm,z}$  component, we get a *transverse spin component*  $\mathcal{S}_{\mathcal{E}}^{\text{trans}}$  in the  $xy$  plane. As we can deduce from Eq. 4.4, the transverse spin changes its sign when the propagation direction is reversed. In Fig. 4.3, a simple example of total internal reflection at a dielectric interface illustrates how transverse spin is formed.

## 4.4 Spin-direction Locking

The fact that the transverse spin in nanophotonic devices changes sign based on the direction of light propagation leads to the so-called *spin-direction locking*. It turns out that any waveguide mode has regions with evanescent field tails near the edges of the waveguide, where this effect can be utilized.

In another example from [48], we consider an evanescent wave, propagating

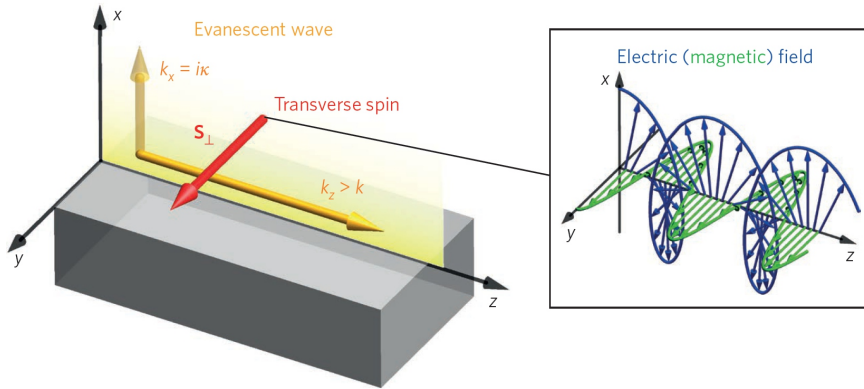


**Figure 4.4:** Each waveguide mode has evanescent field tails near the boundary to the surrounding material. The evanescent field propagates along the waveguide and decays in the perpendicular direction. To satisfy the transversality condition  $\mathbf{E} \cdot \mathbf{k} = 0$ , we get a longitudinal,  $\pi/2$  shifted  $E_z$  field component, causing the electric field to rotate in the propagation plane and generating a transverse spin component, which flips orientation if the mode switches its propagation direction. Taken from [48].

at the edge of a waveguide along the  $z$ -axis, which is attenuated in the  $x$ -direction. It can be described as a plane wave,  $\mathbf{k} = k_z \mathbf{z} + i\kappa \mathbf{x}$ , where  $\kappa$  stands for attenuation. From the transversality condition  $\mathbf{E} \cdot \mathbf{k} = 0$  we can again conclude that there is a  $\pi/2$  phase-shifted longitudinal  $E_z$  component,  $E_z = -i(\frac{\kappa}{k_z})E_x$ , resulting in the rotation of electric field  $\mathbf{E}$  in the propagation ( $xz$ ) plane and generating a transversal spin component. The conditions are illustrated in Fig. 4.4. If the mode is propagating in the opposite direction, the transversal spin flips its sign. In other words, the transverse spin is "locked" with the evanescent wave propagation direction, hence the name spin-direction locking. This phenomenon is connected also with the quantum spin-Hall effect for photons [50].

## 4.5 Unidirectional Coupling in Waveguides

### Successful Demonstrations

Spin direction-locking has been successfully utilized to demonstrate a unidirectional excitation of waveguide modes. Several groups have reached important

milestones in this regard in the recent years, from using classical emitters in dielectric waveguides [51] and photonic crystals [52] to employing well-defined spin states in single quantum dots [53, 54] and manipulating surface plasmon polaritons in metallic waveguides [55, 56]. All of the proposed techniques are fundamentally based on the same principle - incident light, which is usually circularly polarized, is propagating perpendicularly to the waveguide and has the usual spin angular momentum (SAM) which depends on the handedness and points in the direction of propagation. Through a scatterer, which acts as a point-like circular dipole source, this light is coupled to the evanescent tails of the waveguide mode. The mode is excited in such a way that the SAM of the incident light and of the evanescent field are parallel. This means the latter propagates in only one of both possible directions, depending on the circular polarization of the incident light. Figs. 4.5 (a, b) illustrate examples of unidirectional coupling to plasmonic and dielectric waveguides.

## Rectangular Si Waveguide

In order to gain a more thorough insight into how to achieve unidirectional coupling, let us follow a simple example of a plain rectangular silicon waveguide as presented in [57].

We assume the waveguide consists only of a silicon core which is surrounded by air ( $n = 1$ ). It has a rectangular cross-section with a width of 450 nm and a height of 220 nm, with its axis pointing in the  $z$ -direction. The employed wavelength  $\lambda = 1550$  nm lies in the telecommunications bandwidth. We first consider the fundamental TE-like mode, which has a significant  $E_x$  component. As explained in section 4.3, in nanophotonic structures exhibiting strong light confinement we also get a substantial longitudinal field component  $E_z$  due to significant gradients of the transverse  $E_x$  and  $E_y$  components. The imaginary component of  $E_z$  is displayed in Fig. 4.6 (a). The magnitude of  $E_z$  is comparable to  $E_x$  and has a similar shape, while phase shifted by  $\pi/2$  and antisymmetric with regard to the  $x = 0$  axis. Figs. 4.6 (b, c) are the plots of the ratio between the

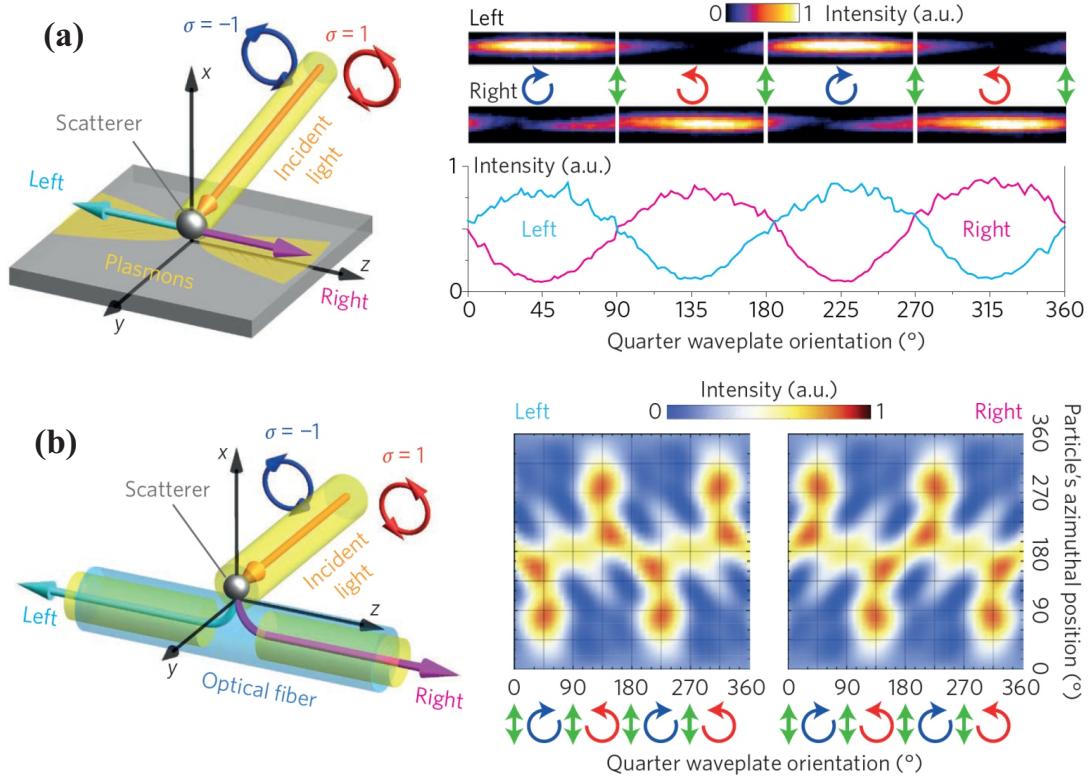


**Figure 4.5:** (a) Unidirectional coupling of incident light to surface plasmon modes in a metallic waveguide. The right panel shows the dependency of the coupling to the right or left direction on the polarization of the incident light, controlled by the quarter wave plate orientation. We observe maxima when the light is purely left- or right-hand circularly polarized. In (b) is an analogous case for an optical fiber and conventional dielectric modes. In both cases the scatterer is a nanoparticle, positioned on the waveguide. The images were taken from [48] (left side), [56] ((a) right side) and [51]((b) right side).

longitudinal and transverse field components. There are regions where the longitudinal  $E_z$  component has much higher values than the transversal counterparts. This occurs near the waveguide-air interface, where there is a large index change resulting in a large change (gradient) in the  $E_x$  component. As shown in Eq. 4.4, a larger gradient means a higher value of the  $E_z$  component.

Spin-controlled unidirectional excitation of guided waveguide modes can generally be achieved by placing a point dipole source with a dipole moment  $\mathbf{d}$  in the appropriate position. The power of light coupled into a given mode is propor-

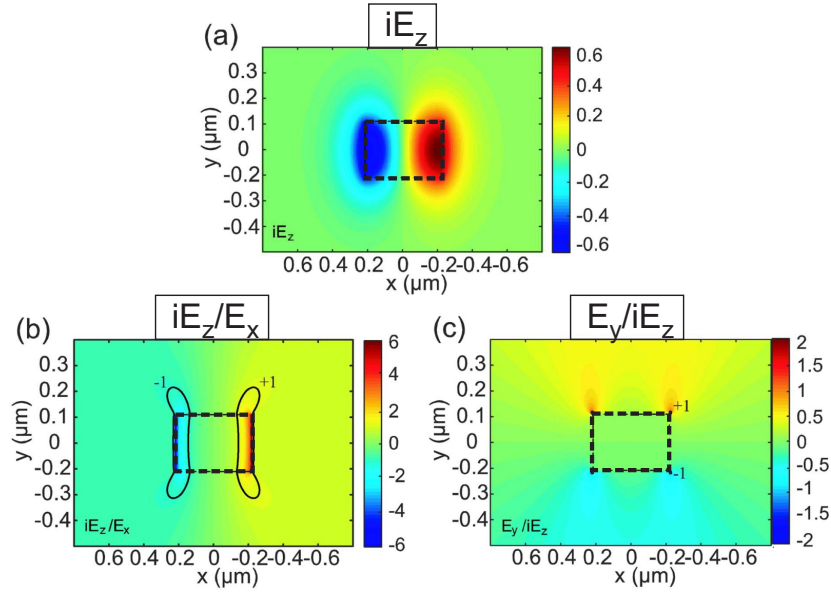


**Figure 4.6:** (a) Imaginary part of the longitudinal  $E_z$  component.  $E_z$  is comparable in size to  $E_x$ , phase shifted by  $\pi/2$  and antisymmetric around the  $x = 0$  axis. (b) and (c) show the ratio between the imaginary part of the  $E_z$  component and  $E_x$  or  $E_y$  components, respectively. The contours mark the region where the ratio is equal to 1, meaning the field is locally circularly polarized. The values of electric fields in the plot are normalized to the  $E_x$  value in the coordinate system origin. Results and plots taken from [57].

tional to  $I_{\text{coupl}} \propto |\mathbf{d}^* \cdot \mathbf{E}|^2$ , which can be set to zero with the dipole polarization and position [51]. The mode is therefore only excited in one direction, which can be switched by flipping the dipole moment between  $\mathbf{d}$  and  $\mathbf{d}^*$ . In Figs. 4.6 (b, c), the contours where the ratio between the longitudinal and transversal components is 1 are outlined in black color. There, the electric field is circularly polarized in the  $xz$  and  $yz$  planes, respectively. By placing a circularly polarized point dipole in these regions, the fundamental mode will be excited in one or another direction of the waveguide. Simulation results from [57] for the fundamental TE-like mode show a good unidirectional coupling, see Figs. 4.7(b, c).

One problem, however, is that the excitation conditions are different for each of the waveguide modes. If we think of the TM-like mode, its field components are similar to those of the TE-like mode, only rotated by  $90^\circ$  around the  $z$  direction. Consequently, the maps of field ratios are different so although we correctly place

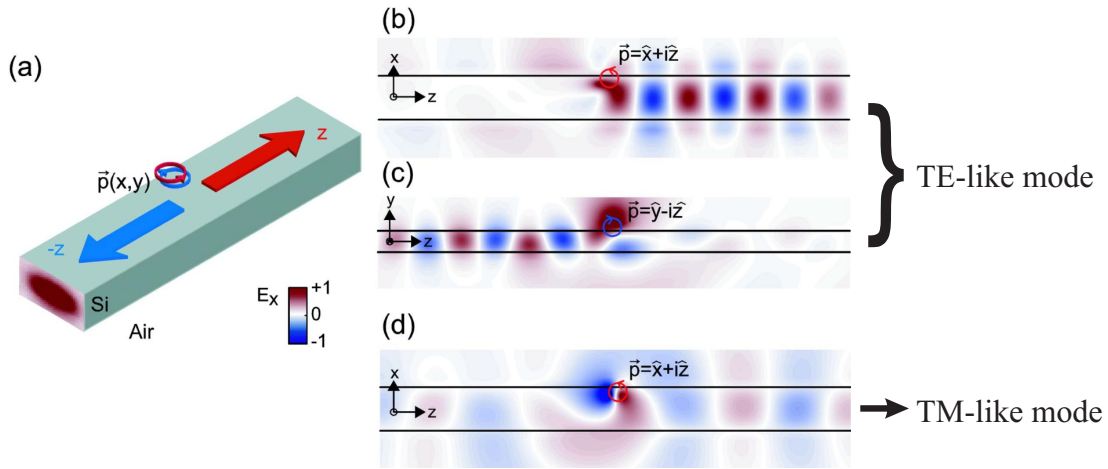


**Figure 4.7:** (a) Schematic of unidirectional coupling of waveguide modes by placing a circularly polarized dipole in the appropriate position. (b) and (c) show the  $E_x$  component (TE-like mode) for the cases of using a dipole polarized in the  $xz$  and  $yz$  plane, respectively. For the TE mode we get a good unidirectional coupling, as opposed to the TM mode (d), which has completely different condition for unidirectional excitation. Results and plots taken from [57].

the dipole for a unidirectional excitation of the TE-like mode, the light is coupled to the TM-like mode in both directions, (Fig. 4.7 (d)). This has to be taken into account when dealing with spin-orbit coupling in multimode waveguides.

# Chapter 5

## Numerical Methods

The results presented in this thesis were obtained using the numerical simulation tools COMSOL Multiphysics, Lumerical MODE Solutions and Lumerical FDTD Solutions. In this chapter, the basic concepts of the underlining numerical algorithms, namely the Finite Element Method (FEM), Finite Difference Eigenmode (FDE) and Finite-Difference Time-Domain (FDTD) are explained.

### 5.1 Finite Element Method

The Finite Element Method is a widely employed numerical technique in various fields of science and engineering. The vast majority of physical processes can be described using partial differential equations (PDEs), which often do not have an analytical solution. In turn, an approximate solution can be computed through numerical model equations [58]. In FEM, the simulation region is divided into *finite elements* - smaller interconnected subregions. The method is very appropriate for solving boundary value problems, which can be split into equilibrium/steady-state/time-independent problems, eigenvalue problems and transient problems.

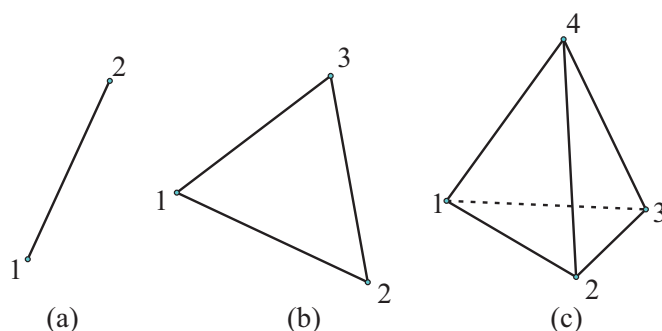


**Figure 5.1:** Examples of possible shapes of the finite elements: (a) linear segment connecting two nodes (1D), (b) triangle (2D), (c) tetrahedron (3D).

### 5.1.1 Procedure

The FEM implementations follow a sequence of several steps (based on [59]):

#### Domain Discretization

The initial step is to divide the domain into discrete finite elements. Their type and shape depends on the geometry of the simulated domain (for basic shapes see Fig. 5.1). The most often used shapes, employed also by COMSOL, are triangles and tetrahedrons in 2D and 3D, respectively. The chosen size of the elements is connected to the solution convergence and results in the well-known trade-off between accuracy and computation time. The location of nodes is crucial and in complex geometries with several different materials, a non-uniform mesh is required to accurately model discontinuities.

#### Interpolation Model Selection

The solution is approximated in each of the elements by using a simple interpolation function, usually a polynomial. A higher order polynomial generally means a more accurate approximation. We can illustrate the principle on a simple 1D case from [58]. Let  $u$  be a function, dependent on variable  $x$ . It can be approximated

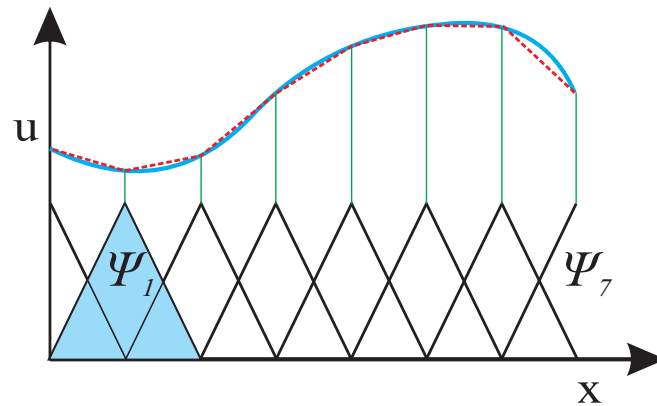


**Figure 5.2:** Interpolation of function  $u$  (blue line) with a linear combination approximation  $u_h = \sum_i u_i \psi_i$  (red line).

by function  $u_h \approx u$  by a linear combination

$$u_h = \sum_i u_i \psi_i, \quad (5.1)$$

where  $u_i$  are the coefficients and  $\psi_i$  the basis functions. In our case,  $\psi_i$  is a linear function with value 1 at its node and 0 at neighboring nodes. The interpolation is illustrated in Fig. 5.2. Realistic problems are much more complex, with higher order interpolation functions and elements in 2D and 3D.

### Element Characteristic Matrices and Load Vectors Derivation

Next, we need to transform the problem equations to a discrete formulation and derive the characteristic matrices and vectors. There are several different approaches [59].

In the *direct method*, we isolate each element and derive the equations, e.g. the forces and displacements on each of the nodes, and write them in a matrix form  $[k]\mathbf{u} = f$ , where  $[k]$  is the characteristic matrix.

In the *variational approach*, the problem is translated to a variational form, where the task is to determine the function  $f(x)$  to find the maximum/minimum of the

functional

$$I = \int_{x_1}^{x_2} F(x, f, f_x, f_{xx}, \dots) dx, \quad (5.2)$$

where  $x$  is the independent variable,  $f_x = \frac{df}{dx}$ ,  $f_{xx} = \frac{d^2f}{dx^2}$ , ... , are derivatives, while  $I$  and  $F$  are functionals.

Using the *weighted residual approach*, the FEM equations are derived directly from the problem's differential equations. In this context, one can employ several different techniques, e.g. the Galerkin Method [60] or Least Squares Method [61].

### Element Equations Assembly

Once we have the element matrices and vectors, we need to connect them to form the entire system. The first step is to transform the coordinates to a common, global coordinate system. In the following assembly stage, boundary conditions have to be taken into account and the values at nodes connecting several elements must agree. We end up with a global system of equations.

### Solution of Equations

In the final stage, the solution, i.e., the values of the physical quantities of interest at each node are obtained, where the method used depends on the type of the problem [59].

For equilibrium problems

$$[A]\mathbf{X} = \mathbf{b} \quad (5.3)$$

with boundary conditions

$$[B]\mathbf{X} = \mathbf{g}, \quad (5.4)$$

we can use e.g. Gaussian Elimination or the Choleski Method.

Eigenvalue problems

$$[A]\mathbf{X} = \lambda \mathbf{bX} \quad (5.5)$$

with boundary conditions

$$[C]\mathbf{X} = \mathbf{g} \quad (5.6)$$

can be solved with the Jacobi or Power Method, among others.

Transient problems

$$[A]\frac{d^2\mathbf{X}}{dt^2} + [B]\frac{d\mathbf{X}}{dt} + [C]\mathbf{X} = \mathbf{F}(\mathbf{X}, t), \quad t > 0 \quad (5.7)$$

that adhere to boundary conditions

$$[D]\mathbf{X} = \mathbf{g} \quad t \geq 0 \quad (5.8)$$

and initial conditions

$$\mathbf{X} = \mathbf{X}_0, \quad t = 0 \quad (5.9a)$$

$$\frac{d\mathbf{X}}{dt} = \mathbf{Y}_0, \quad t = 0 \quad (5.9b)$$

can be tackled with Runge-Kutta Methods, Direct Integration Methods etc.

### 5.1.2 Mode Analysis with COMSOL

We can use COMSOL for mode analyses to numerically calculate the supported waveguide modes and their properties, such as the effective refractive index  $n_{\text{eff}}$ .

After setting the geometrical parameters and material values and constructing the cross-section of the NW structure, the software builds a triangular mesh, which is finer at the edges of the structure and at interfaces of different materials, see Fig. 5.3. The simulations use the Electromagnetic Waves, Frequency

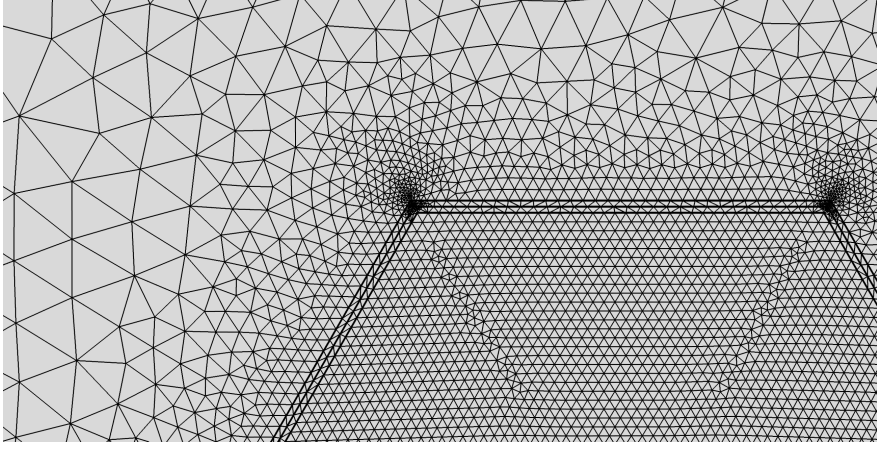


**Figure 5.3:** A detailed view of the auto-generated mesh in COMSOL. Near the edges and vertices of the nanowire, the mesh is finer than in the surrounding regions.

Domain package [62]. The fundamental equations are

$$\nabla \times \mu_r^{-1}(\nabla \times \mathbf{E}) - k_0^2(\varepsilon_r - \frac{i\sigma}{\omega\varepsilon_0})\mathbf{E} = \mathbf{0}, \quad \text{wave equation} \quad (5.10a)$$

$$\lambda = -i\beta - \delta_z, \quad \text{eigenvalue} \quad (5.10b)$$

$$\mathbf{E}(x, y, z) = \hat{\mathbf{E}}(x, y)e^{-ik_z z}. \quad \text{electric field} \quad (5.10c)$$

Here,  $\mu_r$  denotes the relative permeability,  $k_0$  the vacuum wavenumber,  $\sigma$  the conductivity,  $\omega$  the angular frequency,  $\varepsilon_r$  the relative permittivity,  $\varepsilon_0$  the vacuum permittivity,  $\beta$  the propagation constant,  $\delta_z$  the real part of the eigenvalue and  $k_z$  the  $z$ -component of the wave vector. We set zero initial values and apply scattering boundary conditions

$$\mathbf{n} \times (\nabla \times \mathbf{E}) - ik\mathbf{n} \times (\mathbf{E} \times \mathbf{n}) = -\mathbf{n} \times (\mathbf{E}_0 \times (ik(\mathbf{n} - \mathbf{k}_{\text{dir}})))e^{-ik\mathbf{k}_{\text{dir}}}, \quad (5.11)$$

where  $\mathbf{n}$  is the normal vector,  $\mathbf{E}_0$  the incident electric field (set to zero) and  $\mathbf{k}_{\text{dir}}$  the incident wave direction. When the simulation is complete, we obtain results in the form of field profiles of supported modes and their effective refractive indices. An example is shown in Fig. 5.4.

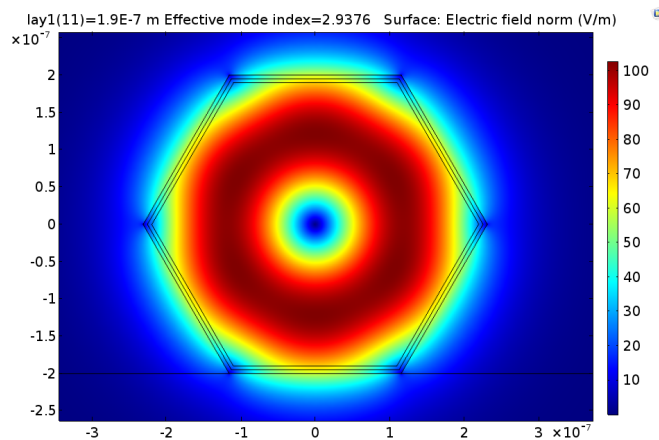


**Figure 5.4:** The solution to the eigenmode problem in COMSOL is the effective refractive index  $n_{\text{eff}}$  and the mode field profiles. Here, an example of the electric field norm  $|\mathbf{E}|$  profile for the TE<sub>01</sub> mode in a 200 nm radius NW.

## 5.2 Finite Differences Methods

The solvers developed by Lumerical Solutions Inc. are based on Finite Differences Methods, namely the Finite Difference Eigenmode (FDE) to determine the supported modes, and Finite-Difference Time-Domain (FDTD) to solve Maxwell's equations in complex geometries in the time domain. They use a rectangular discretization scheme based on the one originally proposed by Yee [63], illustrated in Fig. 5.5.

### 5.2.1 Finite Difference Eigenmode

The Finite Difference Eigenmode solver, embedded in Lumerical MODE Solutions, solves Maxwell's equations on a cross-section of the waveguide and calculates the spatial profiles of supported modes along with their effective index and losses [64].

Its numerical algorithm is based on [65]. The method uses a 2D Yee mesh, see Fig. 5.5(a). The fields are described as  $\mathbf{E}(x, y)e^{i(\beta z - \omega t)}$  and  $\mathbf{H}(x, y)e^{i(\beta z - \omega t)}$ , where  $\beta$  is the propagation constant and  $\omega$  the angular frequency. We use

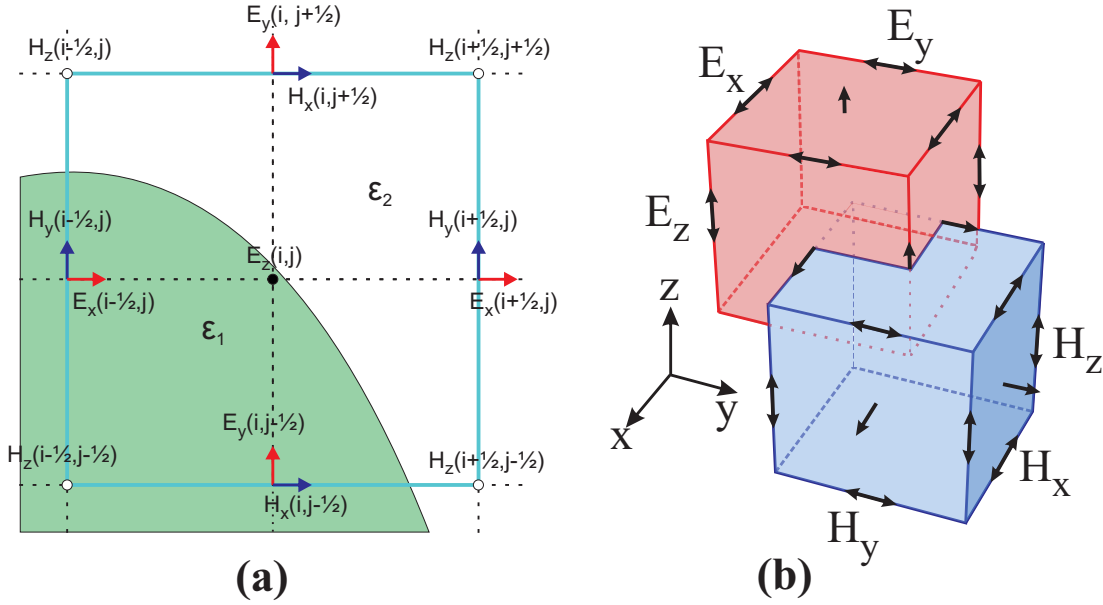


**Figure 5.5:** (a) 2D Yee mesh over a curved dielectric interface. The magnetic and electric fields are discretized over shifted rectangular grids. (b) The basic cells of a 3D Yee mesh. The primary and secondary cell have a partial overlap, making the leapfrog time-stepping scheme an algorithm to implement naturally.

Maxwell's equations

$$\nabla \cdot \mathbf{D} = \rho \quad (5.12a)$$

$$\nabla \cdot \mathbf{B} = 0 \quad (5.12b)$$

$$\nabla \times \mathbf{E} = -\frac{\partial \mathbf{B}}{\partial t} \quad (5.12c)$$

$$\nabla \times \mathbf{H} = \mathbf{J} + \frac{\partial \mathbf{D}}{\partial t} \quad (5.12d)$$

where  $\mathbf{D}$  denotes the electric displacement,  $\rho$  the charge density,  $\mathbf{B}$  the magnetic field,  $\mathbf{E}$  the electric field,  $\mathbf{H}$  the magnetic field strength and  $\mathbf{J}$  the current density. Assuming free space, the charge and current densities  $\rho$  and  $\mathbf{J}$  are zero, so 5.12a

and 5.12d are further simplified. We can rewrite the equations component-wise:

$$i\omega\mu_0 H_x = \frac{\partial E_z}{\partial y} - i\beta E_y \quad (5.13a)$$

$$i\omega\mu_0 H_y = i\beta E_x - \frac{\partial E_z}{\partial x} \quad (5.13b)$$

$$i\omega\mu_0 H_z = \frac{\partial E_y}{\partial x} - \frac{\partial E_x}{\partial y} \quad (5.13c)$$

$$-i\omega\varepsilon_0\varepsilon_r E_x = \frac{\partial H_z}{\partial y} - i\beta H_y \quad (5.14a)$$

$$-i\omega\varepsilon_0\varepsilon_r E_y = i\beta H_x - \frac{\partial H_z}{\partial x} \quad (5.14b)$$

$$-i\omega\varepsilon_0\varepsilon_r E_z = \frac{\partial H_y}{\partial x} - \frac{\partial H_x}{\partial y} \quad (5.14c)$$

where  $\mu_0$  is the vacuum permeability and  $\varepsilon_0$  and  $\varepsilon_r$  the vacuum and relative permittivities, respectively.

In this form, the equations can easily be adapted to the Yee grid by replacing continuum fields with values at discrete points, e.g.  $H_x(x, y) \rightarrow H_x(i, j)$ , where  $(i, j)$  is a point on the grid. The spatial derivatives are rewritten as a difference between the field values of two neighboring vertices, e.g.  $\frac{\partial E_z}{\partial y} \rightarrow \frac{E_z(i, j+1) - E_z(i, j)}{\Delta y}$ . The discrete equations can be translated into matrix form

$$i\omega\mu_0 \begin{bmatrix} \mathbf{H}_x \\ \mathbf{H}_y \\ \mathbf{H}_z \end{bmatrix} = \begin{bmatrix} \mathbf{0} & -i\beta\mathbf{I} & \mathbf{U}_y \\ i\beta\mathbf{I} & \mathbf{0} & -\mathbf{U}_x \\ -\mathbf{U}_y & \mathbf{U}_x & \mathbf{0} \end{bmatrix} \begin{bmatrix} \mathbf{E}_x \\ \mathbf{E}_y \\ \mathbf{E}_z \end{bmatrix} \quad (5.15)$$

$$-i\omega\varepsilon_0 \begin{bmatrix} \varepsilon_{rx} & \mathbf{0} & \mathbf{0} \\ \mathbf{0} & \varepsilon_{ry} & \mathbf{0} \\ \mathbf{0} & \mathbf{0} & \varepsilon_{rz} \end{bmatrix} \begin{bmatrix} \mathbf{E}_x \\ \mathbf{E}_y \\ \mathbf{E}_z \end{bmatrix} = \begin{bmatrix} \mathbf{0} & -i\beta\mathbf{I} & \mathbf{V}_y \\ i\beta\mathbf{I} & \mathbf{0} & -\mathbf{V}_x \\ -\mathbf{V}_y & \mathbf{V}_x & \mathbf{0} \end{bmatrix} \begin{bmatrix} \mathbf{H}_x \\ \mathbf{H}_y \\ \mathbf{H}_z \end{bmatrix} \quad (5.16)$$

Here,  $\mathbf{I}$  is an identity matrix,  $\varepsilon_{rx}$ ,  $\varepsilon_{ry}$  and  $\varepsilon_{rz}$  are matrices of the average refraction

tive index of neighboring cells and  $\mathbf{U}_x$ ,  $\mathbf{U}_y$ ,  $\mathbf{V}_x$  and  $\mathbf{V}_y$  are matrices with element values of -1, 0 or 1, depending on boundary conditions. For example, there are two non-zero diagonals with values  $\pm 1$  when zero boundary conditions apply.

After some rearrangements, the final formulation leads to an eigenvalue problem

$$\begin{bmatrix} \mathbf{P}_{xx} & \mathbf{P}_{xy} \\ \mathbf{P}_{yx} & \mathbf{P}_{yy} \end{bmatrix} \begin{bmatrix} \mathbf{E}_x \\ \mathbf{E}_y \end{bmatrix} = \beta^2 \begin{bmatrix} \mathbf{E}_x \\ \mathbf{E}_y \end{bmatrix} \quad (5.17)$$

$\mathbf{P}_{xx}$ ,  $\mathbf{P}_{xy}$ , ... include the elements from 5.15 and 5.16. After solving the eigenvalue problem with one of the known methods, we obtain the mode fields and effective indices  $n_{\text{eff}} = \frac{\beta}{k_0}$ , where  $k_0 = \frac{2\pi}{\lambda}$  is the vacuum wavenumber. An equivalent problem formulation with transverse magnetic components is also possible.

## 5.2.2 Finite-Difference Time-Domain

Finite-Difference Time-Domain (FDTD) is a simple yet powerful state-of-the-art method for solving Maxwell's equations in the time domain for complex 3D geometries and arbitrary materials.

### 5.2.2.1 Basic Algorithm

The original algorithm proposed by Yee in 1966 [63] employs second-order central difference approximations of spatial and temporal derivatives of Maxwell's curl equations. It can be summarized as a sequence of the following steps [66]:

1. Replace derivatives in Maxwell's equations with finite differences and discretize time and space.
2. Obtain the update equations that determine the future field values from the known, past fields.
3. Evaluate the magnetic field one time-step in the future.
4. Evaluate the electric field one time-step in the future.

5. Repeat previous two steps until the desired time is reached.

The discretization is similar to the one used in FDE (see Section 5.2.1), but now we do not assume a  $\propto e^{i(\beta z - \omega t)}$  field dependence. Eqs. 5.13 and 5.14 therefore take a more general form [67]:

$$i\omega\mu_0 H_x = \frac{\partial E_z}{\partial y} - i\beta E_y \longrightarrow \mu \frac{\partial H_x}{\partial t} = \frac{\partial E_y}{\partial z} - \frac{\partial E_z}{\partial y} \quad (5.18a)$$

⋮

$$-i\omega\varepsilon_0\varepsilon_r E_z = \frac{\partial H_y}{\partial x} - \frac{\partial H_x}{\partial y} \longrightarrow \varepsilon \frac{\partial E_z}{\partial t} = \frac{\partial H_y}{\partial x} - \frac{\partial H_x}{\partial y} \quad (5.18b)$$

The discretization is done over a 3D Yee mesh, composed of overlapping primary and secondary cells, see Fig. 5.5b. Temporal and spatial derivatives are replaced by their discrete counterparts, e.g. Eq. 5.18a is transformed into

$$\mu \left( \frac{H_{x,i,j+\frac{1}{2},k+\frac{1}{2}}^{n+1} - H_{x,i,j+\frac{1}{2},k+\frac{1}{2}}^n}{\Delta t} \right) = \left( \frac{E_{y,i,j+\frac{1}{2},k+1}^{n+\frac{1}{2}} - E_{y,i,j+\frac{1}{2},k}^{n+\frac{1}{2}}}{\Delta z} \right) - \left( \frac{E_{z,i,j+1,k+\frac{1}{2}}^{n+\frac{1}{2}} - E_{z,i,j,k+\frac{1}{2}}^{n+\frac{1}{2}}}{\Delta y} \right) \quad (5.19)$$

Here,  $n$  is the  $n^{\text{th}}$  time-step,  $x, y, z$  denote the field components,  $i, j, k$  are the spatial coordinates and  $\Delta t, \Delta z, \Delta y$  the time and spatial steps. After discretizing all the Eqs. from 5.18, we rearrange them to obtain the update equations, suitable for a time-stepping scheme. For example, Eq. 5.19 is rewritten to

$$H_{x,i,j+\frac{1}{2},k+\frac{1}{2}}^{n+1} = H_{x,i,j+\frac{1}{2},k+\frac{1}{2}}^n + \frac{\Delta t}{\mu} \left[ \left( \frac{E_{y,i,j+\frac{1}{2},k+1}^{n+\frac{1}{2}} - E_{y,i,j+\frac{1}{2},k}^{n+\frac{1}{2}}}{\Delta z} \right) - \left( \frac{E_{z,i,j+1,k+\frac{1}{2}}^{n+\frac{1}{2}} - E_{z,i,j,k+\frac{1}{2}}^{n+\frac{1}{2}}}{\Delta y} \right) \right] \quad (5.20)$$

We assume that  $E_y^{n+\frac{1}{2}}, E_z^{n+\frac{1}{2}}$  and  $H_x^n$  are known, as the magnetic and electric fields are updated alternatively, in "half-steps" -  $H^{n+1}$  is determined by using  $E^{n+\frac{1}{2}}$  values which were obtained from  $H^n$ , all the way down to  $n = 0$  and initial field values, which are known (initial conditions). This recursive update scheme is also known as the *leapfrog* time-update algorithm.

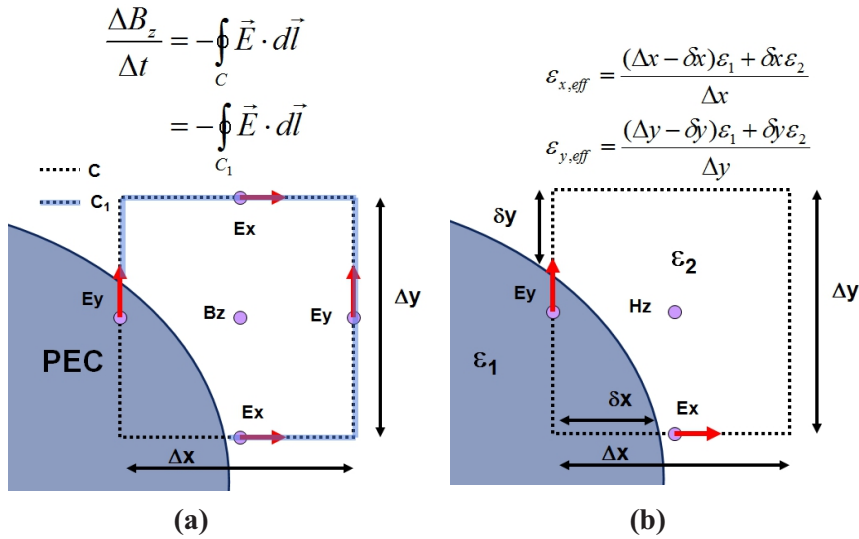


**Figure 5.6:** (a) A perfect electrical conductor is accounted for by reducing the contour integral, including only the region outside. (b) In case of dielectric interfaces, each component in the cell is given an effective permittivity, scaled by its ratio within the cell. Figures taken from [68].

### 5.2.2.2 FDTD with Lumerical

The scheme presented in the previous section is valid for electromagnetic fields in linear, isotropic, lossless media. Modern simulation packages, such as Lumerical FDTD Solutions, build on top of the original algorithm by implementing several sophisticated techniques to model arbitrary materials and improve the simulations in terms of accuracy and computation time.

One obvious improvement is using a non-uniform mesh, which can be refined where necessary, e.g. in high index or highly absorbing materials. The Cartesian mesh still has its drawbacks, as the inability to account for variations within a single Yee cell results in a staircase permittivity mesh. Lumerical mitigates this weakness by using *Conformal Mesh Technology* (CMT) to account for sub-cell features [68]. The general approach of conformal mesh methods is to solve Maxwell's equations at interfaces of different structures in the integral form. For example, Yu-Mitra methods are useful when modeling curved perfect electric conductor (PEC) or dielectric surfaces, see Fig. 5.6. Lumerical's CMT is an

extension of such methods, providing a greater accuracy for a coarse mesh to reduce simulation times by a factor of around 10, and achieving a faster and smoother convergence.

As FDTD is a time-domain method, a single simulation can provide broadband results. However, this is only an advantage if we can accurately model materials over a broad frequency range. In contrast to conventional dispersion models, such as Drude, Debye or Lorentz, Lumerical introduced multi-coefficient materials (MCMs), offering a better fit to dispersion characteristics of real materials, which are often hard to describe with the aforementioned models [69]. The simulation environment already comes with a material database including experimental values of common materials used in photonics. A fit is automatically generated, and for a better agreement several parameters can be tweaked. Users can also import their own measured values or use one of the other possible material types, such as a simple (n,k) material, a PEC or providing an analytical expression [70].

### **The Use of FEM, FDE and FDTD**

Each of the numerical methods presented in this Chapter has its own strengths and weaknesses. The main advantage of FEM with respect to Finite Differences Methods is its adaptable mesh. In the thesis, FEM is employed in solving the eigenmode problem and determining the effective refractive indices  $n_{\text{eff}}$ , as it provides a greater accuracy at a comparable number of mesh elements with respect to FDE. The latter is also used for eigenmode analyses, to validate the FEM results and to determine the mode field profiles. These can then be directly imported as a source in the 3D FDTD simulations, which compute the time evolution of the propagating fields and can thus be used to extract parameters like reflectivity or coupling efficiency.



# Chapter 6

## Simulation Results

After we reviewed the basics of lasers, waveguide modes, chiral optics and the numerical methods employed by the utilized simulation tools, we can finally set up the simulations to study our NW structures of interest prior to fabrication.

In the following sections, initial simulations of a standalone NW show the dependence of supported modes on the NW radius. The reflectivity of the end facet is computed at different NW radii and several structures on top of the end facet are evaluated. In subsequent simulations of a NW on WG structure, we study unidirectional coupling into the WG and investigate the influence of several parameters, such as the NW and WG dimensions and the oxide thickness.

### 6.1 GaAs-AlGaAs Core-Shell NW Laser

#### 6.1.1 Structure

The basic simulated structure is the GaAs-AlGaAs core-shell NW, consisting of a GaAs core (active region), followed by a 5 nm thick AlGaAs passivation layer and protected by a 5 nm thick GaAs cap. The cross-section is a hexagon, as that is the natural shape of the fabricated NWs which is connected to the crystal

structure<sup>1</sup>. We are interested in the supported modes and end facet reflectivities under different conditions. The used parameters that are mostly fixed are listed in Table 6.1. The structure is illustrated again in Fig. 6.1 with the radius of the NW marked red as the only variable parameter.

Name	Symbol	Value	Unit
Temperature	$T$	300	K
Wavelength	$\lambda$	870	nm
Refractive Index GaAs	$n + ik$	3.627+i0.0216	-
Refractive Index AlGaAs	$n + ik$	3.48	-
AlGaAs Thickness	$d_{\text{pass}}$	5	nm
GaAs Cap Thickness	$d_{\text{cap}}$	5	nm
NW Length	$l_{\text{NW}}$	5	$\mu\text{m}$

**Table 6.1:** Simulation constants

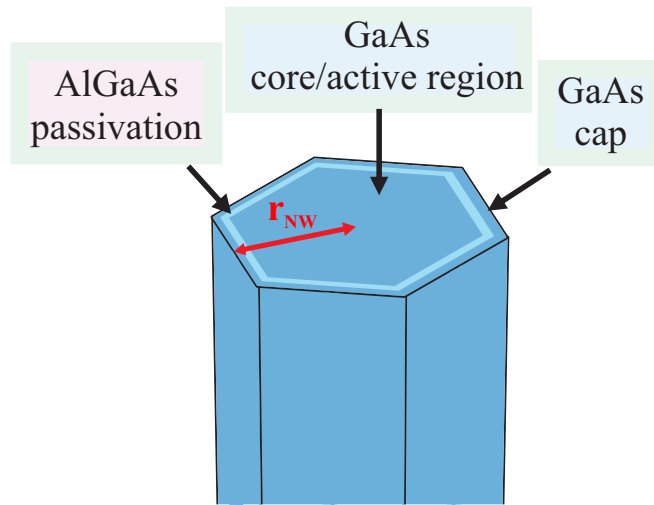


**Figure 6.1:** The basic GaAs-AlGaAs core-shell NW simulation structure. The thickness of the passivation and cap layer remain constant at 5 nm, while we sweep the NW radius (marked in red) by changing the active region thickness. We define the NW radius as the distance between the NW center and side facet.

<sup>1</sup> A more detailed explanation of the NW properties and the fabrication process can be found in [25]

### 6.1.2 Mode Analysis

We are first interested in the modes supported by the NW waveguide with respect to a change of the NW radius. We expect to observe cut-off, when a certain mode reaches a point where it no longer can propagate inside the waveguide. The obtained results are the mode field profiles and effective refractive indices at different radii. This analysis is crucial to understand how the modes of interest change with the NW radius. It can also be useful in the context of identifying the interesting range of NW radii, e.g. to find the radius for which we get single-mode waveguiding. The results are obtained by solving the eigenmode problems across the NW cross-section. We can use either Lumerical MODE Solutions or COMSOL Multiphysics, as discussed in Chapter 5. The former is used to determine the mode profiles which can be used directly as an injected light source in FDTD simulations, while the latter provides greater accuracy at a given number of degrees of freedom as it uses an adaptive non-uniform triangular mesh and was thus utilized in the mode analysis.

The mode field profiles were already shown in Section 3.3 for the case of a NW with radius 200 nm. Now, the influence of the NW size is investigated by varying its radius from 50 to 300 nm and tracing the  $n_{\text{eff}}$  of some of the supported modes, as shown in Fig. 6.2. The obtained values lie between the refractive indices of the NW material (bulk GaAs) and the surrounding environment (air). At larger NW radii, the  $n_{\text{eff}}$  values of the different modes increase. If we would increase the NW radius even further, the effective indices of individual modes would slowly stabilize at a value just below  $n_{\text{GaAs}}$ . At smaller radii, the fraction of the power propagating inside the waveguide for an individual mode is decreased (the mode "spreads out" and part of the field intensity is on the outside of the NW). This happens as the respective mode approaches its cut-off point and the  $n_{\text{eff}}$  experiences a steep decrease. Once the  $n_{\text{eff}}$  value drops below the refractive index of the ambient material (in our case air,  $n_{\text{air}} = 1$ ), the mode is no longer supported in the nanowire. This region is covered in red color in Fig. 6.2. The

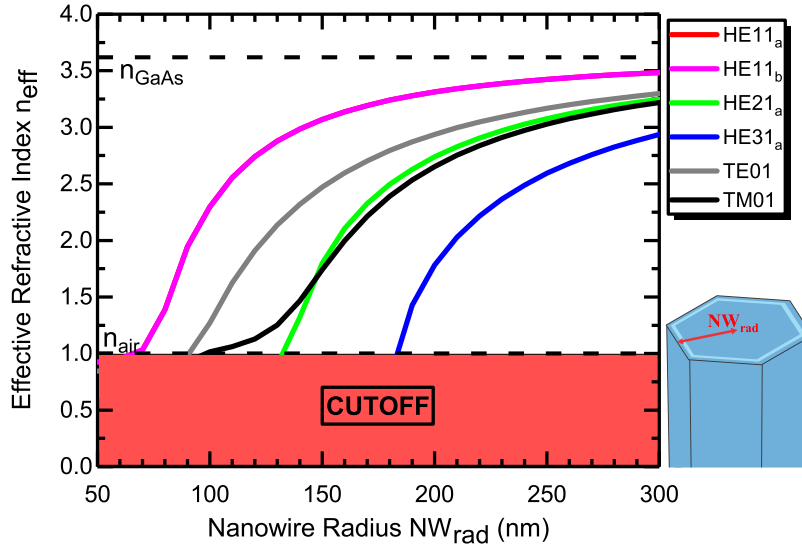


**Figure 6.2:** The  $n_{\text{eff}}$  dependency on NW radius for several modes. The dashed lines mark the refractive indices of the NW material (bulk GaAs,  $n = 3.627$  at room temp.) and the surrounding environment (air,  $n=1$ ). The red area below marks the cut-off region - as an individual mode reaches this zone at decreasing radius, it is no longer supported by the NW.

cut-off point appears at different NW radii for different mode types. This is, however, not the case for degenerated modes. As we explained in Section 3.3, the hexagonal symmetry of the nanowire gives rise to degenerated  $a$  and  $b$  modes. They share the radial and azimuthal symmetry properties, but are rotated around the  $z$  axis by a  $90^\circ$  geometrical angle (see also Fig. 3.4 and Fig. 3.5). For lower order modes, such as HE11<sub>a</sub>/HE11<sub>b</sub> and HE21<sub>a</sub>/HE21<sub>b</sub>, these  $a$  and  $b$  degenerated modes are essentially the same mode, rotated by  $90^\circ$ . As a consequence, they also share the same  $n_{\text{eff}}$  values and dependency on NW radius. This can be seen in Fig. 6.2, where the  $n_{\text{eff}}$  of the HE11<sub>a</sub> and HE11<sub>b</sub> modes show an overlap. In higher order modes, e.g. HE31<sub>a</sub>/HE31<sub>b</sub>, the  $n_{\text{eff}}$  of the  $a$  and  $b$  modes differ slightly, as there is a larger difference between the field ratio propagating inside the NW body for these modes (see Fig. 3.5).

### 6.1.3 End Facet Reflectivity

Next, we study the reflectivity of the NW end facet. We define it as a power ratio between the reflected and incident light propagating in the observed mode of the investigated structure,  $\frac{P_{\text{refl}}}{P_{\text{inc}}}\Big|_{\text{NW mode}}$ . In the simulated structures in later sections, the NW is standing vertically on a waveguide while the upper end facet is facing air. Here, we first investigate the influence of the NW radius and different end facet configurations on the reflectivity of the upper facet by using Lumerical FDTD Solutions. Designing a structure with a high reflectivity is one of the crucial factors in achieving low-threshold lasing (see also Eq. 2.4). This ensures a low power consumption, which is an important metric for integrated devices.

When simulating 3D NW structures, we select one of the supported modes (determined by performing an FDE simulation in the cross-section of the NW) to inject a so-called *mode source* inside the NW. The injected light in the form of a broadband pulse then propagates along the NW axis. We can investigate arbitrary regions of the simulation domain by placing different *monitors*. Mode expansion monitors use overlap analysis to determine the forward/backward propagating fields in terms of a linear combination of individual supported modes, as they form a complete basis set [71]. Frequency-domain field monitors are helpful in determining the electromagnetic field profiles and transmitted/reflected power over a cross-section at a chosen location. The end facet reflectivity can be determined by placing such a monitor behind the injected source and recording the field passing through its surface. We norm the integrated power to the injected power to get the amount of light, back-reflected from the end facet and hence determine the reflectivity. When dealing with lossy media (imaginary part in the refractive index), we also need to account for absorption as the light propagates along the NW. To obtain the correct value of end facet reflectivity, we renorm the recorded value in terms of back-propagating the wave, i.e., by using the relation describing power ratios in an absorbing material

$$P(z) = P(z_0)e^{-\alpha z}, \quad (6.1)$$

where the absorption coefficient  $\alpha$  can be obtained from  $k$ , the imaginary part of the effective refractive index of the propagating mode:

$$\alpha = \frac{4\pi k}{\lambda} \quad (6.2)$$

### Air Facet

We start with the simplest case of observing the reflectivity for a flat top facet with no additional layers. In the previous subsection we have shown that the mode profiles and their effective refractive indices  $n_{\text{eff}}$  depend on the NW radius. As we also expect the reflectivity values to be dependent on the NW dimensions, we compute the reflectivity for a range of NW radii as well.

The simulation results of the reflectivity dependency on NW radius is visualised in Fig. 6.3. The cut-off points (NW radii) for individual modes were obtained from the mode analysis study (see Fig. 6.2) and are marked here with dashed lines. The reflectivity of individual modes reduces drastically near their respective cut-off point, as the mode is no longer guided in the NW. At large NW radii, the reflectivities do not change significantly. For the HE11, HE21 and HE31 modes, we observe peaks near the cut-off region, which may seem unexpected. However, by increasing the NW radius, higher order modes start appearing. After reflection, light is partly scattered also into some of these modes, mostly into those with a similar radial and azimuthal symmetry. For example, the HE11 mode scatters partially also into the EH11 mode, hence reducing the reflectivity in the observed mode. For degenerate HE11<sub>a</sub> and HE11<sub>b</sub> modes, we see an almost identical reflectivity dependence. This is again due to the fact that for lower order modes, the  $a$  and  $b$  modes are essentially the same mode, rotated by 90°.

We have shown that for the case of degenerated modes, the mode field profiles,  $n_{\text{eff}}$  and reflectivities are very similar - in subsequent results we omit the  $a$  and  $b$  indices and work with  $a$  modes unless stated otherwise.

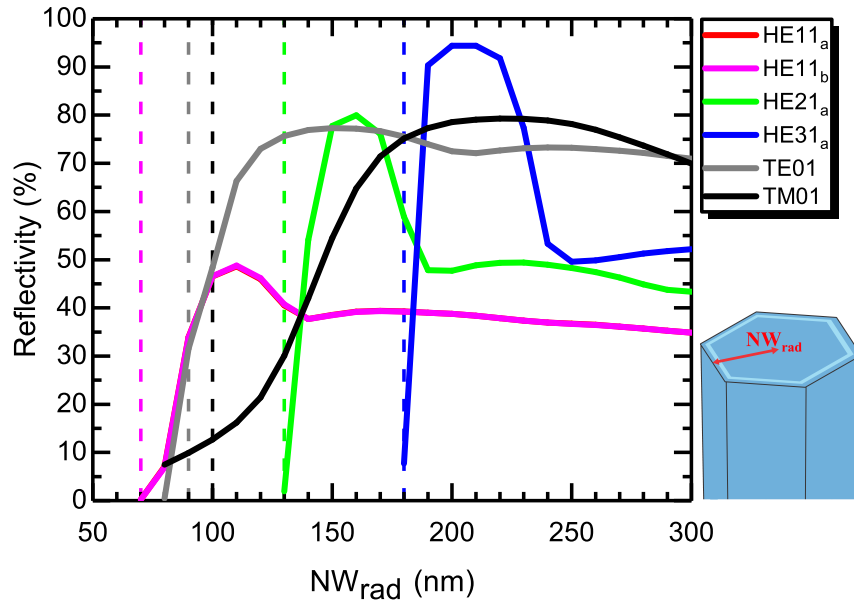


**Figure 6.3:** The reflectivity dependency on NW radius for some of the supported modes.

### Gold Mirror

To enhance the top facet reflectivity, we can add a structure acting as a mirror on top of the end facet. A simple idea is the addition of a metal layer which should provide a better reflection than the plain end facet. The modified structure is illustrated in Fig. 6.4.

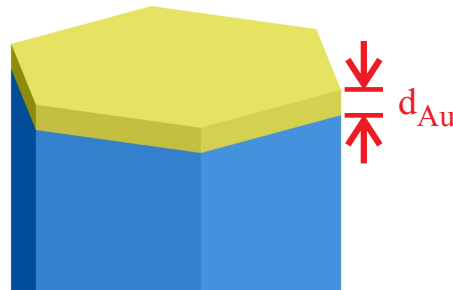


**Figure 6.4:** The addition of a gold layer on top of the NW end facet in an attempt to improve the reflectivity. The gold layer thickness is varied to find a possible optimum end facet reflectivity.

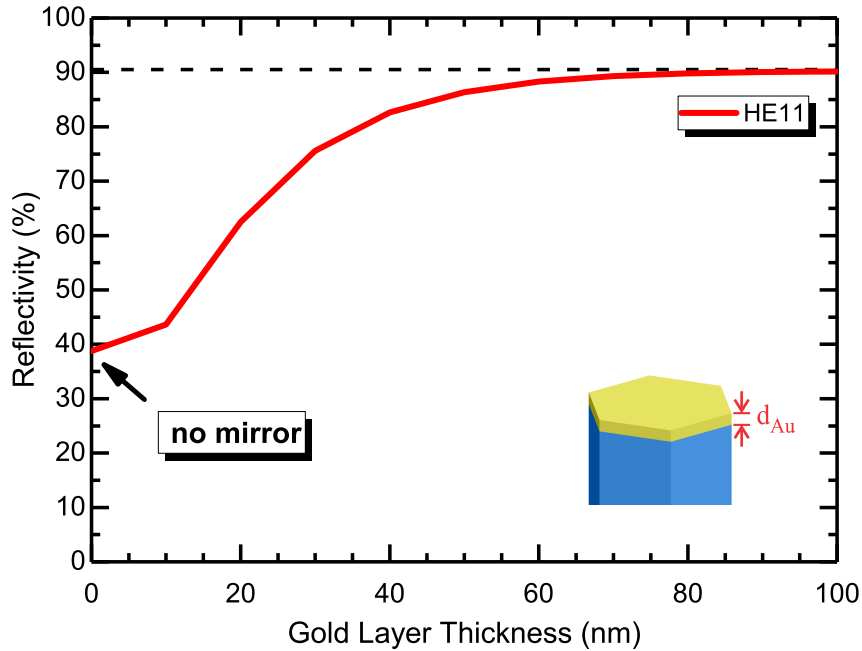


**Figure 6.5:** The end facet reflectivity of a gold covered nanowire end facet propagating the fundamental HE11 mode. With increasing Au layer thickness a saturation in the reflectivity is observed. The reflectivity can be increased from around 40% up to 90%.

We study the case for a gold layer of variable thickness on top of a 200 nm radius NW for the fundamental HE11 mode. The results are presented in Fig. 6.5. The reflectivity first increases with the gold mirror thickness increase and saturates for large thicknesses (at around 60 nm and more). There is a simple reasoning behind - when the metal layer is too thin, some of the light can still make it to the other side of the end facet/metal/air interface and radiate in the environment. This is illustrated in Fig. 6.6 with FDTD simulation snapshots of the electric field amplitude  $|\mathbf{E}|$  at the moment of reflection for different metal layer thicknesses. In (a) and (b) we see that without a mirror or with a 30 nm thick metal layer, some of the light propagates beyond the end facet and radiates in the environment. In (c), a 60 nm thick metal layer is enough to reflect the light completely, but we still only get a reflectivity of around 90%. Some of the remaining 10% is lost through absorption in the metal layer during reflection, and

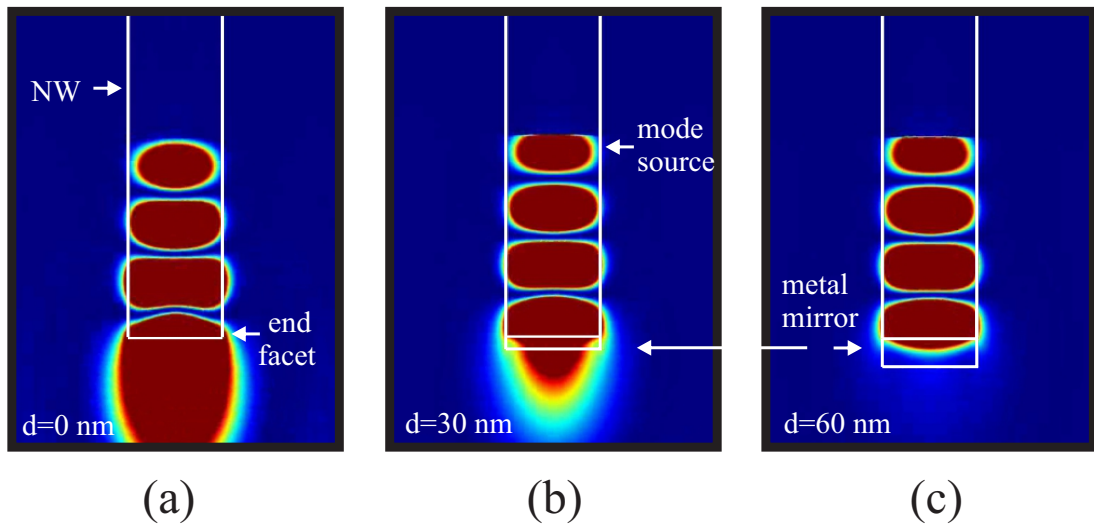


**Figure 6.6:** Snapshot of the fundamental HE11 electric field intensity profile at a  $xz$  cut through the NW at the reflection moment for three different cases: (a) no metal layer, (b) 30 nm thick and (c) 60 nm thick gold layer.

a small portion of the reflected light is scattered into higher order modes.

### Gold and Dielectric Layer Stack

Sometimes, an oxide layer is required between the metal and the nanowire (e.g., as an insulating layer in case of metal contacting). We therefore consider the case of a  $\text{SiO}_2$  oxide/gold layer stack, placed on top of the NW end facet, see Fig. 6.7.

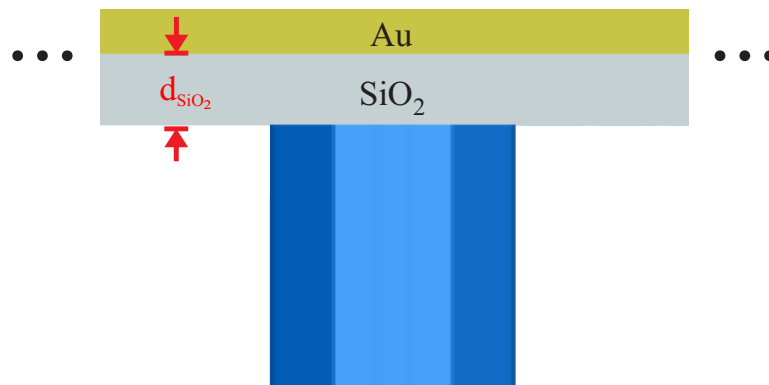


**Figure 6.7:** An oxide layer is required for the NW growth procedure in some cases. Here, an oxide/gold layer stack is placed on top of the NW end facet. The thickness of the oxide layer is varied in the simulation.

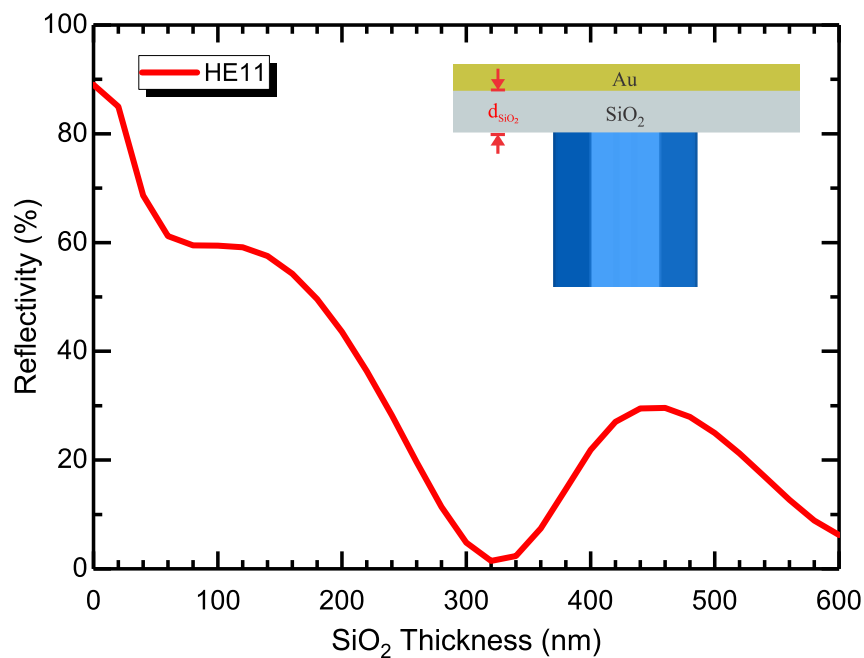


**Figure 6.8:** The reflectivity dependence on the SiO<sub>2</sub> layer thickness. The dielectric layer is sandwiched between the NW end facet and a gold layer. The general trend of reduced reflectivity with increased dielectric layer thickness is accompanied by local extrema due to interference effects.

In our reflectivity study, we vary the thickness of the SiO<sub>2</sub> layer. The gold layer thickness is set to 80 nm, well in the region where the mirror reflectivity already saturates (see also Fig. 6.5). As can be seen in the simulation results Fig. 6.8, the reflectivity has the largest value when the NW is placed directly on top of the gold mirror, i.e., without an oxide layer. After introducing an oxide layer and increasing its thickness, the reflectivity follows a descending trend, which can be associated with a part of the light propagating away and decaying at the SiO<sub>2</sub>/air interface. The reflectivity also experiences local maxima and minima at larger thicknesses. With two different layers beneath the NW end facet, light is now reflected at two regions - at the NW end facet/oxide interface and the oxide/metal interface. The back reflected light is a sum of those waves. The local maxima and minima can be explained by constructive and destructive interference. In order to get a constructive interference, the waves reflected off both interfaces

need to be in phase, also known as the *phase matching condition*. By varying the SiO<sub>2</sub> layer thickness we change the optical path length of the wave reflected from the SiO<sub>2</sub>/Au interface. For constructive interference, the path length  $l$  needs to satisfy the condition:  $l = u\lambda$ , where  $u \in \mathbb{N}$  and  $\lambda = \lambda_0/n_{\text{SiO}_2}$ ,  $n_{\text{SiO}_2} = 1.45$ . In our case,  $l = 2d_{\text{SiO}_2}$ . The distance between a minimum and a maximum  $\frac{\Delta}{2}$  would then equal  $\frac{\Delta}{2} = \frac{\lambda_0}{4n_{\text{SiO}_2}} \simeq 140$  nm. In Fig. 6.8 we can recognize a local minimum at around 320 nm and a local maximum at around 460 nm SiO<sub>2</sub> thickness, which is a thickness difference of 140 nm.

## 6.2 Nanowire on a Si Ridge Waveguide

We continue with a more complex structure consisting of a nanowire positioned vertically on top of a Si waveguide. While the coupling of light from the NW to the waveguide has been investigated and successfully demonstrated in our group [29], we use this scheme to exploit chiral effects and elucidate unidirectional coupling of light into the waveguide.

### 6.2.1 Structure

The structure of the NW remains unchanged from the previous studies, but now it is positioned vertically on a Si waveguide on top of a Silicon-On-Insulator (SOI) platform. The NW dimensions remain the same as in Table 6.1, while we use material values for a temperature of 10K to make the results more comparable to the lab environment (this temperature is used in measurements, as lasing is achieved more easily). The values are in Table 6.2.

The Si waveguide is covered by another SiO<sub>2</sub> layer, which plays a dual role:

- it enables a site-selective integration of NWs on top of the Si waveguide and
- increases the modal reflection at the waveguide interface by providing a higher index contrast than the minuscule refractive index difference of GaAs and Si.

Name	Symbol	Value	Unit
Temperature	$T$	10	K
Wavelength	$\lambda$	820	nm
Refractive Index GaAs	$n + ik$	3.25	-
Refractive Index AlGaAs	$n + ik$	3.17	-
Refractive Index Si	$n + ik$	3.634+i0.003	-
Refractive Index SiO <sub>2</sub>	$n + ik$	1.452	-
Subst. Thick. SiO <sub>2</sub>	$d_{\text{sub, SiO}_2}$	1	$\mu\text{m}$

**Table 6.2:** Additional simulation constants

In our simulations we investigate the influence of several parameters: the dimensions of the NW, waveguide and top oxide, the position of the NW on the waveguide and the shape and polarization of the propagating fields. The simulated structure is illustrated in Fig. 6.9.

## Unidirectional Coupling with NWs

In the example in Section 4.5 we showed that unidirectional coupling to Si waveguides can be easily accomplished by placing a circularly (or, more generally, elliptically) polarized dipole source in the appropriate position. To achieve a comparable effect with a NW on top of a waveguide, we need to fulfill the following criteria:

- Have a circularly/elliptically polarized wave propagating along the NW
- Use a waveguide of appropriate, i.e., sub-wavelength dimensions with evanescent field regions
- Place the NW in an optimal position to achieve good unidirectional coupling

## Circular Polarization in NWs

As we have discussed in the Chapter 3, the NW supports several optical modes. By itself, one of these NW modes cannot be simply utilized for the excitation of waveguide modes via spin-orbit coupling, as it does not carry any spin angular

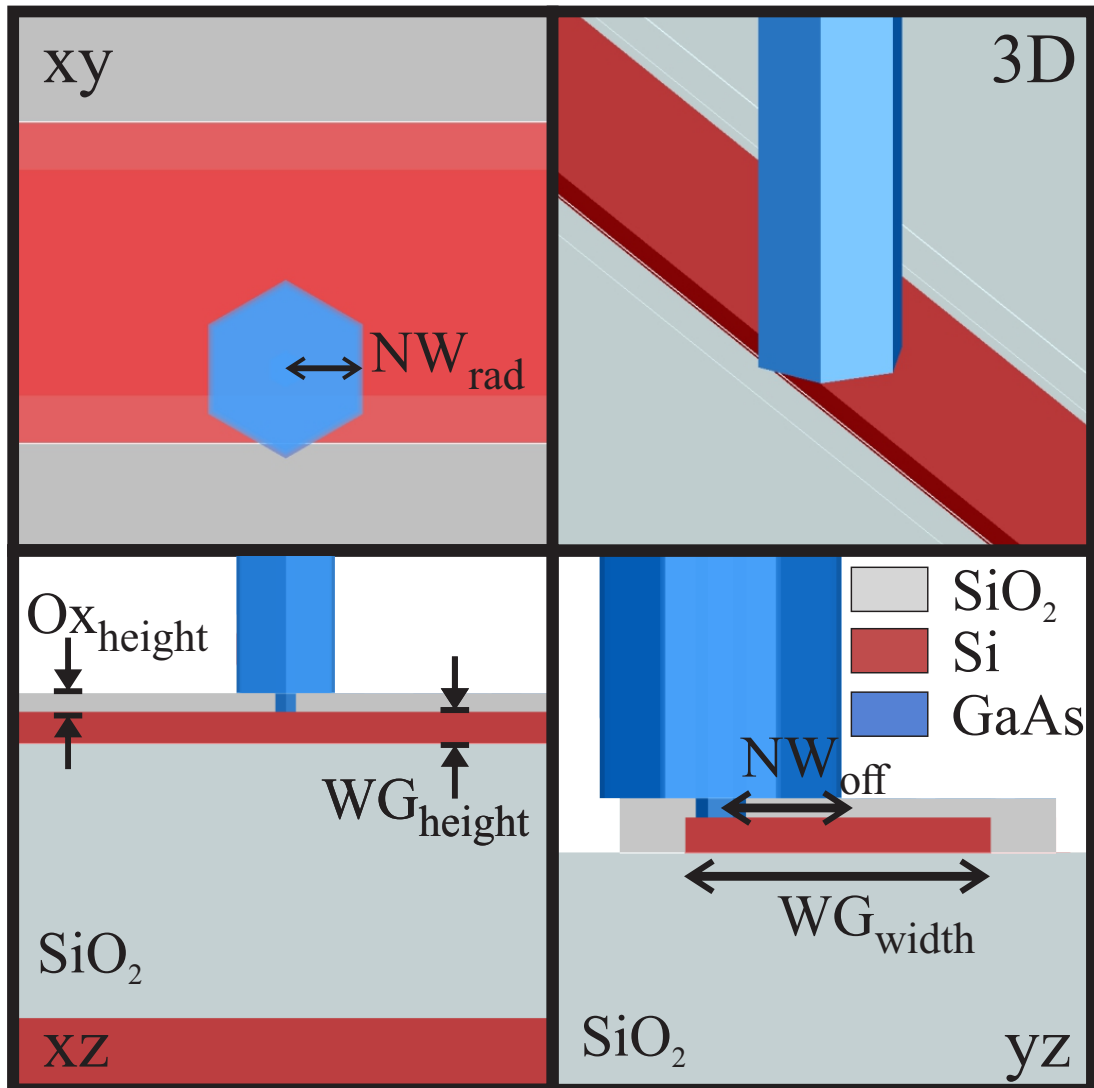


**Figure 6.9:** The simulated structure, a GaAs-AlGaAs core-shell NW laser integrated on a Si waveguide on a Silicon-On-Insulator (SOI) platform. The  $xz$ -view (bottom left) shows the cross section of the structure. The substrate is made from a silicon and a  $\text{SiO}_2$  layer. On top, a silicon waveguide is positioned. Another  $\text{SiO}_2$  oxide layer on top of the waveguide enables site-selective growth by etching holes in the oxide, where the NW core starts its growth. Its second role is to provide improved reflectivities at the interface between the waveguide and NW facilitated by the high index contrast between  $\text{SiO}_2$  and GaAs.  $xy$  and  $yz$  views illustrate a possible asymmetric positioning of the NW on the waveguide. A 3D perspective is also shown (the top oxide is transparent for better visibility of the waveguide). The geometrical parameters that are varied in the simulations are marked:  $\text{NW}_{\text{rad}}$  - NW radius,  $\text{Ox}_{\text{height}}$  - top oxide height,  $\text{WG}_{\text{height}}$  - Si waveguide height,  $\text{WG}_{\text{width}}$  - waveguide width,  $\text{NW}_{\text{off}}$  - NW off-center position.

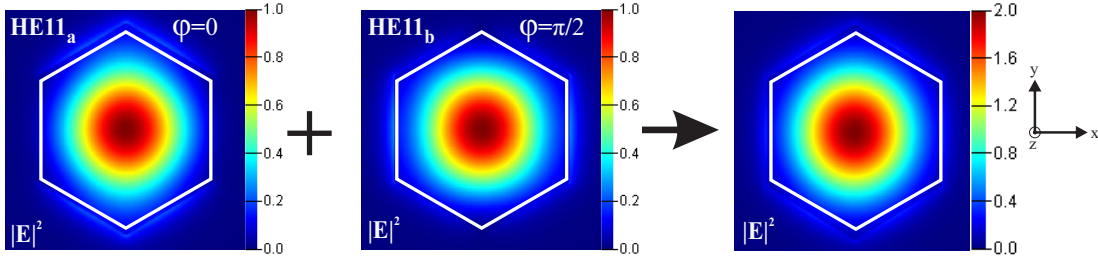


**Figure 6.10:** Electric field intensity profiles  $|\mathbf{E}|^2$  of the HE11a,  $\pi/2$  phase shifted HE11b mode and their sum. For the case of HE11 modes, the result of mode mixing is more evident when observing individual field components, e.g.  $E_z$  in Fig. 6.11.

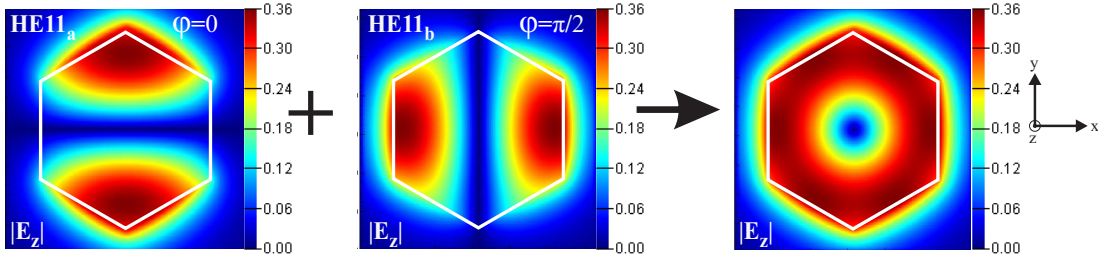


**Figure 6.11:** Profiles of the absolute value of the electric field  $z$  component  $|E_z|$  of the HE11a,  $\pi/2$  phase shifted HE11b mode and their sum.

momentum (SAM). This is a property of circularly/elliptically polarized waves. However, one can construct a circularly polarized wave by mixing two modes. In the following we show that due to the NW geometry, one can obtain pairs of degenerate modes, e.g. HE11<sub>a</sub> and HE11<sub>b</sub>, which have a similar field intensity profile shifted by a  $90^\circ$  angle around the NW axis. A combination of two such modes with a phase shift of  $\pi/2$  gives us a circularly polarized wave, as illustrated in Figs. 6.10 and 6.11. This way we get a SAM vector component along the NW axis ( $S_z$ ), see Fig. 6.12a. In contrast to an ideal point source, the SAM also has  $S_x$  and  $S_y$  components, which are generally smaller than the desired  $S_z$  component. However, near the edges of the NW where  $S_z$  decreases, the other two components become comparable. As a consequence, the SAM vector  $\mathbf{S} = [S_x, S_y, S_z]^T$  points in a different direction, see Figs. 6.12 (b,c).

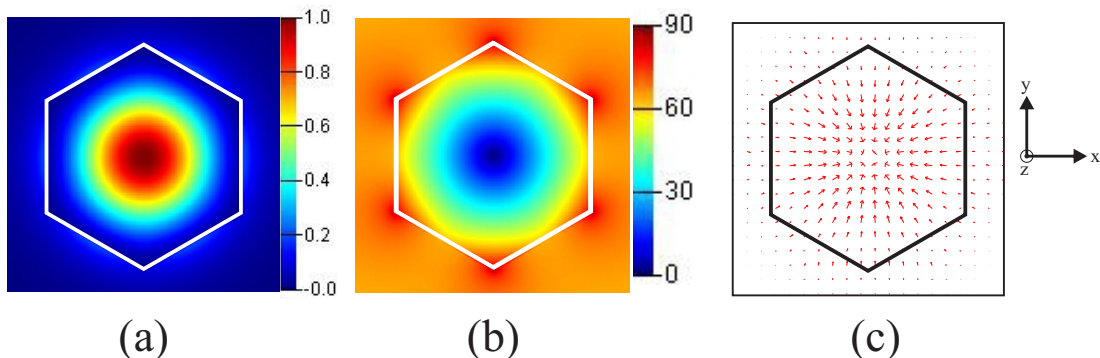


**Figure 6.12:** (a) The  $S_z$  SAM component of the HE11a and  $\pi/2$  phase shifted HE11b combination, normalized to 1.  $S_z$  has a maximum absolute value in the center of the NW and decreases towards the edges. (b) The angle between the  $z$  axis and the SAM vector  $\mathbf{S} = [S_x, S_y, S_z]^T$ . Only in the center  $\mathbf{S}$  points along the NW axis. (c) The  $\mathbf{S}$  vector, projected on the  $xy$  plane. In the off-center locations, it points slightly towards the center of the NW axis.

### Waveguide Eigenmode Analysis

Next, we perform an eigenmode analysis of the waveguide to study the field profiles and ratios between individual components. We follow a similar procedure as the one described in the Si waveguide example. Eigenmode solutions, i.e., the electric field components of the fundamental mode for an exemplary case of a Si waveguide with dimensions  $280 \text{ nm} \times 70 \text{ nm}$  are shown in Fig. 6.13. We can then map the ratio between individual field components, e.g.,  $\text{Im}(E_x)/\text{Re}(E_y)$  in Fig. 6.14, to identify the positions where the placement of a NW supporting circularly polarized waves should result in a unidirectional excitation.

### Finding the optimal parameters

In this configuration, we are mainly interested in optimizing the following properties of our structure:

- A large unidirectionality, so that light couples mostly into one direction
- A significant amount of light coupling into one of the directions (a high directionality would hardly be useful if only a negligible fraction of light intensity is coupled into the waveguide)

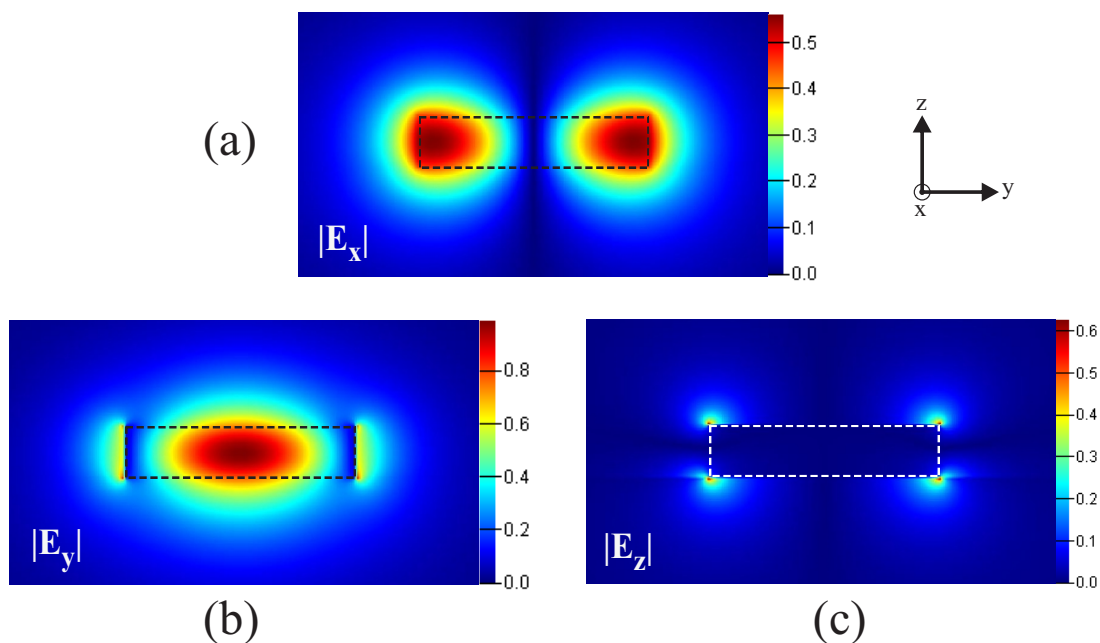


**Figure 6.13:** The electric field components of the fundamental mode in a simple Si waveguide with dimensions  $280 \times 70$  nm. The dashed line marks the edges of the waveguide. A strong gradient in the transversal  $|E_y|$  component near the waveguide walls gives rise to a longitudinal  $|E_x|$  component of comparable magnitude. The  $|E_z|$  component is negligible, except for small regions near the waveguide edges.

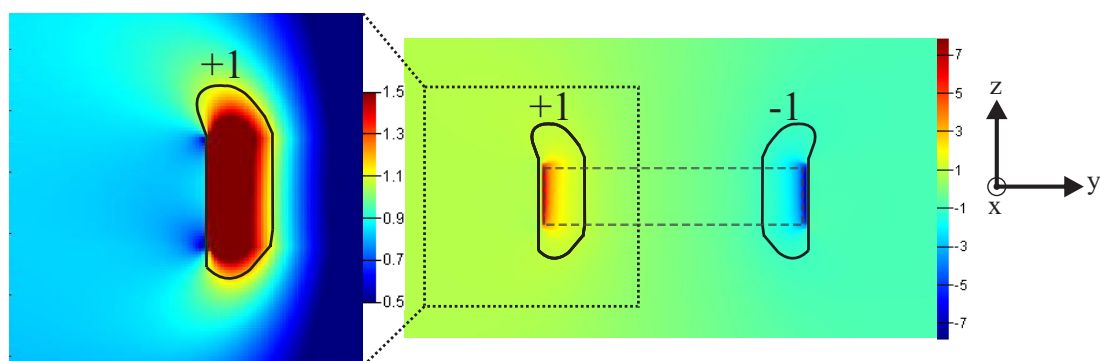


**Figure 6.14:** Map of  $\text{Im}(E_x)/\text{Re}(E_y)$ , the ratio of the imaginary part of the transversal and longitudinal electric field components. Locations where the value is  $\pm 1$  is outlined with a solid line - areas near these locations are interesting in the context of spin-orbit coupling. The left inset shows a narrower region with an adapted color scale to showcase the behaviour of the ratio near the waveguide walls. The waveguide edges are marked with a dashed line.

- A high reflectivity at the NW-WG interface to ensure low-threshold lasing of the NW

In an attempt to approach an optimum, we study the influence of different parameters, as illustrated already in Fig. 6.9. Our goal of finding an optimum structure which exhibits unidirectional coupling can be approached by sweeping through several parameters. This is a challenging task, as the parameter space is very large, which is common for multidimensional optimization problems.

In the following subsections, the simulation results of parameter sweeps are presented and discussed. Our initial test structure is a NW with a radius of 120 nm positioned on a rectangular Si waveguide with a width of 280 nm and a height of 70 nm. The initial dimensions were chosen based on eigenmode analyses. The NW radius is set to be small, near the cut-off of the HE<sub>11</sub> mode, considering that most other studies [51, 57] employed a point-like dipole source. The waveguide dimensions are set to strongly support only its fundamental mode, as our unidirectional coupling efforts are aimed at a single mode excitation. The injected light source is a combination of  $\pi/2$  phase shifted HE<sub>11<sub>a</sub></sub> and HE<sub>11<sub>b</sub></sub> modes to form a circularly polarized propagating wave.

## 6.2.2 Nanowire Position Offset

Based on the examples we discussed in Chapter 4 we expect a strong dependency on the NW position. Therefore we first keep our initial NW and waveguide structure and compute a sweep of the NW offsets from the center position. In the simulations, we are interested in several properties:

- **the unidirectional coupling ratio**  $\frac{P_{\text{pref}}}{P_{\text{supp}}} \Big|_{\text{1st WG mode}}$ , defined as a power ratio between the light coupled to the preferred waveguide direction and light coupled to the suppressed direction, both into the fundamental waveguide mode
- **the coupling efficiency**  $\frac{P_{\text{coup, 1st WG mode}}}{P_{\text{inj, NW}}}$ , i.e., the amount of light coupled into the fundamental waveguide mode, expressed as a fraction of the power

injected from the NW

- **the reflectivity back into the NW**  $\frac{P_{\text{refl}}}{P_{\text{inc}}}\Big|_{\text{NW mode}}$ , defined as a ratio of the reflected and incident light of the observed NW mode (combination) at the nanowire/waveguide interface

When evaluating the coupling ratio and efficiency, we are only considering the fundamental waveguide mode. As explained in Section 6.2.1, the unidirectional coupling conditions are different for each mode. For our initial waveguide structure we chose a geometry where only the fundamental mode can propagate.

In Fig. 6.15(a), the unidirectional coupling ratio at different NW offsets is plotted. For our choice of incident polarization handedness and waveguide side, the preferred coupling direction for light is into the "right" waveguide direction (i.e., in the positive  $x$  direction, see Fig. 6.9). As expected, at a central position, the coupling ratio between the left and right direction equals 1, i.e., an equal amount of light is coupled in opposite directions of the waveguide. By moving the NW position towards the edge of the waveguide, the symmetry is broken and therefore the coupling ratio to the different directions begins to increase. It reaches a peak value of  $\sim 200$  at a 115 nm offset position. In Fig. 6.15(b), the coupling efficiency into the left and right direction are shown separately. In the preferred right direction, the maximum coupling of around 9.5% is reached at an 85 nm offset - at a different position than the ratio maximum. The behaviour of the coupling ratio and its peak position are not dominated by the coupling in the preferred direction, but are mainly influenced by the suppressed coupling to the opposite direction. In the inset displaying the amount of coupled light into the left direction on a logarithmic scale, one can see the inverse shape to the coupling ratio, reaching a minimum at the position of the maximum coupling ratio. To get a better picture of the differences between omni- and unidirectional coupling, we look at the field profiles from different perspectives. Snapshots from FDTD simulations displaying the electric field intensities for the cases of a central NW position and the optimal NW offset are shown in Fig. 6.16(a, b) in the  $yz$ ,  $xy$

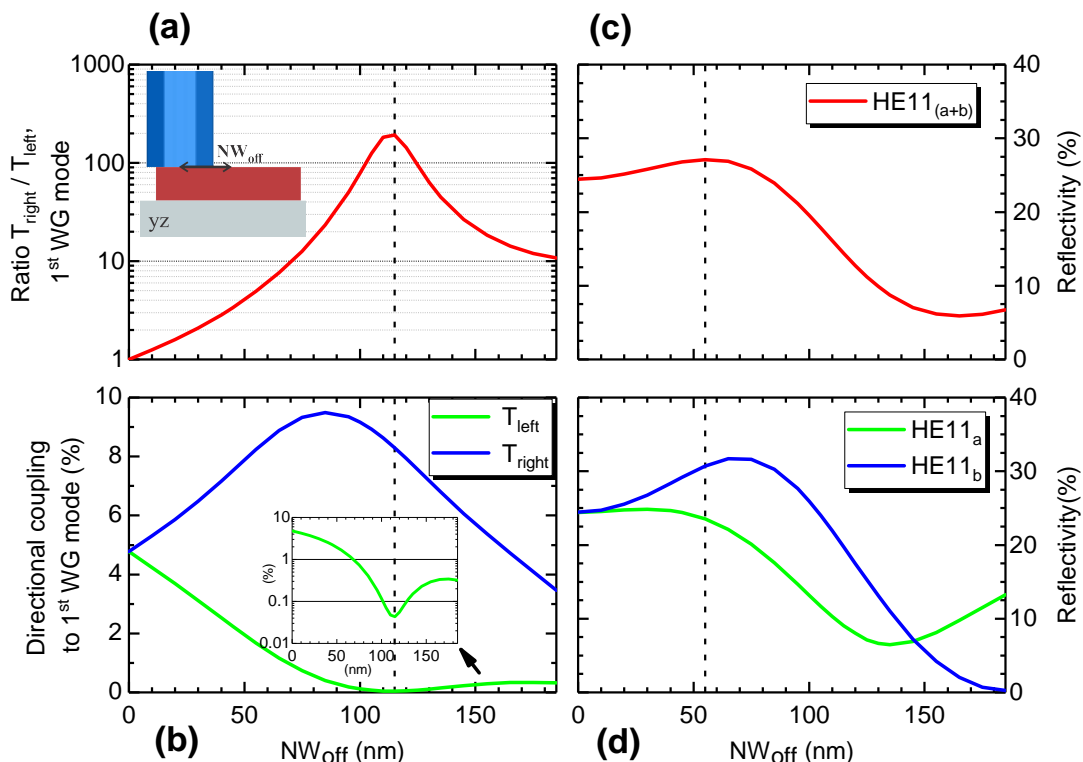


**Figure 6.15:** Simulation results for a sweep of the NW offset from the center position on the waveguide. (a) plots the ratio of the light, coupled in the right versus left direction, reaching a peak value of almost 200. (b) shows the proportion of injected light coupled into the individual direction. The inset displays the coupling into the left direction on a log scale. (c) and (d) plot the reflectivity versus NW offset for the mixed  $HE11_{(a+b)}$  mode and for the individual  $HE11_a$  and  $HE11_b$  contributions.

and  $xz$  plane cuts at consecutive moments in time. The 3D structure with the used plane cuts is illustrated in Fig. 6.16(c). One can see that we get a perfectly symmetric coupling in the case of a central NW position (a), while at an offset, the majority of light couples into the preferred right direction (b).

In Fig. 6.15(c), the reflectivity of the mixed mode  $HE11_{(a+b)}$  is plotted versus offset. Its maximum value of around 27% is reached at a 55 nm offset. Fig. 6.15(d) splits the reflectivity into contributions of the  $HE11_a$  and  $HE11_b$  mode. While the reflectivities of both contributions are equal at the center position, they experience a different dependence on NW offset. As the NW is shifted towards the edge of the waveguide, the latter starts to play a role in the reflec-

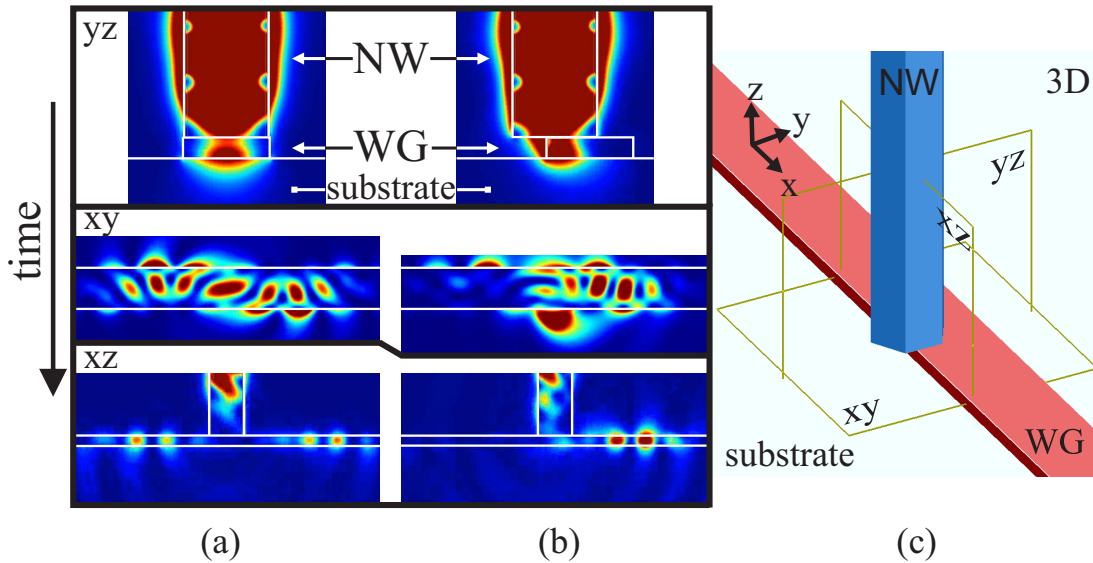


**Figure 6.16:** Snapshots of the electric field intensity for a NW with a radius of 120 nm placed on a  $280 \text{ nm} \times 70 \text{ nm}$  Si waveguide for (a) a central NW position and (b) an offset of 115 nm. From top to bottom, the time frames show the fields in  $yz$ ,  $xy$  and  $xz$  plane cuts at consecutive time moments. The propagation inside the waveguide is symmetric for the central position (left side) and asymmetrical with a strong preference to one direction for the offset case (right side). In (c) is a 3D schematic of the NW on waveguide structure, showing the plane cuts used to produce the snapshots.

tivity of the individual modes. A region of the NW "hangs" over the waveguide edge, so the light propagating along the NW partially faces a nanowire/waveguide interface, while the outside part faces an interface with air, which introduces a greater refractive index contrast. The light reflected back into the nanowire is now a combination of waves reflected from the nanowire/waveguide, waveguide/substrate and nanowire/air interface. We assume that this interplay of interference of several waves induces a difference in the reflectivities of the  $a$  and  $b$  modes. The rotation of the NW starts to play a role in the reflectivity of the  $\text{HE}_{11_a}$  and  $\text{HE}_{11_b}$  mode as well, as the NW's orientation determines the modes' orientation with respect to the waveguide and consequently the ratio of the mode power over the waveguide edge.

The results indicate that the NW offset affects the (unidirectional) coupling into the waveguide significantly. Even a small change in the offset of a few tens

of nanometers can change the directional ratio by orders of magnitude. The other properties of interest, namely the coupling efficiency and the reflectivity, do not show such an extreme sensitivity to the offset position. One must therefore initially aim at an offset with the optimal coupling ratio, as it shouldn't degrade the coupling efficiency and reflectivity significantly. As the coupling ratio is so sensitive to the NW offset, we need to use a range of different offsets when studying the influences of other parameters in the following subsections.

### A Semi-Analytical Coupling Approximation

It is also important to note that the offset where the coupling ratio is highest is not at 95 nm - the position suggested by an eigenmode analysis of the waveguide. As explained in Sec. 4.5, this is the point where the ratio of the longitudinal and transverse electric field components of the fundamental waveguide mode equals one, i.e.,  $\left. \frac{E_x}{E_y} \right|_{WG} = 1$ . In this position, the evanescent electric field of the waveguide is circularly polarized and acquires a transverse spin component, oriented in the  $z$ -direction. This results in the best alignment with the SAM vector of the incident circularly polarized light, which is also oriented in the  $z$ -direction. In the studies completed by most other groups [51, 57], point-like sources were utilized, where the optimal point indeed is the one defined by unity ratio between the transversal and longitudinal field components. However, our NW with a diameter of a few hundred nanometers means that the spin-orbit coupling no longer depends on the spin alignment of the incident light and evanescent waveguide mode at one single point. Instead, it is the result of a collective contribution of overlapping spins over a larger region. We argue that the amount of coupled light is proportional to the product of the transverse spin and the SAM vector and to their enclosing angle. One can test such a dependency with the following procedure:

- Compute the field profiles of the fundamental waveguide mode and of the NW mixed (a+b) mode by solving the eigenmode problem.

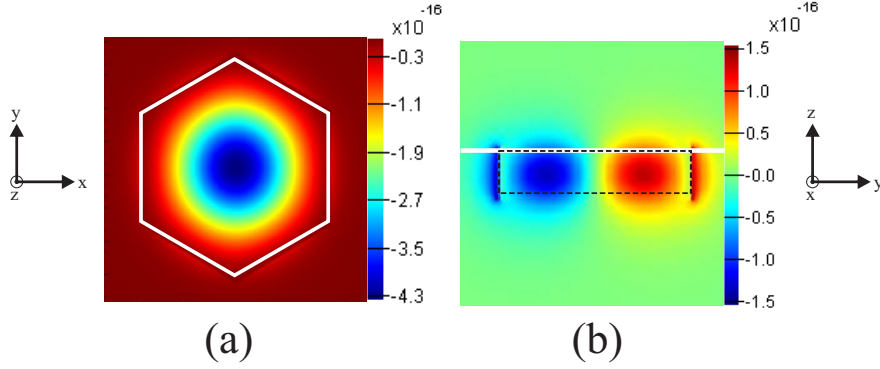


**Figure 6.17:** The  $S_z$  component of the spin vector  $\mathbf{S}$  of (a) the NW in the  $xy$  plane and of (b) the waveguide in the  $yz$  plane. The dotted line marks the edges of the waveguide, while the white line is the region where we calculate the spin overlap between the NW and waveguide in the  $xy$  plane. The waveguide spin map, extended into the  $xy$  plane, is shown in Fig. 6.18.

- Determine the corresponding spin vectors by using the relation

$$\mathbf{S} = -\frac{i\epsilon_0}{2\omega} \mathbf{E}^* \times \mathbf{E} \quad (\text{see also Eq. 4.5}).$$

- Integrate the dot product of spin vectors in the overlapping region

$$\iiint \mathbf{S}_{NW}(x, y, z) \cdot \mathbf{S}_{WG}(x, y, z) dx dy dz.$$

Since we have a discrete mesh, the integral in the final step turns into a sum across all the relevant grid points:

$$\sum_{i=1}^I \sum_{j=1}^J \sum_{k=1}^K \mathbf{S}_{NW}(i, j, k) \cdot \mathbf{S}_{WG}(i, j, k) \quad (6.3)$$

In a first approximation, we only consider the contribution across the nanowire-waveguide interface surface in the  $xy$  plane ( $K \rightarrow 1$  in Eq. 6.3). A problem we face is that the field profiles and spin maps for the NW and waveguide modes are calculated in  $xy$  and  $yz$  planes, respectively (see Fig. 6.17). The waveguide spin map is constructed by "extending" the values along a line in the  $yz$  plane into a surface in the  $xy$  plane as shown in Fig. 6.18, which is another approximation. Nevertheless, we run this scheme for different NW offsets and normalize the values to the FDTD simulation results, see Fig. 6.19. The spin dot product sum can be used to roughly estimate the amount of light coupled into both directions of

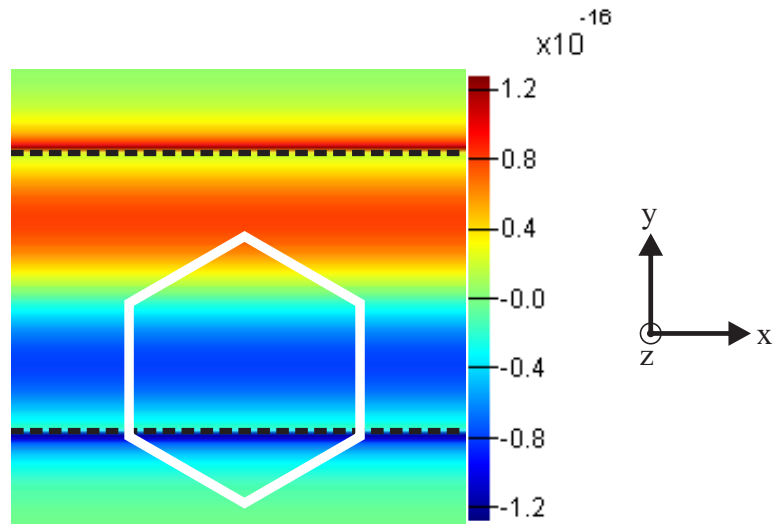


**Figure 6.18:** A map of the waveguide's  $S_z$  spin component in the  $xy$  plane, obtained by extending the spin values from a line along the  $y$  axis to a surface in the  $xy$  plane. The dotted lines mark the edges of the waveguide while the white line outlines the NW, placed on top of the waveguide. The spin overlap at different NW offsets can be calculated by summing the dot product at individual coordinates.

the waveguide. The semi-analytical results follow the trend of the simulation results, but cannot accurately predict the position and magnitude of the ratio between the coupling into both directions. As already mentioned, the directional coupling ratio is dominated by the coupling to the suppressed left direction. Even a small deviation between the semi-analytical result and the result of a full FDTD simulation means a large relative error and consequently a large difference in the obtained coupling ratio and the offset where a peak ratio is observed. In the FDTD simulation results, for example, we obtain a dip at 115 nm for the coupling into the left direction. This is not predicted by the semi-analytical scheme, yet it is the point determining the maximum coupling ratio and the corresponding optimal offset. This shows that full 3D FDTD simulations cannot be replaced by this simplified scheme. However, one can still employ this and similar methods to narrow down the range of values of interest for the offset position, reducing the number of FDTD simulation necessary to approach an optimum offset. The described approach requires a single MODE simulation of the NW and waveguide

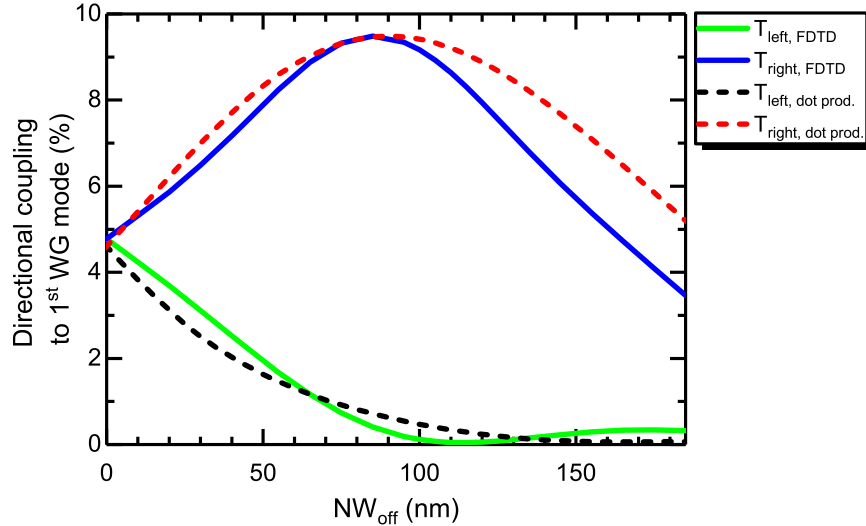


**Figure 6.19:** Comparison of the FDTD Simulation results for the amount of coupled light in both directions (straight lines) and the normalized spin dot products sum (dashed lines, see Eq. 6.3). The sum follows the trend of the simulation results, but does not provide a good estimation of the coupling ratio as it fails to model the minimum in the left direction, which is the main factor in determining the maximum ratio position and magnitude.

structure which takes a few minutes. We can then calculate the spin overlap for a range of different offset values in a matter of seconds. In comparison, a full FDTD simulation for a single offset point takes around an hour.

### 6.2.3 Nanowire Radius

After discussing the importance of the NW offset, we can investigate the properties of individual components of our structure. The NW acts as a source of incident light and in this context, the most interesting variable is its size, i.e., its radius. This geometrical parameter directly influences the  $n_{\text{eff}}$ , the field shape and propagation properties of the supported NW mode(s). At smaller NW radii, only a few modes are guided (approaching the cut-off region), whereas increasing the NW size gives rise to higher order modes, as shown in Fig. 6.2. We are interested in the reflectivity dependence on the NW radius. As the NW offset plays a major

role, one needs to consider several NW positions for each value of the radius. Based on results for the reflectivity at the air facet in Sec. 6.1.3, we expect a decrease in reflectivity for larger NW radii, as part of the light is scattered back into higher order modes. In the smaller NW size range, the reflectivity decreases drastically near the cut-off point (see also Fig. 6.3).

The above considerations are valid for a centrally positioned NW standing on top of a waveguide wide enough for its edges not to play a role in the reflection of light. In other words, when light is reflected from a uniform interface at a certain  $z$  coordinate, i.e., at the nanowire/waveguide or waveguide/substrate interface. Nevertheless, depending on the waveguide geometry and NW offset, we expect there is a NW radius yielding maximum reflectivity in the chosen NW mode.

The results of a NW offset sweep for NW radii between 80 and 200 nm are shown in Fig. 6.20. To investigate only the effect of the NW radius on the whole system, we fixed the waveguide dimensions to the ones of the initial structure (280 nm  $\times$  70 nm). At a central NW position, the highest reflectivity is reached for a NW of 160 nm radius. One would expect the reflectivity to be higher for a smaller NW radius, e.g. the 120 nm radius NW, as larger radii result in a partial scattering of light into higher order NW modes. However, due to the fact that the WG dimensions are fixed, two further effects can influence the reflectivity. Firstly, for larger NW radii, the part of the NW "hanging" over the edge of the waveguide can act as a source for the scattering of light into higher order modes, reducing the reflectivity into the main lasing mode. Secondly, it cannot be excluded that the fixed waveguide height leads to a phase matching condition only at a certain NW radius, as the NW mode itself and its  $n_{\text{eff}}$  change with radius as well.

As shown, the waveguide edge plays a major role in the back reflection of light. The choice of the optimal NW radius which yields a maximum reflectivity is therefore unique for each waveguide geometry and NW offset.

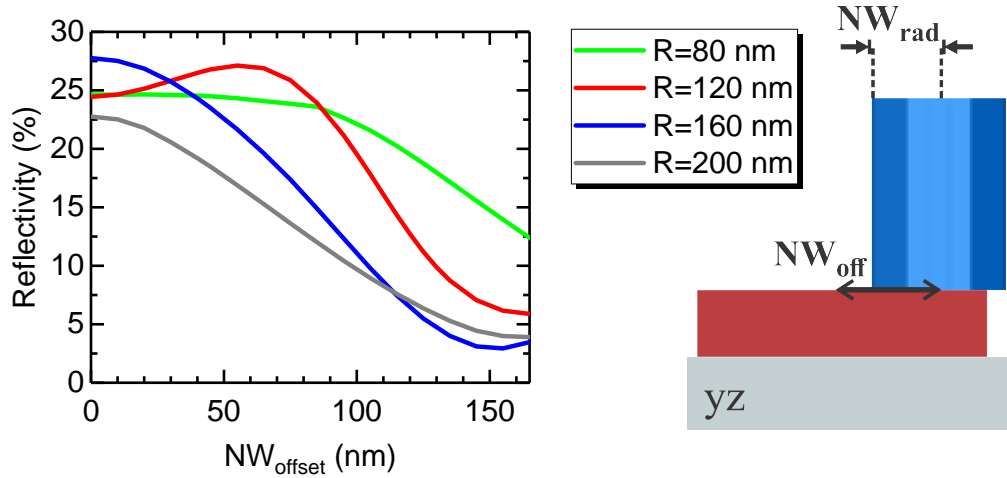


**Figure 6.20:** The effects of NW radius at different offset positions on the waveguide. The reflectivity at the nanowire-waveguide interface decreases with offset for all the simulated radii and is generally higher for smaller NWs, as light is scattered into higher order modes with larger NWs.

## 6.2.4 Waveguide Dimensions

After analyzing the influences of the NW's geometry as the structure providing the source of light, we focus on the other, receiving end - the waveguide - by exploring the influence of its geometry on the coupling. While the shape of the waveguide's cross section remains rectangular, we vary its dimensions. The initial structure remains the same as before: a 120 nm radius NW standing on top of a  $280 \text{ nm} \times 70 \text{ nm}$  rectangular Si waveguide.

### Waveguide Height

We start by computing a sweep of the waveguide height between 40 nm and 90 nm at different NW offsets, while the width of the waveguide is kept constant at 280 nm. In the simulated structure, the back reflected light is a sum of reflections from the nanowire/waveguide and waveguide/substrate interfaces, where interference plays a major role. By changing the waveguide height, we mainly change two parameters which both affect the optical path of light from the waveguide/substrate interface back into the NW. A change in the height results in a change of the  $n_{\text{eff}}$

of the mode, while on the other hand, the distance between the nanowire/waveguide and waveguide/substrate interface is also altered. A maximum reflectivity is achieved when we have constructive interference. Here, we also need to take into account that light waves experience a  $\pi$  phase shift when reflected from a higher index material - in our case, this happens at the nanowire/waveguide interface. For a phase matching of both waves, the wave reflected from the lower refractive index substrate needs to accumulate a  $\pi + 2u\pi$  phase shift, where  $u \in \mathbb{N}$ . In a rough estimation, for a maximum reflectivity, the optical path length  $l$  has to be an odd number multiple of half the wavelength,  $l = (2u - 1)(\lambda/2)$ , where  $u \in \mathbb{N}$  and  $\lambda = \lambda_0/n_{\text{Si}}$ . If we translate this into units of waveguide thickness, we get  $d_{\text{WG}} = \frac{(2u-1)\lambda_0}{4n_{\text{Si}}}$ . By setting  $u = 1$  and using the values from Table 6.2, the first maximum interference should appear at a waveguide thickness of around 55 nm.

As we see in Fig. 6.21(a), at zero offset point, the reflectivity initially goes up with increasing waveguide height, reaching a maximum value of around 26% at a height of 50 nm, then starts decreasing. The height of 50 nm exhibiting a maximum reflectivity is close to the value of 55 nm predicted by the simple analytical expression for constructive interference. A larger range of thicknesses would show a sequence of increasing and decreasing reflectivities, exposing the periodic nature of interference effects (similar as in one of the previous sections, where we varied the thickness of a  $\text{SiO}_2$  layer on top of the NW end facet, see Fig. 6.8). As we shift the NW away from the center of the waveguide, the reflectivities for individual heights first reach a maximum (between 0 nm and 80 nm offset), followed by a minimum (e.g., at 90 nm height and 135 nm offset), then start to increase again etc. Here, the edge of the waveguide starts to play a role - the part of the NW "hanging" over the edge of the waveguide is facing air, which introduces a higher refractive index contrast compared to the Si waveguide, thus we now have several contributing factors for a constructive/destructive interference condition: besides the reflections at the nanowire/waveguide and waveguide/substrate interface, light gets reflected also at the nanowire/air interface.

As already mentioned, a change in the height of the waveguide results also in

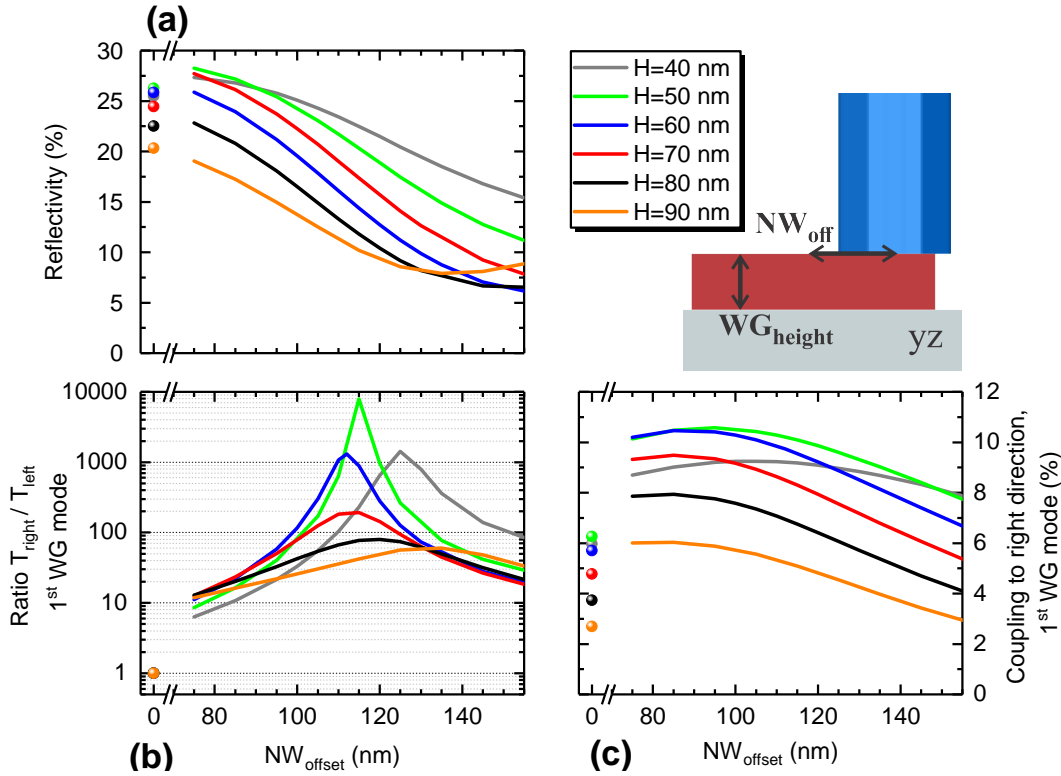


**Figure 6.21:** A NW offset sweep at several waveguide heights. (a) The reflectivity can be tuned with the waveguide height and NW offset (interference effects due to reflection from several interfaces). (b) The coupling ratio changes with waveguide height due to a change in the  $n_{\text{eff}}$  and mode profiles, modifying the coupling conditions. The highest ratio of almost 8000 is reached for a waveguide height of 50 nm. The ratio resonance is narrower when the peak is higher. (c) The coupling versus offset dependency decreases with the waveguide height due to a worse spin overlap between the nanowire and waveguide modes and due to coupling into higher modes. The highest coupling efficiency is achieved with a waveguide height of 50 nm.

a change of the  $n_{\text{eff}}$  of the supported waveguide modes. The modes' field profiles and consequently the corresponding transverse spin components are modified, thus altering the coupling conditions for the incident light. This results in a changed optimal NW offset, as well as in a different coupling ratio peak value. As shown in Fig. 6.21(b), increasing the waveguide height from 40 nm to 60 nm, the coupling ratio peak position moves to smaller offsets, with the maximum peak ratio of almost 8000 at a height of 50 nm and an offset of 115 nm. A further increase of the height reduces the coupling ratio and moves the peak position towards the

edge of the waveguide. This can be associated with a more efficient suppression in the left direction, as these coupling conditions also change with the  $n_{\text{eff}}$  of the waveguide mode. In Fig. 6.21(c) the coupling efficiency into the preferred right direction is plotted. The highest coupling efficiency is achieved with a waveguide height of 50 nm. A further increase in height results in a reduction of the amount of coupled light. This can be accredited to two phenomena - one is the worse overlap between the NW's SAM vectors and the transverse spin components of the waveguide mode, as a consequence of the changed waveguide geometry. The second reason is that an increase in the waveguide height also gives rise to higher order waveguide modes, into which part of the light is coupled, taking away some of the intensity from our desired fundamental waveguide mode.

### Waveguide Width

The other waveguide dimension we can tweak is its width. This again results in a change in the  $n_{\text{eff}}$  of the supported guided modes, altering their field distribution across the waveguide cross-section and consequently modifying their transverse spin components. This in turn changes the coupling conditions for the incident light from the nanowire. In contrast to sweeping the waveguide height, however, a change in the waveguide width does not alter the distance between the nanowire/waveguide and waveguide/substrate interfaces. The optical path is thus changed only due to a change in the  $n_{\text{eff}}$ .

We compute a NW offset sweep for waveguide widths between 200 and 440 nm, while the height is kept constant at the initial value of 70 nm. In the previous parameter studies, the zero NW offset was defined at the center of the waveguide. To make the results more comparable for several waveguide widths, we redefine the offset origin by setting it in the position where we would achieve the best coupling for a point-like dipole source. As we explained already in Sec. 6.2.1, this is the point where the ratio of the longitudinal and transverse electric field components of the fundamental waveguide modes equal one, i.e.,  $\left. \frac{|E_x|}{|E_z|} \right|_{WG} = 1$ . In this position, the evanescent field of the waveguide is circularly polarized and

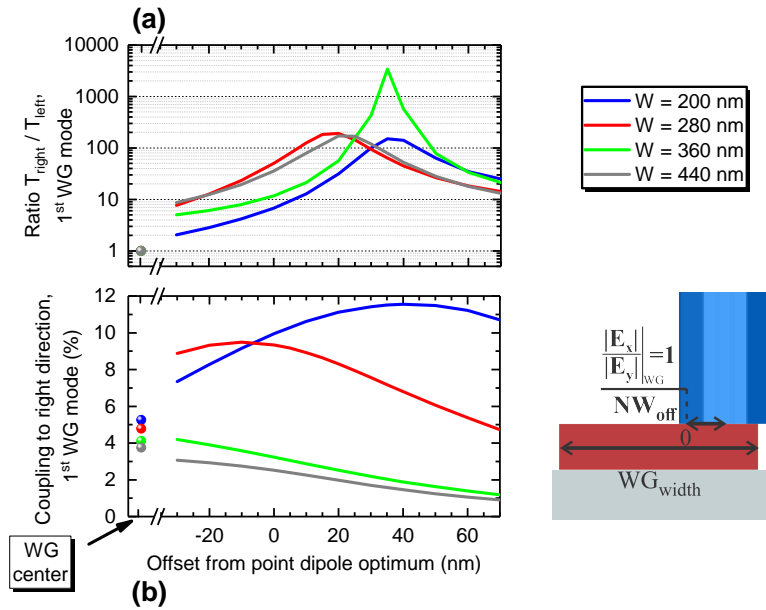


**Figure 6.22:** Results of an offset sweep at several waveguide widths. The offset origin is set to the point where the ratio between  $|E_x|/|E_y| = 1$  for the waveguide mode (optimum point for a point dipole source). **(a)** The highest coupling ratio peak is reached with a 360 nm wide waveguide. **(b)** The coupling efficiency is small if the waveguide is too wide.

has a transverse spin component oriented in the  $z$  direction, resulting in the best alignment with the SAM vector of the incident circularly polarized light. As mentioned before, this is not the optimal point in the case of a NW, which cannot be considered a point-like source anymore. Nevertheless, it can provide a reasonable coordinate origin for an easier comparison between several waveguide widths. In Fig. 6.22(a) one can see that for all the simulated widths, the coupling ratio peak point is positioned further towards the edge of the center when compared to the point-like dipole optimum. Again, the position with a maximal coupling ratio is associated with the point where the coupling in the other, left direction, is suppressed the most. This is the consequence of a minimal spin vectors' alignment and the point of destructive interference. They are both connected with the  $n_{\text{eff}}$  of the waveguide mode, which affects the SAM vectors of the propagating waveguide modes and the interference conditions. A maximum coupling ratio of over 3000 is achieved with a waveguide width of 360 nm at a 35 nm relative offset.

Fig. 6.22(b) plots the coupling efficiency into the preferred right side of the waveguide. Both at a central NW position and at an offset, the coupling efficiency is generally lower for wider waveguides. With an increase of the width, the waveguide supports higher order modes into which part of the light is coupled, which explains the significantly smaller coupling efficiencies for the case of a 360 nm and 440 nm wide waveguide. For the waveguides with widths of 200 nm and 280 nm, the highest coupling efficiency can be associated with the best overlap between the NW's SAM vectors and the transverse spin components of the waveguide mode.

### Height & Width

In the simulations presented in the previous subsections, we swept either through a set of several heights or widths while keeping the other parameter constant. This way we can hardly hope to find an optimal waveguide geometry. A more complete analysis would therefore require a simultaneous sweep of the height and width, which would in turn increase the number of simulation runs by a power of two.

### 6.2.5 Mode Amplitudes Ratio

So far we have only considered a perfectly circularly polarized wave propagating along the nanowire. In principle, we can also use an elliptically polarized light source for unidirectional excitation, as demonstrated in [55]. We explore this possibility by changing the amplitudes ratio between the HE11<sub>a</sub> and HE11<sub>b</sub> modes from 0.6 and 1.4 in steps of 0.2. The HE11<sub>b</sub> mode's  $E_z$  field component is oriented along the waveguide ( $x$  axis), while the  $E_z$  component of the HE11<sub>a</sub> mode is perpendicular to the waveguide, or in other words, aligned with the  $y$  axis direction. The difference in the modes' amplitudes results in an elliptically polarized wave propagating along the NW. The profiles of the magnitude of the  $E_z$  component are shown in the upper part of Fig. 6.23 for  $\frac{b}{a}$  mode ratios of 0.6,

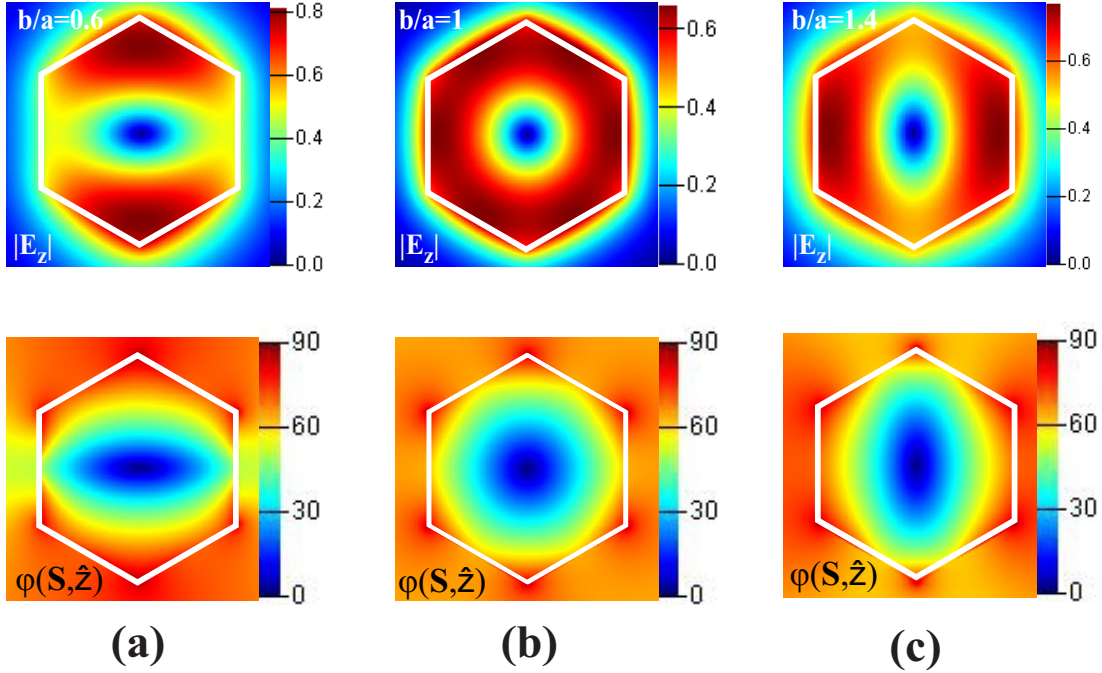


**Figure 6.23:** The upper row plots the profiles of the  $E_z$  electric field component magnitudes for elliptically (circularly) polarized waves, while the bottom row shows the corresponding maps of the angle between the spin angular momentum vector  $\mathbf{S}$  and the  $z$  axis for mode power ratios  $\frac{P(\text{HE}_{11b})}{P(\text{HE}_{11a})}$  of 0.6, 1 and 1.4 in (a), (b) and (c), respectively.

1 and 1.4. We can see that the elliptical polarization (the ellipse semimajor axis) is oriented along the  $y$  axis for  $\frac{b}{a} < 1$  and along the  $x$  axis for  $\frac{b}{a} > 1$ .

Another important aspect to consider is the effect of elliptical polarization of light on its spin angular momentum (SAM) vector  $\mathbf{S} = [S_x, S_y, S_z]^T$ . As shown in Sec. 4.3,  $\mathbf{S}$  can be determined from the electric field profile of the propagating light using the relation

$$\mathbf{S} = -\frac{i\epsilon_0}{2\omega} \mathbf{E}^* \times \mathbf{E} \quad (6.4)$$

As is evident from Fig. 6.13 which displays the different field components for the fundamental waveguide mode, the  $E_z$  component is practically negligible except for a small region near the waveguide vertices. We expand the Eq. 6.4 for the individual components, e.g.  $S_z = -\frac{i\epsilon_0}{2\omega} (E_x^* E_y - E_x E_y^*)$ . One can conclude that  $S_z$  is the dominant component along most of the cross-section of the NW,

as  $S_x$  and  $S_y$  include a dependency on  $E_z$ . The  $E_x$  and  $E_y$  components from the above equation for  $S_z$  depend on the HE11<sub>a</sub> and HE11<sub>b</sub> mode contributions, respectively. When changing the  $\frac{b}{a}$  ratio, we increase one of the mode components while decreasing the other, so neither the shape nor the magnitudes of the  $S_z$  vector across the NW cross-section are changed significantly. In the bottom part of Fig. 6.23, the corresponding maps of the angle  $\varphi(\mathbf{S}, \hat{\mathbf{z}})$  between the SAM vector  $\mathbf{S}$  of the light, propagating along the NW and the unit vector  $\hat{\mathbf{z}}$  of the axis of propagation  $z$  are shown. The angles at individual points can be computed using the formula

$$\varphi(\mathbf{S}, \hat{\mathbf{z}}) = \arctan\left(\frac{S_z}{\sqrt{S_x^2 + S_y^2}}\right) \quad (6.5)$$

We can see that the minimum angle between the SAM vector  $\mathbf{S}$  and the axis of propagation is at the center of the waveguide for all the mode amplitude ratios. In the case of a perfectly circularly polarized wave, the angle increases radially towards the edges of the nanowire, regardless of the direction (Fig. 6.23). For elliptically polarized waves, however, the angle retains a smaller value longer along the axis perpendicular to the dominant polarization axis (see Fig. 6.23(a, b)). This has important consequences as the spin-orbit coupling mechanism, responsible for our unidirectional coupling, depends on the amplitude of  $\mathbf{S}_{\text{NW}}$  and  $\mathbf{S}_{\text{WG}}$  as well as on their alignment, as we have argued already in Eq. 6.3.

We compute NW offset sweeps for several  $\frac{b}{a}$  amplitude ratios. The results presented in Fig. 6.24(a) show that by changing the ratio between the  $a$  and  $b$  mode components, we can shift the position of the coupling ratio peak. By increasing the HE11<sub>b</sub> component contribution, the ratio peak position moves towards the center of the waveguide. On the other hand, increasing the HE11<sub>a</sub> component moves it towards the waveguide edge. This is a consequence of the change of the SAM vector  $\mathbf{S}$  across the NW's cross-section with the changed polarization of the propagating light (as we discussed and showed in the bottom row in Fig. 6.23). This causes the NW offset with the minimum coupling in the suppressed waveguide side to shift. In Fig. 6.24(b) we plot the coupling efficiency

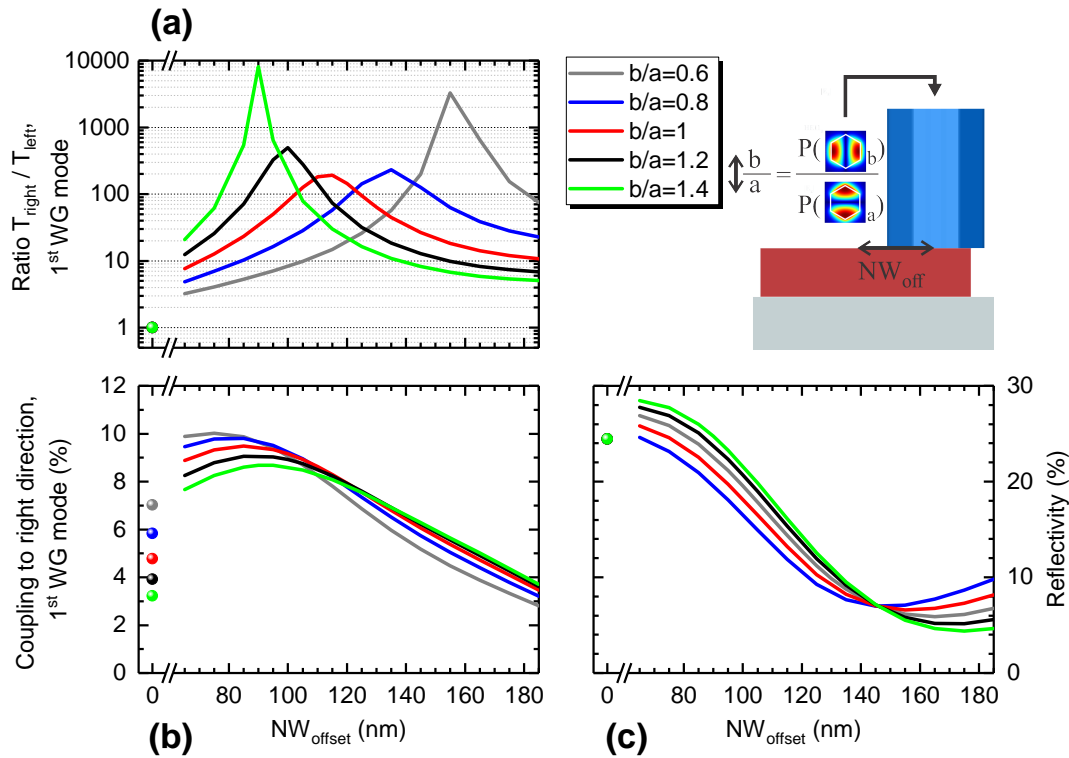


**Figure 6.24:** Simulation results for several  $b/a$  ratios, i.e., the power ratio between the  $HE_{11_b}$  and  $HE_{11_b}$  mode mixture. (a) shows that we can shift the directional coupling peak towards the center (edge) of the waveguide by increasing (decreasing) the  $b/a$  ratio. In (b) and (c) one can see that a change in the mentioned ratio does not significantly affect the coupling efficiency and reflectivity, proving it as a possible mechanism for shifting the peak position without significantly affecting the other properties of interest.

into the right direction of the waveguide. At zero NW offset, the coupling is higher for lower  $\frac{b}{a}$  ratios, owing to a better spin overlap of the NW and waveguide mode. As the offset is increased, the coupling first reaches a maximum and then starts to decrease. In that region of larger offsets, the higher  $\frac{b}{a}$  ratios provide a slightly better coupling. This can be explained by looking at the spin angle profiles in the bottom row of Fig. 6.23 again. At smaller NW offsets, a ratio of  $\frac{b}{a} < 1$  (Fig. 6.23(a)) ensures the whole NW cross-section part with the relatively smaller angles  $\varphi(\mathbf{S}, \hat{\mathbf{z}})$  (contributing to the coupling the most) is covering the waveguide mode area. For ratios of  $\frac{b}{a} > 1$ , the side parts with the relatively smaller angles  $\varphi(\mathbf{S}, \hat{\mathbf{z}})$  are away from the waveguide mode area. At larger offsets where the

NW is partially off the waveguide, the situation is different - the  $\frac{b}{a} > 1$  provides a better overlap, whereas for the  $\frac{b}{a} < 1$ , the NW part with the smaller angles  $\varphi(\mathbf{S}, \hat{\mathbf{z}})$  is further away from the overlap region with the waveguide's transverse spin. Overall, the coupling efficiency follows a similar trend and has comparable values for all the investigated  $\frac{b}{a}$  ratios.

In Fig. 6.24(c) are the reflectivities at different offsets for the chosen amplitude ratios. At a central NW position, the reflectivity is the same for all of the modes. With an increasing offset, the reflectivities follow a similar trend: first a maximum, then a decrease, followed by a minimum, and another increase etc. This can be associated with the waveguide edge playing a role in the interference of light waves reflected from the nanowire/waveguide and waveguide/substrate interfaces, as some of the light is also reflected at the nanowire/air interface (as discussed already in the height sweep). At an offset, there are small differences in the reflectivity for the different mode component ratios  $\frac{b}{a}$ . We can explain this by looking at the top part of Fig. 6.23. The  $E_z$  component field distributions shown in the figure contribute to the total electric field intensity which becomes slightly more elliptical. The semimajor axis of this ellipse is oriented along the  $y$  axis for  $\frac{b}{a} < 1$  (Fig. 6.23(a)) and along the  $x$  axis for  $\frac{b}{a} > 1$  (Fig. 6.23(b)). At a given NW offset, a different fraction of the light intensity propagates in the part of the NW "hanging" beyond the waveguide. As a consequence, the amount of reflected light and the interference conditions differ for each  $\frac{b}{a}$  ratio, hence the slight difference in reflectivity.

We have shown that with a change in the amplitude ratio of the HE<sub>11a</sub> and HE<sub>11b</sub> we can construct an elliptically polarized wave, propagating along the NW. With the change of the amplitudes ratio we can shift the waveguide coupling ratio peak offset, while the coupling efficiency and reflectivity do not change significantly. This provides a mechanism to tune the NW offset producing the coupling ratio peak without affecting the dependency of other parameters of interest, namely coupling efficiency and reflectivity.

### 6.2.6 SiO<sub>2</sub> Layer

In the simulation results presented so far, we considered a simple waveguide consisting only of a rectangularly shaped silicon core. However, for a site-selective growth of nanowires, a SiO<sub>2</sub> intermediate layer is necessary in the developed fabrication process [25]. The oxide layer influences the process of light coupling on several levels. As it is positioned between the nanowire and the waveguide surface, it separates our incident circularly polarized light from the waveguide into which we want to couple the light. We expect the coupling efficiency to reduce, as we speculate a part of the light to be lost, propagating along the oxide/air interface where it decays quickly. On the other hand, the oxide acts as a spacer layer - by varying its thickness, we can change the length of the optical path of the light, reflected from the waveguide/nanowire end facet ( $l = 2(h_{WG} + d_{SiO_2})$ ). To meet the phase matching condition for constructive interference with the light, reflected from the nanowire/oxide interface, the optical path length  $l$  needs to equal  $l = u\lambda$ , where  $u \in \mathbb{N}$  and  $\lambda = \lambda_0 2(h_{WG} + d_{SiO_2}) / (h_{WG}n_{Si} + d_{SiO_2}n_{SiO_2})$ . As guided modes are supported only inside the Si core of the waveguide, we can tune the oxide height and thus achieve a high reflectivity without affecting the  $n_{\text{eff}}$  and the field profile of the waveguide mode of interest.

In our study, we compute a sweep of the NW offset for a 280 nm  $\times$  70 nm waveguide with a SiO<sub>2</sub> layer on top for oxide thicknesses between 40 and 160 nm. The results are compared with the initial structure with no oxide layer. As one can see in Fig. 6.25(a, b), both the coupling ratio and the coupling efficiency decrease with increasing oxide thickness. As the incident circularly polarized light reaches the oxide-layered waveguide, it couples through the spin-orbit interaction, as in the cases with the simple Si core waveguide. The amount of coupled light depends on the spin overlap of the incident light SAM vector and the transverse spin of the evanescent field of the waveguide mode. The difference now is, that the evanescent wave region where the coupling is largest is now filled up by the oxide. As a consequence, a large fraction of the incident light propagates along

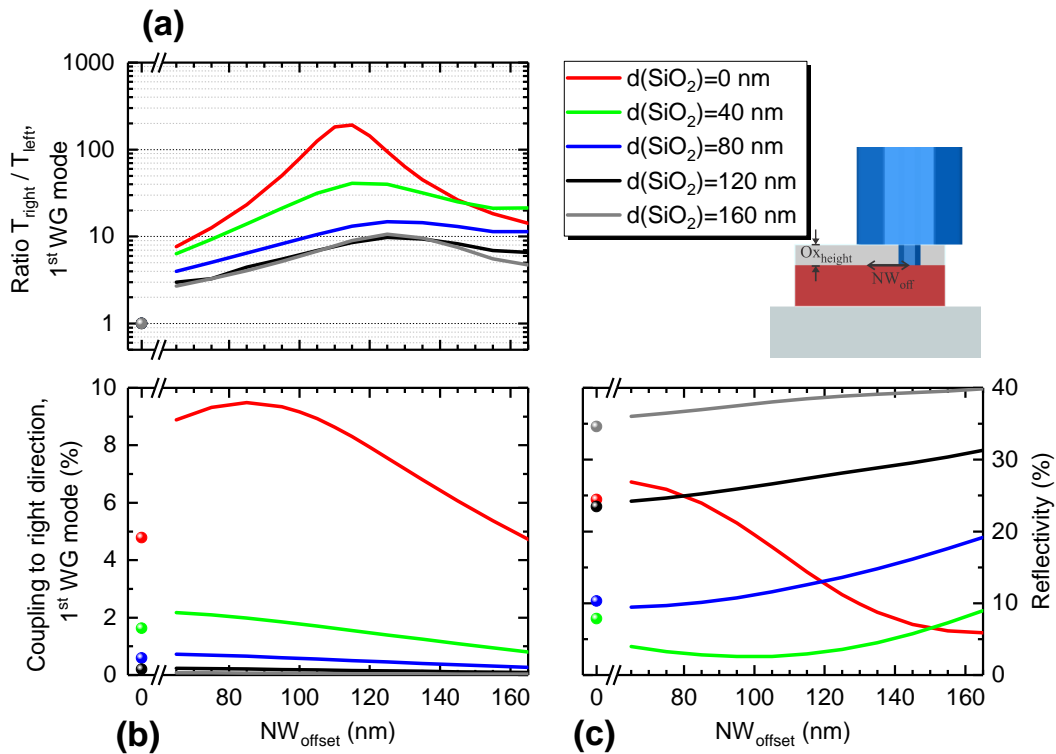


**Figure 6.25:** The results of a NW offset sweep for the case of a waveguide with a SiO<sub>2</sub> oxide layer of several thicknesses. (a) and (b) show that the coupling ratio peak as well as the coupling efficiency into the preferred direction are reduced significantly by the introduction of an oxide layer, only getting worse with increasing thickness. (c) The reflectivity can be enhanced by tuning the oxide height (phase matching).

the oxide-air interface, as can be seen in Fig. 6.26. As this light is not an actual mode guided in the waveguide, it decays quickly. A large proportion of the light intensity is therefore lost and the coupling efficiency to the guided waveguide modes is lower. This gets even worse with a thicker oxide as the distance between the nanowire and the silicon waveguide increases.

While the (unidirectional) coupling is severely degraded, the reflectivity can be greatly enhanced. As mentioned, the change in the oxide thickness does not affect the  $n_{\text{eff}}$  of the propagating waveguide modes. By selecting an appropriate oxide thickness, we can satisfy the phase-matching conditions for a constructive interference. This can be seen in Fig. 6.25(c). The red line shows the reflectivity

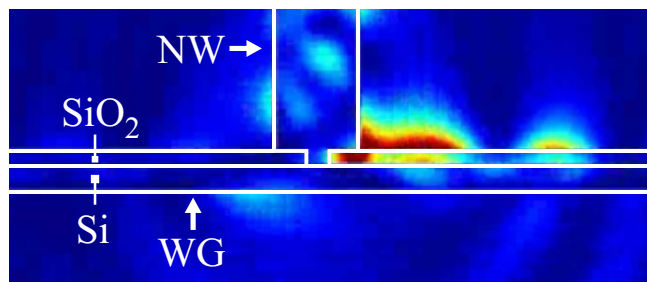


**Figure 6.26:** Even a 40 nm thick SiO<sub>2</sub> oxide layer causes a large fraction of the light to propagate on the oxide-air interface where it decays quickly.

dependence for the case with no oxide. One can see that the reflectivity changes severely with the NW offset which demonstrates that the waveguide edge plays a strong role in the amount of back reflected light, as well as in satisfying the interference conditions (see also explanation from the height sweep). The reflectivities for the case of an oxide layer change much less with the NW offset. The SiO<sub>2</sub> has a refractive index of around 1.45 and presents a large index contrast to the nanowire, similar as a nanowire-air interface. This means that the edge of the waveguide presents a smaller difference for the reflection interface, thus the NW offset plays a smaller role in the reflectivity. Changing the thickness of the oxide layer greatly affects the reflectivity, caused by a change in the optical path length of light reflected from the waveguide/substrate interface. This can be nicely seen in Fig.6.25(c) - for oxide thicknesses of 40 and 80 nm, the total optical path length is closer to a destructive interference condition, while at 120 and 160 nm it approaches a constructive interference, with a reflectivity enhancement. A further increase of the oxide thickness would show a periodic rise and fall of the reflectivity values, as is common for interference effects.

We have shown that despite a significant increase in reflectivity, the introduction of an oxide layer presents a drawback in the context of efficient unidirectional coupling.

## 6.3 Summary

In this chapter we presented the results of numerical simulations of several NW and WG structures that we computed to study their properties and optimize their geometries.

Starting with a standalone nanowire surrounded by air, we first completed an eigenmode analysis. These results showed that with a large NW radius, several higher order modes can propagate in the NW cavity. The effective refractive index  $n_{\text{eff}}$  of the individual modes approaches the refractive index  $n_{\text{GaAs}}$  of the bulk NW material with increasing NW radius. At decreasing NW radii, the individual modes reach their cut-off, when their  $n_{\text{eff}}$  falls below the effective index of the surrounding medium  $n_{\text{air}}$  and the mode is no longer guided along the NW. By means of 3D FDTD simulations, we determined for some of the supported modes the reflectivity of the top end flat facet for different NW radii. The reflectivities of individual modes experience a steep decrease and drop to 0% at cut-off. At larger NW radii, the reflectivities are reduced due to scattering into higher order modes. Introducing a metal mirror on top of the end facet can enhance the reflectivity. In the case of the fundamental HE<sub>11</sub> mode, it can be increased from around 40% to around 90%. In some cases, e.g., with metal contacts for electrical pumping, an intermediate oxide layer is necessary as an insulating layer. With variable oxide thickness, the reflectivity displays minima and maxima due to a change in the optical path length, which is typical for interference effects.

The next studied structure was a NW positioned on top of a rectangular Si waveguide on a SOI platform. By mixing the two degenerated HE<sub>11</sub> modes (HE<sub>11a</sub> and HE<sub>11b</sub>), phase shifted by  $\pi/2$ , a circularly polarized wave can propagate in the NW. Combining such a wave with a displacement of the NW position on top of the waveguide, we break the symmetry and achieve unidirectional coupling into the waveguide. In other words, through the spin-orbit interaction of the spin angular momentum (SAM) vector  $\mathbf{S}$  of the incident light from the NW with the transverse spin of the evanescent field region of the waveguide mode, more

light is coupled into one direction of the waveguide compared to the other. The unidirectional coupling ratios can reach values of nearly  $10^4$ . They exhibit a great sensitivity on the NW offset position, where a shift of only 10 nm can change the ratio by an order of magnitude. The other properties of interest, namely the coupling efficiency into the waveguide and the reflectivity back into the NW show a weaker dependence on position. They can reach values of around 10% and 30%, respectively. The coupling efficiency into the preferred direction can be explained with the spin overlap of the NW and WG modes and can be roughly estimated by an integral of their dot product throughout the overlapping region. The dips in the coupling efficiency of the suppressed direction can be accredited to destructive interference effects. The coupling ratio is dominated by the coupling in the suppressed direction, as the latter experiences large relative differences with the offset (small absolute values). The reflectivities of the individual degenerated NW modes HE11<sub>a</sub> and HE11<sub>b</sub> show different reflectivities depending on the NW displacement.

The NW radius affects the reflectivity greatly. The NW radius which yields a maximum reflectivity depends on the WG dimensions and on the offset of the NW. The reflectivities reach values near 30%. A large NW radius results in additional losses of reflected light due to scattering into higher order modes.

The waveguide (WG) dimensions play an important role in the coupling mechanism. Varying the WG height results in a change of the  $n_{\text{eff}}$  of the mode and its field shape as well as in a change of the optical path between the NW/WG and WG/substrate interface. A change of the height therefore greatly affects the reflectivity. A coupling ratio value of nearly 8000, a coupling efficiency of over 10% and a reflectivity of around 20% are reached employing a WG with dimensions of 280 nm  $\times$  50 nm. Varying the width of the WG also results in a change in the  $n_{\text{eff}}$  and field profiles of the guided modes. In contrast to a change of height, it does not alter the distance between the NW/WG and WG/substrate interfaces. A coupling ratio peak of above 3000, a coupling efficiency of around 2% and a reflectivity of almost 10% are reached for a WG with dimensions of

360 nm  $\times$  70 nm. The lower coupling efficiency is a consequence of the larger WG dimensions which support higher order modes into which part of the light is coupled. The height and width of the WG are of course not independent parameters. To find an optimal WG geometry, one should sweep through both parameters simultaneously, which increases the number of required simulation runs by a power of 2. A general rule to follow is to tune the WG dimensions in such a way, i.e., keep them small enough, that the WG supports only the fundamental mode. With larger WG dimensions, higher order modes appear into which part of the light is coupled, reducing the overall coupling efficiency to the fundamental WG mode.

By changing the amplitude ratio between the HE11<sub>b</sub> and HE11<sub>a</sub> mode components, an elliptically polarized wave can be constructed. This affects the propagating field profile and consequently the spin angular momentum (SAM) vector  $\mathbf{S}$ . The NW offset where a peak in the unidirectional coupling ratio is observed can be shifted with a change in the mode amplitudes ratio. On the other hand, the coupling efficiency and reflectivity do not change significantly with the amplitude ratio. The amplitude ratio change thus provides a mechanism to shift the position where a maximum coupling ratio is observed, essentially without degrading the coupling efficiency or reflectivity.

The introduction of a SiO<sub>2</sub> intermediate layer between the Si WG and the NW, which is necessary in some fabrication processes, results in a severe reduction of the coupling ratio and the coupling efficiency. This is due to the propagation of part of the light along the oxide/air interface, where it decays quickly. On the other hand, the oxide acts also as a spacer layer whose thickness leads to a constructive or destructive interference of the back reflected waves. This way, the reflectivity can be greatly enhanced by varying the thickness of the oxide layer without changing the WG dimensions and consequently the  $n_{\text{eff}}$  and mode shapes.

The simulation results have shown that we can in principle achieve unidirectional coupling into a proximal WG by asymmetrically placing a NW with a circularly/elliptically polarized propagating wave on top of it.



# Chapter 7

## Conclusion

In this thesis, we investigated different nanowire and waveguide structures by means of numerical simulations.

The eigenmode analysis of a GaAs-AlGaAs core-shell nanowire laser showed that the NW body acts as a low-loss waveguide. Depending on the NW radius, it can support several transversal modes, up until the cut-off point which appears at a different NW radius for each mode. This proves that we need to be precise in the NW growth stage to obtain the desired NW radius, otherwise the field shape could change severely. We showed that by adding a simple metal layer on top of the end facet which faces air, the reflectivity can be greatly enhanced. There are other possibilities of increasing the reflectivity, such as distributed Bragg reflectors (DBRs), but these structures could be more challenging to implement in reality.

It has been shown that a circularly polarized mode can be guided along the NW by mixing two degenerate  $a$  and  $b$  modes, phase shifted by  $\pi/2$ . In practical realizations, a gain medium that would provide a circularly polarized mode upon pumping excitation is required. The simulation results show that unidirectional coupling into waveguides is in principle possible with off-center positioned NWs. The amount of coupled light into the preferred waveguide direction can be associated with the spin overlap between the NW and WG modes. The unidirectional coupling ratio can in some configurations reach a peak value of almost  $10^4$ , but

is extremely sensitive to the NW offset position. A shift by only 10 nm can degrade the coupling ratio by an order of magnitude. This is a severe drawback for practical realizations, as an extreme positioning precision would be necessary. It is also questionable to which offset NW growth is possible. Shifting the NW core beyond the waveguide edge is not compatible with the current fabrication process. The latter also requires an intermediate SiO<sub>2</sub> layer, into which holes are etched. These then act as locations for a site-selective growth of NWs. As is evident from the simulation results, the oxide layer can increase the reflectivity, but degrades the coupling ratio and coupling efficiency severely. This happens as a portion of the light is lost, propagating and quickly decaying at the oxide/air interface. Removing the oxide layer after the NW growth could perhaps mitigate this problem.

As demonstrated in the results section, the unidirectional coupling depends on a number of different parameters: the NW offset, the NW radius, the waveguide dimensions, the oxide thickness, the polarization of the incident light and possibly on several others. As these parameters are not independent from each other (e.g., the influence of the WG height changes with WG width), a huge parameter space is formed, making it impossible to sweep through all the parameter combinations and find the optimum. A more complete understanding of the underlying phenomena and the interrelations between the different parameters would be crucial in limiting the range of values for individual parameters. To some extent, we can limit the range of possible values for the NW and WG dimensions by setting the condition of single-mode guiding, which is desired for better coupling efficiencies in the waveguide and higher reflectivities back into the NW.

Despite the problems in finding the optimal structure geometry (due to the huge parameter space) and difficulties we would face in trying to fabricate our structures (mainly arising from the extreme relative position sensitivities), the simulation results have proven useful. For the first time, we showed that unidirectional coupling into waveguides is in principle possible by an asymmetrically

placed NW with a circularly polarized propagating field. In most of the successful studies so far, 0D-like scatterers, e.g., quantum dots (QDs) and nanoparticles which act as point-like dipole sources have been employed. In contrast, the NW as a 3D object has a 2D overlap with the Si waveguide. The task of finding the optimal placement of our source of incident light therefore becomes much more challenging.

In conclusion, we provided Proof-Of-Concept results in the simulation domain that highlight the influences of different parameters towards achieving unidirectional coupling in Si waveguides by facilitating a NW laser as the source of incident light. The next step would certainly be to prove this concept works experimentally. Even though we would not be able to hit the perfect offset position on the WG, in a first step we only require the possibilities of growing NWs asymmetrically on the WG and exciting a circularly (or at least elliptically) polarized wave propagating along the NW. This should suffice to observe an asymmetric coupling in both waveguide directions, albeit reaching a lower unidirectional coupling ratio than the one foreseen by the 3D FDTD simulations.



# Bibliography

- [1] G. E. Moore, “Cramming more components onto integrated circuits,” *Electronics*, vol. 38, pp. 114–117, sep 1965.
- [2] R. Kirchain and L. Kimerling, “A roadmap for nanophotonics,” *Nature Photonics*, vol. 1, pp. 303–305, jun 2007.
- [3] P. Moser, *Energy-Efficient VCSELs for Optical Interconnects*. Springer Theses, Cham: Springer International Publishing, 2016.
- [4] H. Li, P. Wolf, P. Moser, G. Larisch, J. A. Lott, and D. Bimberg, “Vertical-cavity surface-emitting lasers for optical interconnects,” *SPIE Newsroom*, nov 2014.
- [5] J. F. Bauters, M. J. R. Heck, D. John, D. Dai, M.-C. Tien, J. S. Barton, A. Leinse, R. G. Heideman, D. J. Blumenthal, and J. E. Bowers, “Ultra-low-loss high-aspect-ratio Si<sub>3</sub>N<sub>4</sub> waveguides,” *Optics Express*, vol. 19, pp. 3163–3174, feb 2011.
- [6] J. Cardenas, C. B. Poitras, J. T. Robinson, K. Preston, L. Chen, and M. Lipson, “Low loss etchless silicon photonic waveguides,” *Optics Express*, vol. 17, pp. 4752–4757, mar 2009.
- [7] Z. Lu, H. Yun, Y. Wang, Z. Chen, F. Zhang, N. A. F. Jaeger, and L. Chrostowski, “Broadband silicon photonic directional coupler using asymmetric-waveguide based phase control,” *Optics Express*, vol. 23, feb 2015.

- 
- [8] P. Orlandi, F. Morichetti, M. J. Strain, M. Sorel, A. Melloni, and P. Bassi, “Tunable silicon photonics directional coupler driven by a transverse temperature gradient,” *Optics Letters*, vol. 38, pp. 863–865, mar 2013.
- [9] D. Patel, S. Ghosh, M. Chagnon, A. Samani, V. Veerasubramanian, M. Osman, and D. V. Plant, “Design, analysis, and transmission system performance of a 41 GHz silicon photonic modulator,” *Optics Express*, vol. 23, pp. 14263–14287, jun 2015.
- [10] X. Zheng, E. Chang, P. Amberg, I. Shubin, J. Lexau, F. Liu, H. Thacker, S. S. Djordjevic, S. Lin, Y. Luo, J. Yao, J.-H. Lee, K. Raj, R. Ho, J. E. Cunningham, and A. V. Krishnamoorthy, “A high-speed, tunable silicon photonic ring modulator integrated with ultra-efficient active wavelength control,” *Optics Express*, vol. 22, p. 12628, may 2014.
- [11] O. Lopez-Sanchez, D. Lembke, M. Kayci, A. Radenovic, and A. Kis, “Ultra-sensitive photodetectors based on monolayer MoS<sub>2</sub>,” *Nature Nanotechnology*, vol. 8, pp. 497–501, jun 2013.
- [12] C.-H. Liu, Y.-C. Chang, T. B. Norris, and Z. Zhong, “Graphene photodetectors with ultra-broadband and high responsivity at room temperature,” *Nature Nanotechnology*, vol. 9, pp. 273–278, mar 2014.
- [13] X. Zheng, I. Shubin, G. Li, T. Pinguet, A. Mekis, J. Yao, H. Thacker, Y. Luo, J. Costa, K. Raj, J. E. Cunningham, and A. V. Krishnamoorthy, “A tunable 1x4 silicon CMOS photonic wavelength multiplexer/demultiplexer for dense optical interconnects,” *Optics Express*, vol. 18, p. 5151, mar 2010.
- [14] A. M. J. Koonen, Haoshuo Chen, H. P. A. van den Boom, and O. Raz, “Silicon Photonic Integrated Mode Multiplexer and Demultiplexer,” *IEEE Photonics Technology Letters*, vol. 24, pp. 1961–1964, nov 2013.

- 
- [15] Y. A. Vlasov, “Silicon Integrated Nanophotonics: Road from Scientific Explorations to Practical Applications,” in *plenary talk CLEO, United States*, 2012.
- [16] N. Koshida and H. Koyama, “Visible electroluminescence from porous silicon,” *Applied Physics Letters*, vol. 60, pp. 347–349, jan 1992.
- [17] L. Pavesi, L. Dal Negro, C. Mazzoleni, G. Franzò, and F. Priolo, “Optical gain in silicon nanocrystals,” *Nature*, vol. 408, pp. 440–444, nov 2000.
- [18] H. Rong, A. Liu, R. Jones, O. Cohen, D. Hak, R. Nicolaescu, A. Fang, and M. Paniccia, “An all-silicon Raman laser,” *Nature*, vol. 433, pp. 292–294, jan 2005.
- [19] M. Miritello, R. Lo Savio, F. Iacona, G. Franzò, A. Irrera, A. M. Piro, C. Bongiorno, and F. Priolo, “Efficient Luminescence and Energy Transfer in Erbium Silicate Thin Films,” *Advanced Materials*, vol. 19, pp. 1582–1588, jun 2007.
- [20] R. E. Camacho-Aguilera, Y. Cai, N. Patel, J. T. Bessette, M. Romagnoli, L. C. Kimerling, and J. Michel, “An electrically pumped germanium laser,” *Optics Express*, vol. 20, pp. 11316–11320, may 2012.
- [21] J. Liu, X. Sun, R. Camacho-Aguilera, L. C. Kimerling, and J. Michel, “Ge-on-Si laser operating at room temperature,” *Optics Letters*, vol. 35, pp. 679–68, mar 2010.
- [22] K. P. Homewood and M. A. Lourenço, “The rise of the GeSn laser,” *Nature Photonics*, vol. 9, pp. 78–79, 2015.
- [23] H. Park, A. W. Fang, S. Kodama, J. E. Bowers, and A. Liu, “Hybrid silicon evanescent laser fabricated with a silicon waveguide and III-V offset quantum wells,” *Quantum Electron. OSA OPTICS EXPRESS*, vol. 8, no. 9460, pp. 118–131, 2005.

- [24] Z. Zhou, B. Yin, and J. Michel, “On-chip light sources for silicon photonics,” *Light: Science & Applications*, vol. 4, 2015.
- [25] G. Koblmüller, B. Mayer, T. Stettner, G. Abstreiter, and J. J. Finley, “GaAs–AlGaAs core–shell nanowire lasers on silicon: invited review,” *Semiconductor Science and Technology*, vol. 32, may 2017.
- [26] B. Mayer, D. Rudolph, J. Schnell, S. Morkötter, J. Winnerl, J. Treu, K. Müller, G. Bracher, G. Abstreiter, G. Koblmüller, and J. J. Finley, “Lasing from individual GaAs–AlGaAs core–shell nanowires up to room temperature,” *Nature Communications*, vol. 4, 2013.
- [27] B. Mayer, L. Janker, B. Loitsch, J. Treu, T. Kostenbader, S. Lichtmannecker, T. Reichert, S. Morkötter, M. Kaniber, G. Abstreiter, C. Gies, G. Koblmüller, and J. J. Finley, “Monolithically Integrated High- $\beta$  Nanowire Lasers on Silicon,” *Nano Letters*, vol. 16, pp. 152–156, jan 2016.
- [28] T. Stettner, P. Zimmermann, B. Loitsch, M. Döblinger, A. Regler, B. Mayer, J. Winnerl, S. Matich, H. Riedl, M. Kaniber, G. Abstreiter, G. Koblmüller, and J. J. Finley, “Coaxial GaAs–AlGaAs core–multishell nanowire lasers with epitaxial gain control,” *Applied Physics Letters*, vol. 108, p. 011108, jan 2016.
- [29] T. Stettner, T. Kostenbader, D. Ruhstorfer, J. Bissinger, H. Riedl, M. Kaniber, G. Koblmüller, and J. J. Finley, “Direct Coupling of Coherent Emission from Site-Selectively Grown III–V Nanowire Lasers into Proximal Silicon Waveguides,” *ACS Photonics*, sep 2017.
- [30] C. H. Townes, *How the laser happened : adventures of a scientist*. Oxford University Press, 1999.
- [31] B. Jean and T. Bende, “Mid-IR Laser Applications in Medicine,” in *Solid-State Mid-Infrared Laser Sources*, pp. 530–565, Berlin, Heidelberg: Springer Berlin Heidelberg, 2003.

- [32] K. F. Renk, *Basics of laser physics : for students of science and engineering*. Springer, 2012.
- [33] S. L. Chuang, *Physics of optoelectronic devices*. Wiley, 1995.
- [34] M. A. M. Fox, *Quantum optics : an introduction*. Oxford University Press, 2006.
- [35] W. T. Silfvast, *Laser fundamentals*. Cambridge University Press, 2004.
- [36] G. Björk, A. Karlsson, and Y. Yamamoto, “Definition of a laser threshold,” *Physical Review A*, vol. 50, pp. 1675–1680, aug 1994.
- [37] C. Z. Ning, “What is Laser Threshold?,” *IEEE Journal of Selected Topics in Quantum Electronics*, vol. 19, p. 1503604, jul 2013.
- [38] P. W. Milonni and J. H. Eberly, *Lasers*. Wiley, 1988.
- [39] K. Okamoto, *Fundamentals of optical waveguides*. Academic Press, 2 ed., 2010.
- [40] D. B. Li and C. Z. Ning, “Peculiar features of confinement factors in a metal-semiconductor waveguide,” *Applied Physics Letters*, vol. 96, may 2010.
- [41] D. Rudolph, S. Funk, M. Döblinger, S. Morkötter, S. Hertenberger, L. Schweickert, J. Becker, S. Matich, M. Bichler, D. Spirkoska, I. Zardo, J. J. Finley, G. Abstreiter, and G. Koblmüller, “Spontaneous Alloy Composition Ordering in GaAs-AlGaAs Core-Shell Nanowires,” *Nano Letters*, vol. 13, pp. 1522–1527, apr 2013.
- [42] F. Glas, “Critical dimensions for the plastic relaxation of strained axial heterostructures in free-standing nanowires,” *Physical Review B*, vol. 74, sep 2006.
- [43] C. Downs and T. Vandervelde, “Progress in Infrared Photodetectors Since 2000,” *Sensors*, vol. 13, pp. 5054–5098, apr 2013.

- [44] M. J. Adams, *An introduction to optical waveguides*. Wiley, 1981.
- [45] P. Lodahl, S. Mahmoodian, S. Stobbe, A. Rauschenbeutel, P. Schneeweiss, J. Volz, H. Pichler, and P. Zoller, “Chiral quantum optics,” *Nature*, vol. 541, no. 3, pp. 473–480, 2017.
- [46] H. J. Carmichael, “Quantum trajectory theory for cascaded open systems,” *Physical Review Letters*, vol. 70, pp. 2273–2276, apr 1993.
- [47] L. L. Allen, S. M. S. M. Barnett, and M. J. Padgett, *Optical angular momentum*. Institute of Physics Pub, 2003.
- [48] K. Y. Bliokh, F. J. Rodríguez-Fortuño, F. Nori, and A. V. Zayats, “Spin-orbit interactions of light,” *Nature Photonics*, vol. 9, pp. 796–808, 2016.
- [49] K. Y. Bliokh, A. Y. Bekshaev, and F. Nori, “Extraordinary momentum and spin in evanescent waves,” *Nature Communications*, vol. 5, 2014.
- [50] K. Y. Bliokh, D. Smirnova, and F. Nori, “Quantum spin Hall effect of light,” *Science*, vol. 348, no. 6242, pp. 1448–1451, 2015.
- [51] J. Petersen, J. Volz, and A. Rauschenbeutel, “Chiral nanophotonic waveguide interface based on spin-orbit interaction of light,” *Science*, vol. 346, no. 6205, pp. 67–71, 2014.
- [52] B. LeFeber, N. Rotenberg, and L. Kuipers, “Nanophotonic control of circular dipole emission,” *Nature Communications*, vol. 6, 2015.
- [53] I. J. Luxmoore, N. A. Wasley, A. J. Ramsay, A. C. T. Thijssen, R. Oulton, M. Hugues, S. Kasture, V. G. Achanta, A. M. Fox, and M. S. Skolnick, “Interfacing Spins in an InGaAs Quantum Dot to a Semiconductor Waveguide Circuit Using Emitted Photons,” *Physical Review Letters*, vol. 110, jan 2013.
- [54] R. J. Coles, D. M. Price, J. E. Dixon, B. Royall, E. Clarke, P. Kok, M. S. Skolnick, A. M. Fox, and M. N. Makhonin, “Chirality of nanophotonic wave-

- guide with embedded quantum emitter for unidirectional spin transfer,” *Nature Communications*, vol. 7, 2016.
- [55] F. J. Rodríguez-Fortuño, G. Marino, P. Ginzburg, D. O’Connor, A. Martínez, G. A. Wurtz, and A. V. Zayats, “Near-Field Interference for the Unidirectional Excitation of Electromagnetic Guided Modes,” *Science*, vol. 340, no. 6130, pp. 328–330, 2013.
- [56] D. O’Connor, P. Ginzburg, F. J. Rodríguez-Fortuño, G. A. Wurtz, and A. V. Zayats, “Spin–orbit coupling in surface plasmon scattering by nanostructures,” *Nature Communications*, vol. 5, 2014.
- [57] A. Espinosa-Soria and A. Martinez, “Transverse Spin and Spin-Orbit Coupling in Silicon Waveguides,” *IEEE Photonics Technology Letters*, vol. 28, pp. 1561–1564, jul 2016.
- [58] COMSOL Multiphysics, “Detailed Explanation of the Finite Element Method (FEM).” <https://www.comsol.de/multiphysics/finite-element-method> (accessed on 2017-09-20).
- [59] S. S. Rao, *The finite element method in engineering*. Elsevier/Butterworth Heinemann, 2005.
- [60] V. Thomee, *Galerkin Finite Element Methods for Parabolic Problems*, vol. 25 of *Springer Series in Computational Mathematics*. Berlin, Heidelberg: Springer Berlin Heidelberg, 2006.
- [61] P. B. Bochev and M. D. Gunzburger, “Finite Element Methods of Least-Squares Type,” *SIAM Review*, vol. 40, pp. 789–837, jan 1998.
- [62] COMSOL Multiphysics, *Wave Optics Module User’s Guide*. 2017.
- [63] Kane Yee, “Numerical solution of initial boundary value problems involving maxwell’s equations in isotropic media,” *IEEE Transactions on Antennas and Propagation*, vol. 14, pp. 302–307, may 1966.

- 
- [64] Lumerical Solutions Inc., “FDE | Lumerical Knowledge Base.” [https://kb.lumerical.com/en/solvers\\_finite\\_difference\\_eigenmode.html](https://kb.lumerical.com/en/solvers_finite_difference_eigenmode.html) (accessed on 2017-09-20).
- [65] Z. Zhu and T. Brown, “Full-vectorial finite-difference analysis of microstructured optical fibers,” *Optics Express*, vol. 10, pp. 1345–1347, aug 2002.
- [66] J. Schneider, “Understanding the finite-difference time-domain method,” *School of electrical engineering and computer engineering, Washington State University*, 2010.
- [67] S. Gedney, “Introduction to the finite-difference time-domain (FDTD) method for electromagnetics,” *Synthesis Lectures on Computational Electromagnetics*, 2011.
- [68] Lumerical Solutions Inc., “Mesh refinement options | Lumerical Knowledge Base.” [https://kb.lumerical.com/en/ref\\_sim\\_obj\\_mesh\\_refinement\\_options.html](https://kb.lumerical.com/en/ref_sim_obj_mesh_refinement_options.html) (accessed on 2017-09-20).
- [69] Lumerical Solutions Inc., “Overcoming the Multi-wavelength FDTD Challenge.” [https://www.lumerical.com/support/whitepaper/fdtd\\_multicoefficient\\_material\\_modeling.html](https://www.lumerical.com/support/whitepaper/fdtd_multicoefficient_material_modeling.html) (accessed on 2017-09-20).
- [70] Lumerical Solutions Inc., “Material Permittivity Models | Lumerical Knowledge Base.” [https://kb.lumerical.com/en/materials\\_permittivity\\_models.html](https://kb.lumerical.com/en/materials_permittivity_models.html) (accessed on 2017-09-20).
- [71] Lumerical Solutions Inc., “Using Mode Expansion Monitors | Lumerical Knowledge Base.” [https://kb.lumerical.com/en/ref\\_sim\\_obj\\_using\\_mode\\_expansion\\_monitors.html](https://kb.lumerical.com/en/ref_sim_obj_using_mode_expansion_monitors.html) (accessed on 2017-20-09).

# Appendix A

## Lumerical MODE Analysis Code

The code in Appendix A is used after running an eigenmode analysis in Lumerical MODE to visualize mode field profiles and the ratios between individual field components, plot the corresponding spin maps and calculate the spin dot product sum, related to the coupling efficiency.

### A.1 Waveguide

```
1 # E fields
2 Emode = getresult("FDE::data::mode1","E");
3 E2 = Emode.E2;
4 E2 = pinch(E2);
5 Ex = Emode.Ex;
6 Ex = pinch(Ex);
7 Ey = Emode.Ey;
8 Ey = pinch(Ey);
9 Ez = Emode.Ez;
10 Ez = pinch(Ez);
11 yz=size(E2);
12
13 y=1:1:yz(1);
14 z=1:1:yz(2);
15
```

```
16 #visualization
17 image(y,z,E2);
18 image(y,z,imag(Ex));
19 image(y,z,real(Ey));
20 image(y,z,real(Ez));
21 image(y,z,abs(Ex));
22 image(y,z,abs(Ey));
23 image(y,z,abs(Ez));
24
25 #component ratios
26 ratio1 = imag(Ex)/real(Ey);
27 ratio2 = real(Ez)/imag(Ex);
28 ratio3 = imag(Ex)/real(Ez);
29 ratio4 = real(Ey)/imag(Ex);
30
31 image(y,z,ratio1);
32 image(y,z,ratio2);
33 image(y,z,ratio3);
34 image(y,z,ratio4);
35
36 # convert index to point location
37 y_ind = 92;#65;#80;
38 z_ind = 160;#100;#119;
39
40 y_width = waveguide_width + 2*side_oxide_thickness + wavelength;
41 y_offset = nw_y_pos + nw_y_offset - y_width/2;
42 z_width = waveguide_height + top_oxide_thickness + wavelength;
43 z_offset = oxide_height + 0.5*waveguide_height - z_width/2;
44 ?y_loc = (y_width)*y_ind/yz(1)+y_offset;
45 ?z_loc = (z_width)*z_ind/yz(2)+z_offset;
46
47 y_offset = 0;
48 dy = getnamed("mesh_waveguide", "dy");
49 y_ind_center = round((yz(1)/2));
50 ?y_loc = ((y_ind_center-y_ind)*dy) + y_offset;
51
```

```

52 # reverse: get index from coordinate
53 y_loc_in = 140*1e-9;
54 z_loc_in = 1.07*1e-6;
55
56 ?y_ind_out = (y_loc_in-y_offset)*yz(1)/y_width;
57 ?z_ind_out = (z_loc_in-z_offset)*yz(2)/z_width;
58
59 z_ind_center = round((yz(2)/2));
60 z_offset2 = oxide_height + 0.5*waveguide_height;
61 dz = getnamed("mesh_waveguide", "dz");
62 ?z_ind_out = ((z_loc_in-z_offset2)/dz+z_ind_center);

```

**Listing A.1:** Field components of individual WG modes and their ratios

## A.2 Nanowire

```

1 # E fields
2 m1 = 1; # mode number 1
3 m2 = 2; # mode number 2
4 phase_shift = pi/2;
5 ratio = 1;
6 amp1 = 2/(1+ratio);
7 amp2 = amp1*ratio;
8
9 Emode1 = getresult("FDE::data::mode"+num2str(m1),"E");
10 Emode2 = getresult("FDE::data::mode"+num2str(m2),"E");
11
12 # construct the modes
13 E2_1 = amp1*amp1*Emode1.E2;
14 E2_1 = pinch(E2_1);
15 Ex_1 = amp1*Emode1.Ex;
16 Ex_1 = pinch(Ex_1);
17 Ey_1 = amp1*Emode1.Ey;
18 Ey_1 = pinch(Ey_1);
19 Ez_1 = amp1*Emode1.Ez;

```

```
20 Ez_1 = pinch(Ez_1);
21
22 E2_2 = amp2*amp2*Emode2.E2;
23 E2_2 = pinch(E2_2);
24 Ex_2 = amp2*Emode2.Ex;
25 Ex_2 = pinch(Ex_2);
26 Ey_2 = amp2*Emode2.Ey;
27 Ey_2 = pinch(Ey_2);
28 Ez_2 = amp2*Emode2.Ez;
29 Ez_2 = pinch(Ez_2);
30
31 # sum both modes with a pi/2 phase shift
32 E2 = E2_1+E2_2;
33 Ex = Ex_1+Ex_2*exp(1i*phase_shift);
34 Ey = Ey_1+Ey_2*exp(1i*phase_shift);
35 Ez = Ez_1+Ez_2*exp(1i*phase_shift);
36
37 xy=size(E2);
38
39 x=1:1:xy(1);
40 y=1:1:xy(2);
41
42 image(x,y,abs(Ez));
43 image(x,y,abs(Ex));
44 image(x,y,abs(Ey));
45
46 # field ratios
47 ratio1 = imag(Ez)/real(Ex);
48 ratio2 = real(Ey)/imag(Ez);
49 ratio3 = imag(Ez)/real(Ey);
50 ratio4 = real(Ex)/imag(Ez);
51 ratio5 = real(Ex)/real(Ey);
52 ratio6 = abs(Ex)/abs(Ey);
53
54 image(x,y,ratio1);
55 image(x,y,ratio2);
```

```

56 image(x,y, ratio3);
57 image(x,y, ratio4);
58 image(x,y, ratio5);
59 image(x,y, ratio6);

```

**Listing A.2:** Field components of individual NW modes and their ratios

## A.3 Spin Dot Product

```

1 # E fields
2 Emode = getresult("FDE::data::model", "E");
3 E2 = Emode.E2;
4 E2 = pinch(E2);
5 Ex = Emode.Ex;
6 Ex = pinch(Ex);
7 Ey = Emode.Ey;
8 Ey = pinch(Ey);
9 Ez = Emode.Ez;
10 Ez = pinch(Ez);
11 yz=size(E2);
12
13 y=1:1:yz(1);
14 z=1:1:yz(2);
15
16 # ratio between modes to determine the appropriate z coordinate
17 ratio1 = imag(Ex)/real(Ey);
18 image(y,z, ratio1);
19
20 # reverse: get index from coordinate
21 z_width = waveguide_height + top_oxide_thickness + wavelength;
22 z_offset = oxide_height + 0.5*waveguide_height - z_width/2;
23 z_loc_in = 1.07*1e-6;
24 ?z_ind_out = (z_loc_in - z_offset)*yz(2)/z_width;
25
26 z_ind_nw = 93; # determine manually from plots (E)

```

```

27 ratio1_line_nw = matrix(yz(1),1);
28 ratio11_line_nw = matrix(yz(1),1);
29
30 Ex_line_nw = matrix(yz(1),1);
31 Ey_line_nw = matrix(yz(1),1);
32 Ez_line_nw = matrix(yz(1),1);
33 plotxy(y, ratio1_line_nw);
34 plotxy(y, ratio11_line_nw);
35 plotxy(y, Ex_line_nw);
36 plotxy(y, Ey_line_nw);
37 plotxy(y, Ez_line_nw);
38
39 x = 1;
40 # spin density plots and angles
41 sEz = -1i/(2*2*pi*(c/wavelength))*((conj(Ex)*Ey-Ex*conj(Ey)));
42 image(y,z,sEz);
43
44 sEx = -1i/(2*2*pi*(c/wavelength))*((conj(Ey)*Ez-Ey*conj(Ez)));
45 image(y,z,sEx);
46
47 sEy = -1i/(2*2*pi*(c/wavelength))*((conj(Ex)*Ez-Ex*conj(Ez)));
48 image(y,z,sEy);
49
50 angl_wg = atan(sEz/(sqrt(sEx^2+sEy^2)));
51 image(y,z,angl_wg*180/pi);
52
53 angl_wg_fi = acos(sEx/sEy);
54 image(y,z,angl_wg_fi*180/pi);
55
56 a = atan(sEx/sEy)*180/pi;
57 b = atan(sqrt(sEx^2+sEy^2)/sEz)*180/pi;
58 image(y,z,a);
59 image(y,z,b);
60
61 #line plot
62 z_ind_wg = 97; #97; #93; # determine manually from plots (E)

```

```

63 sEx_line_wg = matrix(yz(1),1);
64 sEy_line_wg = matrix(yz(1),1);
65 sEz_line_wg = matrix(yz(1),1);
66
67 for (i=1:yz(1)){
68 sEx_line_wg(i) = sEx(i,z_ind_wg);
69 sEy_line_wg(i) = sEy(i,z_ind_wg);
70 sEz_line_wg(i) = sEz(i,z_ind_wg);
71 }
72 plotxy(y,sEx_line_wg);
73 plotxy(y,sEy_line_wg);
74 plotxy(y,sEz_line_wg);
75 #EXPORT
76 x = 1;
77 spin_wg = matrix(3,1);
78 spin_wg = [sEx, sEy, sEz];
79 spin_wg_line = matrix(3,1);
80 spin_wg_line = [sEx_line_wg, sEy_line_wg, sEz_line_wg];
81 sEx_wg = sEx;
82 sEy_wg = sEy;
83 sEz_wg = sEz;
84 x_wg = x;
85 y_wg = y;
86 z_wg = z;
87 yz_wg = yz;
88 savedata("spin_wg.ldf",yz_wg,spin_wg,spin_wg_line,sEx_wg,sEy_wg,
           sEz_wg,sEx_line_wg,sEy_line_wg,sEz_line_wg,x_wg,y_wg,z_wg);

```

Listing A.3: WG spin maps and export.

```

1 # E fields
2 m1 = 1; # mode number 1
3 m2 = 2; # mode number 2
4 phase_shift = pi/2;
5 ratio = 1.4;
6 ?amp1 = 2/(1+ratio);
7 ?amp2 = amp1*ratio;

```

```

8
9 Emode1 = getresult("FDE::data::mode"+num2str(m1),"E");
10 Emode2 = getresult("FDE::data::mode"+num2str(m2),"E");
11 #Emode = Emode1+Emode2*exp(1i*phase_shift);
12
13 E2_1 = amp1*amp1*Emode1.E2;
14 E2_1 = pinch(E2_1);
15 Ex_1 = amp1*Emode1.Ex;
16 Ex_1 = pinch(Ex_1);
17 Ey_1 = amp1*Emode1.Ey;
18 Ey_1 = pinch(Ey_1);
19 Ez_1 = amp1*Emode1.Ez;
20 Ez_1 = pinch(Ez_1);
21
22 E2_2 = amp2*amp2*Emode2.E2;
23 E2_2 = pinch(E2_2);
24 Ex_2 = amp2*Emode2.Ex;
25 Ex_2 = pinch(Ex_2);
26 Ey_2 = amp2*Emode2.Ey;
27 Ey_2 = pinch(Ey_2);
28 Ez_2 = amp2*Emode2.Ez;
29 Ez_2 = pinch(Ez_2);
30
31 E2 = E2_1+E2_2;
32 Ex = Ex_1+Ex_2*exp(1i*phase_shift);
33 Ey = Ey_1+Ey_2*exp(1i*phase_shift);
34 Ez = Ez_1+Ez_2*exp(1i*phase_shift);
35
36 xy=size(E2);
37 x=1:1:xy(1);
38 y=1:1:xy(2);
39 z = 1;
40
41 # spin components
42 sEz = -1i/(2*2*pi*(c/wavelength))*((conj(Ex)*Ey-Ex*conj(Ey)));
43 image(x,y,(sEz));

```

```

44 sEx = -1i/(2*2*pi*(c/wavelength))*((conj(Ey)*Ez-Ey*conj(Ez)));
45 image(x,y,(sEx));
46 sEy = -1i/(2*2*pi*(c/wavelength))*((conj(Ex)*Ez-Ex*conj(Ez)));
47 image(x,y,(sEy));
48 # calculate theta
49 angl_nw = atan(sEz/(sqrt(sEx^2+sEy^2)));
50 image(x,y,90+(angl_nw*180/pi));
51
52 # OVERLAP CALCULATIONS
53 # NW
54 ?x_span_nw = getnamed("mesh_nanowire","x span");
55 ?dx_nw = getnamed("mesh_nanowire","dx");
56 ?num_x_nw = floor(x_span_nw/dx_nw);
57 if((-1)^num_x_nw===-1){
58 num_x_nw=num_x_nw-1;
59 }
60 ?num_x_FDE = getnamed("FDE","actual mesh cells x");
61 ?center_x_FDE = round(num_x_FDE/2); # automatically -> can be wrong
62 center_x_FDE = 90; # manually
63 ?x_min_nw = center_x_FDE-floor(num_x_nw/2);
64 ?x_max_nw = center_x_FDE+floor(num_x_nw/2);
65
66 ?y_span_nw = getnamed("mesh_nanowire","y span");
67 ?dy_nw = getnamed("mesh_nanowire","dy");
68 ?num_y_nw = floor(y_span_nw/dy_nw);
69 if((-1)^num_y_nw===-1){
70 num_y_nw=num_y_nw-1;
71 }
72 ?num_y_FDE = getnamed("FDE","actual mesh cells y");
73 ?center_y_FDE = round(num_y_FDE/2); # automatically -> can be wrong
74 center_y_FDE = 90; # manually
75 ?y_min_nw = center_y_FDE-round(num_y_nw/2);
76 ?y_max_nw = center_y_FDE+round(num_y_nw/2);
77
78 subEx = sEx(x_min_nw:x_max_nw,y_min_nw:y_max_nw);
79 subEy = sEy(x_min_nw:x_max_nw,y_min_nw:y_max_nw);

```

```
80 subEz = sEz(x_min_nw:x_max_nw,y_min_nw:y_max_nw);
81
82 y_ind_nw = 90;
83 sx_line_nw = matrix(xy(1),1);
84 sy_line_nw = matrix(xy(1),1);
85 sz_line_nw = matrix(xy(1),1);
86 for(i=1:xy(1)){
87     sx_line_nw(i) = sEx(i,y_ind_nw);
88     sy_line_nw(i) = sEy(i,y_ind_nw);
89     sz_line_nw(i) = sEz(i,y_ind_nw);
90 }
91 plotxy(x,sz_line_nw);
92
93 # LOAD DATA from WG
94 loaddata("spin_wg");
95 plotxy(y_wg,sEz_line_wg);
96 x_wg = 1000;
97 sx_wg = matrix(x_wg,yz_wg(1));
98 sy_wg = matrix(x_wg,yz_wg(1));
99 sz_wg = matrix(x_wg,yz_wg(1));
100 for(i=1:x_wg){
101     for(j=1:yz_wg(1)){
102         sx_wg(i,j)=(sEx_line_wg(j));
103         sy_wg(i,j)=(sEy_line_wg(j));
104         sz_wg(i,j)=(sEz_line_wg(j));
105     }
106 }
107 image(1:x_wg,1:yz_wg(1),sx_wg);
108 image(1:x_wg,1:yz_wg(1),sy_wg);
109 image(1:x_wg,1:yz_wg(1),sz_wg);
110
111 # CALCULATIONS 2D
112 nw_offset = 0*1e-9;
113 nw_offset_list = (-200:5:200)*1e-9;
114 dot_pr = matrix(length(nw_offset_list),1);
115 dot_pr_right = matrix(length(nw_offset_list),1);
```

```
116 dot_pr_left = matrix(length(nw_offset_list),1);
117
118 for(o=1:length(nw_offset_list)){
119   nw_offset = nw_offset_list(o);
120
121   nw_offset_ind = round(nw_offset/dy_nw);
122   wg_center = round(yz_wg(1)/2);
123   x_start_index = round(x_wg/2)-(num_x_nw/2);
124   x_end_index = x_start_index + num_x_nw;
125   y_start_index = wg_center-nw_offset_ind-round(num_y_nw/2);
126   y_end_index = y_start_index+num_y_nw;
127
128   vect_nw_plot_x = matrix(x_end_index-x_start_index+1,y_end_index-
      y_start_index+1);
129   vect_nw_plot_y = matrix(x_end_index-x_start_index+1,y_end_index-
      y_start_index+1);
130   vect_nw_plot_z = matrix(x_end_index-x_start_index+1,y_end_index-
      y_start_index+1);
131
132   vect_wg_plot_x = matrix(x_end_index-x_start_index+1,y_end_index-
      y_start_index+1);
133   vect_wg_plot_y = matrix(x_end_index-x_start_index+1,y_end_index-
      y_start_index+1);
134   vect_wg_plot_z = matrix(x_end_index-x_start_index+1,y_end_index-
      y_start_index+1);
135
136   vect_dot_prod = matrix(x_end_index-x_start_index+1,y_end_index-
      y_start_index+1);
137
138   vect_nw = matrix(3,1);
139   vect_wg = matrix(3,1);
140   dot_pr(o) = 0;
141   dot_pr_right(o) = 0;
142   dot_pr_left(o) = 0;
143
144   for(i=x_start_index:x_end_index){
```

```

145 for(j=y_start_index:y_end_index){
146 vect_nw = [sEx(i-x_start_index+x_min_nw, j-y_start_index+y_min_nw),
            sEy(i-x_start_index+x_min_nw, j-y_start_index+y_min_nw),sEz(i-
            x_start_index+x_min_nw, j-y_start_index+y_min_nw)];
147 vect_nw_plot_x(i-x_start_index+1,j-y_start_index+1)=vect_nw(1);
148 vect_nw_plot_y(i-x_start_index+1,j-y_start_index+1)=vect_nw(2);
149 vect_nw_plot_z(i-x_start_index+1,j-y_start_index+1)=vect_nw(3);
150
151 vect_wg = [sx_wg(i,j), sy_wg(i,j), sz_wg(i,j)];
152 vect_wg_plot_x(i-x_start_index+1,j-y_start_index+1)=vect_wg(1);
153 vect_wg_plot_y(i-x_start_index+1,j-y_start_index+1)=vect_wg(2);
154 vect_wg_plot_z(i-x_start_index+1,j-y_start_index+1)=vect_wg(3);
155
156 dot_pr_temp = dot(vect_nw, vect_wg);
157 vect_wg_plot_z(i-x_start_index+1,j-y_start_index+1)=dot_pr_temp;
158 dot_pr(o) = dot_pr(o) + dot_pr_temp;
159 if(dot_pr_temp>0){
160 dot_pr_right(o)=dot_pr_right(o)+dot_pr_temp;
161 }
162 else{
163 dot_pr_left(o)=dot_pr_left(o)+dot_pr_temp;
164 }
165 }
166 }
167 }
168 # PLOTS
169 plotxy(1:length(nw_offset_list),dot_pr);
170 plotxy(1:length(nw_offset_list),dot_pr_left);
171 plotxy(1:length(nw_offset_list),dot_pr_right);
172 plotxy(1:length(nw_offset_list),abs(dot_pr_right/dot_pr_left));

```

**Listing A.4:** NW spin maps, import of WG spin maps and calculation of spin dot product sum.

# Appendix B

## Lumerical FDTD Postprocessing Code

The code below is used in the postprocessing stage - after running FDTD Simulations of the NW on WG structure, the reflectivity, coupling ratio and coupling efficiency are extracted from the monitors and exported to a .txt file.

```
1 k = 0; # counter for number of files
2 files = splitstring(dir, endl); # directory contents
3 for(i=1:length(files)) { # loop over all files
4   if (findstring(files{i}, "fsp") != -1) { # look for 'fsp' files
5     if (fileexists(files{i})) { # check if the file exists
6       filename = files{i}; # output file name
7       load(files{i}); # load file
8
9     filename = filebasename(currentfilename);
10    source_mode_list = [1, 3, 4, 6, 7, 9]; # HE11a, TE01, HE21a, TM01,
        EH11a, HE31a
11    source_mode_list2 = [2, 3, 5, 6, 8, 10]; # HE11b, TE01, HE21b, TM01,
        EH11b, HE31b
12
13    select("nw_ME_monitor");
14    updatemodes(1:30);
15    unselectall;
```

```

16
17 mnum = 1; #HE11(a+b)
18 mode_num = source_mode_list(mnum);
19 mode_num2 = source_mode_list2(mnum);
20 wavelength = getnamed("source", "wavelength_start");
21 ?n_eff_data = getresult("nw_ME_monitor", "neff");
22 ?n_eff = real(n_eff_data.neff(mode_num));
23 ?k_eff = imag(n_eff_data.neff(mode_num));
24 ?alpha = 4*pi*k_eff/wavelength;
25 ?n_eff2 = real(n_eff_data.neff(mode_num2));
26 ?k_eff2 = imag(n_eff_data.neff(mode_num2));
27 ?alpha2 = 4*pi*k_eff/wavelength;
28
29 # monitor data
30 monitor_num = 1;
31 monitor_data = getresult("nw_ME_monitor", "expansion for nw_monitor_"
    +num2str(monitor_num));
32 ?monitor_num; # just for display
33 ?Tforward = monitor_data.T_forward(mode_num);
34 ?Tforward2 = monitor_data.T_forward(mode_num2);
35
36 Tmeas = monitor_data.T_total(mode_num);
37 # monitor at the start
38 monitor_data_start = getresult("nw_ME_monitor", "expansion for
    nw_monitor_start_1");
39 ?Tbackward_start = monitor_data_start.T_backward(mode_num);
40 ?Tbackward_start2 = monitor_data_start.T_backward(mode_num2);
41 ?z_pos_start = getresult("nw_monitor_start_1", "z");
42 format short;
43 ?z_pos = getresult("nw_monitor_"+num2str(floor(monitor_num)), "z");
44 z_pos_source = getresult("source", "z");
45 format long;
46 ?reflected = Tforward*exp(alpha*z_pos);
47 ?reflected2 = Tforward2*exp(alpha2*z_pos);
48 ?incident = abs(Tbackward_start)*exp(-alpha*z_pos_start);
49 ?reflectivity = reflected + reflected2; #reflected/incident;

```

```
50
51 select("wg_ME_monitor");
52   updatemodes(1:30);
53   unselectall;
54
55 transmission_right = getresult("wg_ME_monitor","expansion for
    wg_monitor_right_2");
56 transmission_left = getresult("wg_ME_monitor","expansion for
    wg_monitor_left_2");
57
58 # determine guided modes
59 mode_data = getresult("wg_ME_monitor","neff");
60 cutoff = 0;
61 for(j=1:30){
62   mode_data_neff = mode_data.neff;
63   if(real(mode_data_neff(j))>1){
64     cutoff = cutoff+1;
65   }
66 }
67 # transmissions
68 Trans_right = 0;
69 Trans_left = 0;
70 for(i=1:cutoff) {
71   Tr_temp = transmission_right.T_forward(i);
72   Tl_temp = -transmission_left.T_backward(i);
73
74   Trans_right = Trans_right + Tr_temp;
75   Trans_left = Trans_left + Tl_temp;
76 }
77 Tr1 = transmission_right.T_forward(1);
78 Tr2 = transmission_right.T_forward(2);
79 Tr3 = transmission_right.T_forward(3);
80 Tl1 = -transmission_left.T_backward(1);
81 Tl2 = -transmission_left.T_backward(2);
82 Tl3 = -transmission_left.T_backward(3);
83
```

```

84 # saving to text
85 results_tempstr = filename + "_RESULTS.txt";
86
87 str_header = "Ttot:          Tfwd(1):          Tfwd(2):          Tfwd(1)+Tfwd
(2)";
88 write(results_tempstr , str_header);
89 str_data = num2str(Tmeas) + "          " + num2str(reflected) + "
" + num2str(reflected2) + "          " + num2str(reflectivity);
90 write(results_tempstr , str_data);
91
92 str_header = "Right:          Ttot:          Tfwd(1):          Tfwd(2):
Tfwd(3):";
93 write(results_tempstr , str_header);
94 str_data = "          " + num2str(Trans_right) + "          "
+ num2str(Tr1) + "          " + num2str(Tr2) + "          " + num2str
(Tr3);
95 write(results_tempstr , str_data);
96
97 str_header = "Left:          Ttot:          Tfwd(1):          Tfwd(2):
Tfwd(3):";
98 write(results_tempstr , str_header);
99 str_data = "          " + num2str(Trans_left) + "          " +
num2str(Tl1) + "          " + num2str(Tl2) + "          " + num2str(
Tl3);
100 write(results_tempstr , str_data);
101
102 str_header = "Right/Left:          Ttot:          Tfwd(1):
Tfwd(2):          Tfwd(3):";
103 write(results_tempstr , str_header);
104 str_data = "          " + num2str(Trans_right/Trans_left) +
"          " + num2str(Tr1/Tl1) + "          " + num2str(Tr2/Tl2) + "
" + num2str(Tr3/Tl3);
105 write(results_tempstr , str_data);
106
107 str_header = "Left/Right:          Ttot:          Tfwd(1):
Tfwd(2):          Tfwd(3):";

```

```
108 write(results_tempstr , str_header);
109 str_data = " " + num2str(Trans_left/Trans_right) +
            " " + num2str(Tl1/Tr1) + " " + num2str(Tl2/Tr2) + " "
            " + num2str(Tl3/Tr3);
110 write(results_tempstr , str_data);
111 }
112 }
113 }
```

**Listing B.1:** Evaluation of FDTD results and export to a .txt file.